

# Study of the electron density in the high latitude ionosphere with incoherent scatter radars and Swarm satellites

A Thesis Submitted to the College of  
Graduate and Postdoctoral Studies in  
Partial Fulfillment of the Requirements  
for the Degree of Master of Science in the  
Department of Physics and Engineering Physics  
University of Saskatchewan  
Saskatoon

By  
Hayden Fast

# Permission to use

In presenting this thesis in partial fulfillment of the requirements for a Postgraduate degree from the University of Saskatchewan, I agree that the Libraries of this University may make it freely available for inspection. I further agree that permission for copying of this thesis in any manner, in whole or in part, for scholarly purposes may be granted by the professor or professors who supervised my thesis work or, in their absence, by the Head of the Department or the Dean of the College in which my thesis work was done. It is understood that any copying or publication or use of this thesis or parts thereof for financial gain shall not be allowed without my written permission. It is also understood that due recognition shall be given to me and to the University of Saskatchewan in any scholarly use which may be made of any material in my thesis.

Requests for permission to copy or to make other uses of materials in this thesis in whole or part should be addressed to:

Head of the Department of Physics and Engineering Physics

116 Science Place

University of Saskatchewan

Saskatoon, Saskatchewan S7N 5E2 Canada

OR

Dean

College of Graduate and Postdoctoral Studies

University of Saskatchewan

116 Thorvaldson Building, 110 Science Place

Saskatoon, Saskatchewan S7N 5C9 Canada

# Abstract

Despite century-long efforts in assessing the electron density distribution in the Earth's ionosphere and significant progress in identification of its major features, there are still many uncertainties with respect to the solar cycle's seasonal and diurnal trends at various latitudes. Knowledge of these variations is needed for robust forecasting of the state of the ionosphere for the operation of practical radio systems, for example communication via high frequency radio waves.

This thesis utilizes data from the incoherent scatter radar (ISR) at Poker Flat (Alaska, USA) to assess the diurnal and seasonal variations of three parameters of the ionospheric F2 region, the peak density, the height of the peak, and the thickness of the layer. These parameters are assessed for relatively high solar activity in 2014, and relatively low solar activity in 2016. Daytime electron densities were found to be largest during winter and spring and nighttime electron densities were found to be smallest in winter. Electron densities during the higher solar activity year were found to be greater than those during the lower solar activity year by a factor of 2-5, depending on the time of day, as expected. Details of the diurnal variations in electron density for various seasons are further discussed.

ISR electron density data are also used for the validation of electron density measurements from Langmuir probes onboard the Swarm satellites in the topside ionosphere (~500 km). This work is an expansion of previous studies that use a different mode of ISR operation and a different approach to both ISR and Swarm satellite data handling. In addition to observations over Poker Flat (geographic latitude of ~60° N), observations over Resolute Bay, Canada at extreme high latitudes of ~80° are also considered. It is shown that, overall, the ratio of Swarm electron density measurements to those measured by ISRs is ~0.5-0.6 and that smaller ratios are observed at larger electron densities, usually during the daytime. At low electron densities less than  $3 \cdot 10^{10} \text{ m}^{-3}$ , the ratios are typically greater than 1, indicating an overestimation effect. The overestimation effect is stronger at night and at higher altitude. It is also more evident during lower solar activity when the electron density in the topside ionosphere is smaller. The conclusions on the electron density underestimation and overestimation by the Swarm Langmuir probes are overall consistent with previous reports, but this thesis confirms that these effects also occur at high latitudes.

# Acknowledgments

I would like to thank my supervisor, Dr. Alexander Koustov, for his guidance and assistance throughout this project, as well as providing me with an opportunity to complete a M.Sc. degree at the University of Saskatchewan. With his invitation, I was able to attend workshops, both virtually and in-person, which gave me an opportunity to learn about other research topics in the field and to improve my presentation skills. His help and feedback throughout the writing of this thesis was extremely helpful and this thesis would not be complete without it.

I would like to thank Bion Larson for his assistance in programming and reading the Swarm data at the beginning of this project, and for providing insight on numerous issues throughout my Master's program. I would also like to thank him for his previous work on the validation of Swarm Langmuir probe measurements which is expanded on in Chapter 4 of this thesis.

I would like to thank Dr. Koustov, the Department of Physics and Engineering Physics, the CREATE program, and the Institute of Space and Atmospheric Studies for providing funding that made this thesis possible.

Finally, I would like to thank my family and friends for their support and encouragement throughout the program.

# Contents

Contents.....	iv
List of tables .....	vii
List of figures.....	viii
Abbreviations.....	xiv
Symbols.....	xvi
Chapter 1	
Introduction .....	1
1.1 Plasma, major concepts.....	2
1.1.1 Debye length.....	2
1.1.2 Langmuir waves and plasma frequency.....	3
1.1.3 $\vec{E} \times \vec{B}$ drift of plasma .....	5
1.2 The Sun, solar wind and IMF.....	5
1.3 Solar activity cycles and their characterization.....	8
1.3.1 Sunspot number .....	8
1.3.2 F10.7-cm radio flux .....	9
1.3.3 Solar cycles .....	9
1.4 The Earth's ionosphere .....	10
1.4.1 Ionospheric layers.....	10
1.4.2 Neutral atmosphere.....	11
1.4.3 Chapman theory of ionization .....	12
1.4.4 Plasma chemistry at F region heights .....	15
1.4.5 Formation of the F2 layer.....	17
1.4.6 Topside ionosphere and protonosphere .....	18
1.5 Empirical modeling of the electron density in the ionosphere, NeQuick approach ...	18
1.6 Objectives of the thesis work .....	21
1.7 Thesis outline .....	23
Chapter 2	
Instruments .....	24
2.1 Incoherent Scatter Radars .....	24
2.1.1 Principles of ISR operation .....	25
2.1.2 Advanced Modular ISRs and the Poker Flat ISR.....	30
2.1.3 Resolute Bay ISR .....	33

2.1.4 Data Sources .....	34
2.2 Comparison of 1-min and 5-min RISR electron density data in Imaging Mode .....	34
2.3 Langmuir probe instruments in space .....	39
2.3.1 Classical Langmuir probes .....	40
2.3.2 Specific features of the Swarm LPs.....	45
2.3.3 Data source .....	48
2.4 Summary .....	49
Chapter 3	
Electron density over Poker Flat, Alaska .....	50
3.1 Variations in solar activity over the last decade .....	50
3.2 Methodology of the analysis .....	52
3.3 Overall electron density profiles versus UT time .....	53
3.4 Overall electron density profiles versus season .....	56
3.5 Diurnal variation of $N_mF2$ .....	58
3.6 Diurnal variation of $h_mF2$ .....	60
3.7 Trends in the thickness of the F2 layer inferred from NeQuick analysis .....	61
3.8 Diurnal and seasonal variations in the ionospheric topside .....	64
3.9 Discussion of the results .....	67
3.9.1 Solar cycle variation .....	67
3.9.2 Seasonal variation.....	68
3.9.3 Diurnal variation.....	69
3.9.4 Thickness of the F2 later and electron density in the ionospheric topside .....	70
3.9.5 Electron density variations in the ionospheric bottomside .....	73
3.10 Conclusions .....	73
Chapter 4	
Validation work for Swarm Langmuir probes.....	73
4.1 Introduction .....	73
4.2 Methodology of the analysis .....	75
4.2.1 Geometry and approach .....	76
4.2.2 Data coverage .....	79
4.2.3 Variability of Swarm and ISR electron densities over conjunction regions .....	81
4.3 RISR and Swarm comparison, results for the polar cap .....	83
4.3.1 Overall scatter plots .....	83
4.3.2 Diurnal differences between $N_e^{Swarm}$ and $N_e^{RISR}$ .....	84
4.4 PFISR and Swarm comparison, results for the auroral zone.....	86

4.4.1 Overall scatter plots .....	86
4.4.2 Diurnal differences between $N_e^{Swarm}$ and $N_e^{PFISR}$ .....	87
4.4.3 Examining the ratio $N_e^{Swarm}/N_e^{PFISR}$ versus absolute electron density .....	89
4.4.4 Solar cycle trend for the ratio R .....	90
4.4.5 UT/MLT variations of the ratio R .....	93
4.5 Discussion of the results .....	94
4.5.1 Swarm underestimation effect.....	94
4.5.2 Swarm overestimation effect.....	97
4.6 Conclusions .....	98
Chapter 5	
Summary of the thesis work and suggestions for future research .....	100
5.1 Summary of the thesis work.....	100
5.1.1 Seasonal and diurnal variations of the electron density over Poker Flat .....	100
5.1.2 Validation work for Swarm LP instruments .....	101
5.2 Suggestions for future research .....	103
5.2.1 Study of long-term trends in the ionosphere over Alaska .....	103
5.2.2 Further validation work for the NeQuick ionospheric model .....	104
References .....	106

# List of tables

2.1	List of RISR-C experiments considered for the comparison of 1-min and 5-min data .....	35
4.1	The median value $\mu$ and the standard deviation $\sigma$ for a histogram distribution of the ratio $R = N_e^{Swarm}/N_e^{PFISR}$ and number of points $n$ for all conjunctions between RISR-AC, PFISR-AC and PFISR-B .....	95
4.2	Coefficients of a linear fit in the form $N_e^{Swarm} = a \cdot N_e^{ISR} + b$ , total number of points, and correlation coefficient to a scatter plot of electron density measured by Swarm versus electron density measured by ISRs for all conjunctions between RISR-AC, PFISR-AC, and PFISR-B. Values of $b$ are given in units of $10^{10} \text{ m}^{-3}$ .....	96
4.3	Percentages of cases with ratio $R = N_e^{Swarm}/N_e^{PFISR}$ more than 1.3 for various time sectors .....	97

# List of figures

1.1	A sketch showing the auroral oval (Feldstein, 2016), yellow belt. Blobs of enhanced plasma, shown by black dots, are polar cap patches travelling from the dayside to the nightside with the bulk of the plasma. The plasma flow pattern at high latitudes is represented by two global-scale cells. The plot is given in magnetic local time-magnetic latitude coordinates (Kivelson and Russel, 1995). The plot was modified from that given by Larson (2021) .....	7
1.2	Daily values of (a) the sunspot number (SSN) and (b) the F10.7-cm solar radiation flux from 1965 to 2022. (c) Scatter plot of SSN versus F10.7-cm flux. The correlation coefficient between the two indices is shown in the bottom left corner. The data were taken from <a href="https://omniweb.gsfc.nasa.gov/form/dx1.html">https://omniweb.gsfc.nasa.gov/form/dx1.html</a> (last accessed 7 May 2022) .....	10
1.3	Electron density profiles in the ionosphere over Resolute Bay, Canada according to the IRI model (Bilitza, 2018). The solid traces are for day ionosphere and the dashed traces are for night ionosphere. Red and blue traces correspond to predictions for high (2013) and low (2018) solar activity, respectively .....	11
1.4	Electron density profiles according to the NeQuick ionospheric model for various values of parameters $H_0$ , $g$ and $r$ . The peak of the profiles was selected at 300 km. Blues lines in panels (d), (e) and (f) correspond to the “optimal” selection of parameters $g$ and $r$ , suggested by Themens et al. (2018). A vertical dashed line is shown in each panel intersecting where electron density is equal to 70% of the peak value, $N_mF2$ , to assess the effective thickness of each profile .....	20
2.1	(a) A sketch illustration of ISR radar configuration for measurements at high latitudes. Insert on the right shows a generic electron density profile in the ionosphere for altitudes from 100 km to 600 km. (b) A sketch of the typical spectrum of a signal received by an ISR. The dashed line represents an ion spectrum without Doppler shift .....	26
2.2	Sketch of a two-pulse sequence transmitted and received by an ISR system. Horizontally is time and vertically is the distance traveled by the transmitted and scattered signal. Image from McWilliams et al. (2003) .....	27
2.3	Simulated ISR spectra for 1, 30, and 600 independent computer runs illustrating the effect of integration time on the shape of the ion line. The solid line is the theoretical spectral line expected for the conditions of modeling. This is Figure 5 from Diaz et al. (2008) .....	29
2.4	Image of individual antenna element units (AEUs) on the face of the RISR-C radar. Image from Gillies & Varney (2016) .....	31

2.5	PFISR beam geometry in International Polar Year (IPY) mode. The left plot shows the direction of each beam with the radar located at the center of the plot. Radially is elevation angle and tangentially is the azimuth angle of each beam. The right plot shows the magnetic coordinates covered over the entire range of each beam. Image from <a href="https://isr.sri.com/madrigal">https://isr.sri.com/madrigal</a> .....	32
2.6	PFISR observations in the IPY mode from ~15 UT on 16 January, 2016 to ~19 UT on 18 January, 2016. Data shown are from one of the 4 beams in IPY. Azimuth and elevation angles for the given beam are shown at the top of the plot. On the horizontal axis is UT time in hours, and on the vertical axis is altitude in kilometers. Electron density is represented by the color bar at the bottom of the figure. Image from the SRI Madrigal Database: <a href="https://isr.sri.com/madrigal">https://isr.sri.com/madrigal</a> .....	33
2.7	Electron density ( $N_e$ ) data collected by the RISR-C radar at the height of 300 km for multiple events in March 2016 (Table 2.1) in the Imaging Mode of operation (51 beams). (a) Scatter plot of $N_e$ with 1-min resolution versus $N_e$ with 5-min resolution. Shown also is the bisector of perfect agreement, the thin black line. (b) Histogram of the relative difference, $(N_e^{5\text{min}} - N_e^{1\text{min}})/N_e^{5\text{min}}$ , expressed in percent. Shown also are the total number of points, $n$ , median of the distribution, $\mu$ , and the standard deviation for the distribution, $\sigma$ . (c) Scatter plot of the relative error in $N_e$ measurements (in percent) for the $N_e^{1\text{min}}$ data. (d) the same as (c) but for the $N_e^{5\text{min}}$ data .....	36
2.8	The same as Figure 2.7 but for the height of 450 km .....	38
2.9	Variation with height of (a) the histogram distribution median, $\mu$ , and (b) standard deviation, $\sigma$ , for the quantity $(N_e^{5\text{min}} - N_e^{1\text{min}})/N_e^{5\text{min}}$ expressed in percent .....	39
2.10	Langmuir probe current as a function of bias voltage. The ion saturation, electron retardation, and electron acceleration regions are indicated. Electron temperature can be measured at the point indicated by $T_e$ . Adapted from Schunk & Nagy (2009). The sketch is a courtesy of A.V. Koustov .....	41
2.11	A schematic illustrating ion-driven current excitation in a negatively biased Langmuir probe .....	42
2.12	A schematic illustration of the Swarm measurement technique in harmonic mode. The plot was sketched from Figure 7 of Knudsen et al. (2017) and Figure 2.6 of Quinn (2019). Courtesy of A.V. Koustov .....	47
3.1	Variations of the solar activity between 2009 and 2020 as characterized by (a) the sunspot number (SSN) and (b) the F10.7-cm radio flux. Shaded horizontal bars mark periods selected for the ionospheric electron density analysis in this chapter. The SSN data were downloaded from <a href="https://www.sidc.be/silso/newdataset">https://www.sidc.be/silso/newdataset</a> (Royal Observatory of Belgium, Brussels, 13 April 2023) while the F10.7-cm flux data were downloaded from <a href="https://omniweb.gsfc.nasa.gov/form/dx1.html">https://omniweb.gsfc.nasa.gov/form/dx1.html</a> .....	51
3.2	Number of Poker Flat ISR radar measurements on the UT-month plane for observations in 2014 and 2016 .....	53

3.3	Electron density $N_e$ at various heights versus UT for four seasons. Panels (a-d) and (e-h) are for observations in 2014 and 2016, respectively. The values are given in units of $10^{10} \text{ m}^{-3}$ . All data obtained by the Poker Flat ISR in the International Polar Year mode were considered .....	54
3.4	Line plots of the electron density $N_e$ at the heights of 150 (panel a and b), 300 km (panels c and d), and 450 km (panel e and f) versus UT for 2014 (solid lines) and 2016 (dashed lines) as measured by the PFISR radar. The dots are hourly medians. Vertical bars are median values $\pm$ one standard deviation for each bin of UT hour. ....	55
3.5	Electron density at various heights versus month in four time sectors. Panels (a-d) and (e-f) are for observations in 2014 and 2016, respectively. The values are given in units of $10^{10} \text{ m}^{-3}$ . All data obtained by the Poker Flat ISR in the International Polar Year mode were considered .....	56
3.6	Line plots of the electron density $N_e$ at the heights of 150 km (panels a and b), 300 km (panels c and d), and 450 km (panels (e and f) versus month for 2014 (solid lines) and 2016 (dashed lines) as measured by the PFISR radar. The dots are monthly medians. Vertical bars are median values $\pm$ one standard deviation for each month. ....	57
3.7	Electron density at the maximum of F2 layer ( $N_mF2$ ) versus UT for various months for (a) 2014 and (b) 2016. All data obtained by the Poker Flat ISR in the International Polar Year mode were considered. The values are given in units of $10^{10} \text{ m}^{-3}$ .....	58
3.8	Line plots of the (panels a and b) peak electron density $N_mF2$ and (panels c and d) peak height versus month for 2014 (solid lines) and 2016 (dashed lines) as measured by the PFISR radar. The dots are monthly medians.....	59
3.9	Height of the peak electron density of F2 layer ( $h_mF2$ ) versus UT for various months of (a) 2014 and (b) 2016. All data obtained by the Poker Flat ISR in the International Polar Year mode of observations were considered .....	60
3.10	Histogram distributions of the parameter $H_0$ in four separate time sectors. All data obtained by the Poker Flat ISR in the International Polar Year mode of observations were considered. Each panel shows the total number of points $n$ , median $\mu$ , and standard deviation $\sigma$ , of the distribution .....	62
3.11	Scatter plots of the parameter $H_0$ (open blue circles) versus time of the year (month) for four separate time sectors of measurements in 2014. Solid blue lines represent monthly median values in 2014. Solid red lines are monthly medians for measurements in 2016 .....	63
3.12	Contour plots for the parameter $H_0$ occurrence versus UT time for four seasons in 2014 (left four panels) and 2016 (right four panels) .....	64

3.13	Diurnal variation of the electron density as measured by the Poker Flat ISR system near Fairbanks, Alaska on 21 March, 2007. ISR-derived $h_mF2$ is shown by the pink line and ISR-derived $N_mF2$ is shown by the black line. From Whittier (2014) .....	68
3.14	Line plot of the hourly medians of the electron density at a height of 450 km versus UT time as measured by the PFISR radar in (a) summer (red line) and (b) winter (blue line) for 2016. Grey dots are the electron density $N_e$ values inferred from the NeQuick model for each individual $N_e$ profile. Solid green dots connected by the green line are the hourly medians of the $N_e$ values inferred from NeQuick .....	71
4.1	A map illustrating typical measurement coverage by RISR-C (Resolute Bay) and PFISR (Poker Flat), and the footprints of the Swarm satellites passing the area of ISR measurements in two different events. For the ISRs, an altitude of $\sim 450$ km was considered. Crosses indicate those locations for which a median electron density was computed and compared to Swarm data. Darker shaded segments around Resolute Bay and Poker Flat outline the areas over which the median Swarm data was computed along a trajectory. Shown by solid dots are Swarm C footprints for 27 July 2016 ( $\sim 16:35$ UT, blue) and Swarm A footprints for 21 February 2015 ( $\sim 07:23$ UT, pink). Arrows indicate directions of satellite travel .....	76
4.2	Details on methodology of ISR-Swarm comparison for the Poker Flat (PFISR) radar. (a) Footprints of the Swarm A and Swarm C satellites passing the area of PFISR observations on 26 May 2014 at $\sim 01:58$ UT moving equatorward (arrow). The observed electron density is represented by the color according to the bar at the bottom of the panel. For PFISR, an altitude of 450 km was considered. Colored segments reflect the median electron density according to the color bar at the bottom. (b) Electron density profile according to PFISR measurements. Colored diamonds indicate measurements for the conjunction. (c) Line plot of the electron density measured by the instruments and median values passed to the data base .....	77
4.3	Number of joint ISR-Swarm measurements on the UT-month plane for observations over Poker Flat, left panels, and Resolute Bay (RISR-C radar), right panels. For the Poker Flat data, each UT-month cell is divided into two halves with the left half for each month corresponding to the radar-Swarm AC conjunctions while the right half of each month corresponding to the radar-Swarm B conjunctions .....	79
4.4	Histogram distributions for the occurrence of the electron density measured by the incoherent scatter radars PFISR and RISR-C for all conjunctions with Swarm satellites in 2014 to 2020. Blue columns are for the PFISR-Swarm AC conjunctions, red columns are for the RISR-C-Swarm AC conjunctions and black columns are for the PFISR-Swarm B conjunctions. The ISR electron density is plotted in units of $10^{10} \text{ m}^{-3}$ . Total number of points $n$ , median value $\mu$ (in units of $10^{10} \text{ m}^{-3}$ ) and standard deviation $\sigma$ (in units of $10^{10} \text{ m}^{-3}$ ) for each distribution are given in the upper right corner by numbers colored respectively .....	80

4.5	Standard deviations of electron density for Swarm measurements versus standard deviation of electron density for PFISR measurements over respective areas of conjunctions for the PFISR-AC comparison. (b) The same as (a) but for PFISR-B comparison. (c) Standard deviations of electron density for PFISR measurements versus the absolute value of the electron density measured by PFISR. The triangles are the medians of standard deviations in $N_e^{PFISR}$ bins of $2 \cdot 10^{10} \text{ m}^{-3}$ (d) The same as (c) but for standard deviations of Swarm AC measurements .....	82
4.6	Scatter plot of the electron density measured by the Swarm A and Swarm C satellites $N_e^{Swarm}$ versus electron density measured by the Resolute Bay incoherent scatter radar RISR-C $N_e^{RISR}$ . Darker circles reflect measurements where $N_e^{Swarm}/N_e^{RISR} > 1$ . Red solid dots are medians of $N_e^{Swarm}$ in bins of $N_e^{RISR}$ (size of each bin is $2 \cdot 10^{10} \text{ m}^{-3}$ ). Vertical red bars are the binned values of $N_e^{Swarm} \pm$ one standard deviation of $N_e^{Swarm}$ . The green line is a linear fit line assuming that the RISR-C measurements are precise. The Dashed line is a linear fit line according to the data presented by Larson et al. (2021) .....	84
4.7	Scatter plots of electron density measured onboard the Swarm A and Swarm C satellites versus electron density measured by the RISR-C incoherent scatter radar. The format of the plots is the same as in Figure 4.6. Panels (a) through (d) are for the dawn, day, dusk, and night sectors. Definitions of the time sectors are given in the text .....	84
4.8	Scatter plots of the electron density measured onboard the Swarm satellites versus electron density measured by the PFISR incoherent scatter radar. The format of the plots is the same as in Figure 4.6. Panels (a) and (b) are for the PFISR-AC and PFISR-B conjunctions, respectively .....	87
4.9	Scatter plots of electron density measured onboard the Swarm AC satellites versus electron density measured by the PFISR incoherent scatter radar. The format of the plots is the same as for Figure 4.6. Panels (a) through (d) are for the dawn, day, dusk, and night sectors, respectively. Definitions of the time sectors are given in the text .....	88
4.10	The same as in Figure 4.9 but for the PFISR-B conjunctions .....	89
4.11	Medians of the ratio $N_e^{Swarm}/N_e^{PFISR}$ as a function of the electron density measured by PFISR $N_e^{PFISR}$ . The bins of $N_e^{PFISR}$ have a step of $2 \cdot 10^{10} \text{ m}^{-3}$ . Vertical bars for each bin are the median value of the ratio $\pm$ one standard deviation of the ratio. Red and blue colors characterize data for PFISR conjunctions with Swarm AC and Swarm B, respectively .....	90
4.12	(a) A contour plot for the occurrence of the ratio $R = N_e^{Swarm}/N_e^{PFISR}$ for Swarm AC versus year of radar-satellite conjunctions. The ratio is scaled according to the bar at the top of each plot. Black circles are F10.7-cm radio flux (given in s.f.u. units). The scale for the radio flux is given on the right. (b) The same as (a) but for Swarm B satellite .....	91

- 4.13 Medians of the ratio  $R = N_e^{Swarm}/N_e^{PFISR}$  as a function of the F10.7-cm radio flux (given in s.f.u. units) for joint PFISR-Swarm measurements from 2014 to 2016. Red and blue colors characterize PFISR conjunctions with Swarm AC and Swarm B, respectively. Bins of F10.7-cm radio flux have a step of 20 s.f.u. Typical standard deviations for  $R$  over all flux bins are shown by vertical lines, on the right. Sloped solid lines are linear fits and parameters of the fit are given in the top left corner. Sloped dashed lines are the linear fit lines as reported by Xiong et al. (2022) 92
- 4.14 (a) A scatter plot for the occurrence of ratio  $R = N_e^{Swarm}/N_e^{PFISR}$  for Swarm AC versus UT time of radar-satellite conjunctions. The scale for  $R$  is represented by the bar at the top. The overlaid black-white triangles are the hourly medians of the  $R$  values. The overlaid red line is the occurrence of low electron densities,  $N_e^{PFISR} < 3 \cdot 10^{10} \text{ m}^{-3}$ , given in percent of the total number of measurements for each one-hour bin. The scale for the occurrence is shown on the right (y) axis. (b) The same as (a) but for the PFISR-B conjunctions ..... 93

# Abbreviations

ACF	Autocorrelation function
AEU	Antenna element unit
AMISR	Advanced Modular Incoherent Scatter Radar
CADI	Canadian Advanced Digital Ionosonde
COSMIC	Constellation Observing System for Meteorology, Ionosphere, and Climate
E-CHAIM	Empirical-Canadian High Arctic Ionospheric Model
EISCAT	European Incoherent Scatter Scientific Association
ESA	European Space Agency
EUV	Extreme ultraviolet
F10.7-cm flux	Solar radiation flux at 10.7 cm
GLAT	Geographic latitude
GPS	Global Positioning System
HF	High frequency
HG	High gain
HM	Harmonic mode
IDL	Interactive Data Language
IMF	Interplanetary Magnetic Field
IPY	International Polar Year
IRI	International Reference Ionosphere
ISR	Incoherent scatter radar
I-V	Current-Voltage
LG	Low gain
LP	Langmuir probe
MLT	Magnetic Local Time
OML	Orbital motion limited
PFISR	Poker Flat Incoherent Scatter Radar
PFISR-AC	PFISR and Swarm A and C
PFISR-B	PFISR and Swarm B
RISR	Resolute Bay Incoherent Scatter Radar
RISR-AC	RISR and Swarm A and C
RISR-C	Resolute Bay Incoherent Scatter Radar-Canada
RISR-N	Resolute Bay Incoherent Scatter Radar-North
RO	Radio occultation
SAL	Sheath area limited
SIDC	Solar Influences Data Analysis Center
SM	Sweep mode

SNN	Solar sunspot number
SRI	Stanford Research Institute
SuperDARN	Super Dual Auroral Radar Network
TEC	Total Electron Content
TII	Thermal Ion Imager
UT	Universal Time
WA	Winter Anomaly

# Symbols

The subscript  $\alpha$  is either  $e$  to indicate electrons,  $i$  to indicate ions, or  $n$  to indicate neutrals for the variables below.

$N_e^{1min}$	1-min resolution ISR electron density data
$N_e^{5min}$	5-min resolution ISR electron density data
$h$	Altitude
$X$	Amplitude of received signal
$\psi$	Angle between direction of electron field and observer
$\omega$	Angular frequency
$A$	Area of a Langmuir probe
$V_b$	Bias voltage
$k_B$	Boltzmann constant
$e$	Charge of an electron
$\Omega_\alpha$	Charged particle gyro frequency
$\alpha_{eff}$	Coefficient dependent on component's density and reaction rate
$\beta$	Coefficient dependent on the mass of neutral particles
$r$	Correlation coefficient
$f_0F2$	Critical frequency of the F2 layer
$\sigma_v$	Cross section for energy backscatter
$\sigma_i$	Cross-sectional area of ionization
$\lambda_D$	Debye length
$N_D$	Debye sphere
$D_{300km}$	Difference between 1-min and 5-min electron density data at 300 km
$D_{450km}$	Difference between 1-min and 5-min electron density data at 450 km
$D_p$	Diffusion coefficient for collisional plasma
$d$	Distance
$V_{\vec{E} \times \vec{B}}$	$\vec{E} \times \vec{B}$ drift velocity
$\beta_0$	Effective loss rate at the reference height
$E$	Electric field magnitude
$\vec{E}$	Electric field vector
$\phi$	Electric potential
$I_e$	Electron contribution to total current measured by a Langmuir probe
$N_e^{ISR}$	Electron density measured by an ISR instrument
$N_e^{PFISR}$	Electron density measured by PFISR radar
$N_e^{RISR}$	Electron density measured by RISR radar
$N_e^{Swarm}$	Electron density measured by Swarm satellites

$f_p$	Electron plasma frequency
$\omega_{pe}$	Electron plasma frequency (angular)
$v_{e,th}$	Electron thermal speed
$V_f$	Floating potential
$a_g$	Gravitational acceleration
$A$	Half-wavelength of a radar
$z$	Height
$z_m$	Height of maximum electron-ion production
$h_m F2$	Height of the maximum density in the F2 layer
$I$	Intensity of solar radiation
$E_i$	Ion ram energy
$C$	Ionization efficiency
$L$	Loss rate of electron-ion pairs
$B$	Magnetic field magnitude
$\vec{B}$	Magnetic field vector
$N_m F2$	Maximum electron density of the F2 layer
$z_{m,0}$	Maximum production height for a solar zenith angle of 0
$q_m$	Maximum production rate of electron-ion pairs
$\mu$	Median
$N_{nm}$	Neutral density at maximum ionization
$n$	Number of data points
$s$	Number of distinct sunspots
$g_s$	Number of isolated groups of sunspots
$r, g, H_0$	Parameters of the NeQuick model
$q_\alpha$	Particle charge
$\nu_\alpha$	Particle collision frequency
$N_\alpha$	Particle density
$N_{\alpha,0}$	Particle density at reference height
$m_\alpha$	Particle mass
$T_\alpha$	Particle temperature
$\epsilon_0$	Permittivity of free space
$V_p$	Plasma potential
$H_p$	Plasma scale height
$p$	Pressure
$p_0$	Pressure at the reference height
$q$	Production rate of electron-ion pairs
$s$	Propagation path
$\sigma_e$	Radar cross section of a scattering event
$r_p$	Radius of a Langmuir probe

$r_e$	Radius of an electron
$\alpha$	Recombination efficiency
$z_0$	Reference height
$I_{as}$	Saturation current
$K$	Scale factor for sunspot number computation
$H$	Scale height
$a$	Slope of linear fit line
$I_{\infty}$	Solar radiation intensity at the source
$I_m$	Solar radiation intensity where maximum ionization occurs
$\chi$	Solar zenith angle
$V_s$	Spacecraft potential
$u_i$	Speed of ions relative to a satellite
$\sigma$	Standard deviation
$R$	Swarm measured electron density over PFISR measured electron density
$t$	Time
$\tau$	Time delay
$I$	Total current measured by a Langmuir probe
$z_t$	Transition height
$b$	Vertical offset of linear fit line
$k$	Wave number
$\lambda$	Wavelength

# Chapter 1

## Introduction

The Earth's atmosphere consists not only of neutral molecules and atoms, but also electrons and positively charged ions. Charged particles are present in the atmosphere because of the ionization of neutral particles by the Sun's radiation, precipitation of high energy particles at high latitudes, and charged particle transport supported by neutral winds and/or particle motion in external electric and magnetic fields constantly present in the near Earth's space. Although the number of charged particles near the Earth's surface is negligibly small, it becomes noticeable starting from altitudes of ~50 km (Rishbeth & Garriott, 1969). This globally distributed shell of space with enhanced charged particle content is known as the ionosphere. It extends roughly from ~50 km to ~1000 km.

The presence of charged ionospheric particles results in many interesting phenomena such as the aurora borealis and alike but, more importantly, the particles affect the operation of various practical systems on the ground and in space. For example, ionospheric electrons can support electric currents driven by the voltage impressed on the ionosphere. These currents can generate magnetic perturbations in the near space that, in turn, can create induced currents in electrical systems and can even damage them (Buzulukova & Tsurutani, 2022). Fortunately, these events do not occur often (e.g., Riley, 2012; see also a WEB report at <https://www.space.com/12584-worst-solar-storms-sun-flares-history.html>).

The ionosphere has been studied for almost a century with a variety of instruments, on the ground and, more recently, in space (e.g., Hargreaves, 1992, Hunsucker, 1991; Schunk & Nagy, 2009). Over the last several decades, attempts have been made to create global empirical models of the electron density distribution in the Earth's ionosphere (Huba et al., 2014). Computer modeling of the ongoing physical and chemical processes is another way of studying the ionosphere (e.g., Huba et al., 2014). Researchers realized that the Earth's ionosphere affects the entire chain of electrical connections between the Sun and the Earth, making it a critical domain in solar-terrestrial physics (Mishin & Streltsov, 2021).

Despite significant progress in assessing the Earth's ionosphere and understanding the various processes in it, current knowledge in this area is still limited for reliable operation of

modern technologies and for forecasting harmful space weather events. One example is the need for stable operation of high frequency (HF) communication systems in the High Arctic (e.g., Hervás et al., 2020). Further work on the physics of the formation of the ionosphere is highly desired.

This chapter will briefly introduce the major elements of the Sun-Earth system with focus on the Earth's ionosphere, the major topic of this thesis. The information provided is based on the following books: Brekke (2013), Kelley (2009), Hargreaves (1992), Hunsucker (1991), Kivelson & Russell (1995), Cravens (1997) and Schunk & Nagy (2009).

## 1.1 Plasma, major concepts

Ionospheric electrons and ions form a matter called plasma. The ionospheric plasma is partially ionized such that the amount of charged particles is smaller than the number of neutrals. At larger distances from the Earth, on the order of one Earth radius, the neutral particles almost vanish, and the plasma is fully ionized. The Sun, its atmosphere, and the entire space between the Sun and the Earth is filled with fully ionized plasma.

A fundamental property of plasma is an equal amount of positive and negative charges, known as the quasi-neutrality condition (Kelley, 2009; Cravens, 1997). Another critical property of plasma is that the motion of individual particles is affected by the collective motion of other particles in its vicinity so that a plasma is not simply a collection of electrons and ions in equal amounts, such as in an ionized gas. To understand the difference between an ionized gas and a plasma, the concept of the Debye length is helpful.

### 1.1.1 Debye length

The Debye length is an important parameter for differentiating a group of charged particles between a plasma and an ionized gas. Consider a single positive ion with charge  $q_i$ . The electrostatic potential created by the ion is proportional to  $q_i/d$ , where  $d$  is the distance from the ion. If the ion is in a gas containing electrons and other positive ions, the electrons will be attracted to this test ion and collectively they will affect its potential. It can be shown that the potential  $\phi$  of the test ion is given by (Kivelson & Russell, 1995)

$$\phi = \frac{q_i \exp(-d/\lambda_D)}{4\pi\epsilon_0 d} \quad (1.1)$$

where  $q_i$  is the charge of the test ion,  $d$  is the distance from the test ion,  $\epsilon_0$  is the permittivity of free space and  $\lambda_D$  is the Debye length given by

$$\lambda_D = \left( \frac{\epsilon_0 k_B T_e}{N_e e^2} \right)^{1/2} \quad (1.2)$$

where  $\epsilon_0$  is the permittivity of free space,  $k_B$  is the Boltzmann constant,  $T_e$  is the electron temperature,  $N_e$  is the electron density in the gas or plasma, and  $e$  is the electron charge. The potential given by equation 1.1 decreases almost exponentially at distances larger than several Debye lengths from the ion. Electrons or positive ions placed much farther than the Debye length in a plasma will experience almost zero electric field created by the test ion and are said to be “shielded”. Thus, the Debye length gives an estimate of the scale over which an ion placed in a plasma can influence surrounding particles (Kivelson & Russell, 1995). For the ionospheric plasma, the Debye length is  $\sim 1$  cm. The shielding effect implies that to study scatter from individual electrons, the radar wavelength must be smaller than  $\lambda_D$ . If the radar wavelength length is larger than  $\lambda_D$ , then the detected scatter is from density fluctuations in the plasma (Schunk & Nagy, 2009).

A sphere with a radius of  $\lambda_D$  centered on an ion in a plasma is referred to as the Debye sphere (Kivelson & Russel, 1995). The number of particles within the Debye sphere  $N_D$  is

$$N_D = \frac{4\pi N_e \lambda_D^3}{3} \quad (1.3)$$

where  $N_e$  is the electron density and  $\lambda_D$  is the Debye length. For the shielding effect to occur, the number of particles within the Debye sphere must be large. For a gas composed of charged particles to behave as a plasma,  $N_D \gg 1$  (Kivelson & Russel, 1995). Equations 1.2 and 1.3 indicate that a combination of low electron density and high temperature is required for a plasma.

## 1.1.2 Langmuir waves and plasma frequency

An important property of plasma is that it can support various types of oscillations and waves. Under a thermal equilibrium condition, plasma waves exist for a short period of time because they give away more energy to particles than they gain from particles' motion (Mishin & Streltsov, 2021).

One of the simplest waves supported by plasma are Langmuir waves, which occur due to pure electron motions. Electron plasma waves are high frequency electrostatic waves that propagate in the direction of the magnetic field in a magnetized plasma (Schunk & Nagy, 2009). For other propagation directions, the dispersion properties of Langmuir waves are modified, and electron gyro frequency contributions become noticeable (Pradipta, 2006). Since the waves are high frequency, ion motion does not contribute to the wave dynamics because their mass is much larger than that of electrons (Schunk & Nagy, 2009). The dispersion relation for the Langmuir waves is given by (Schunk & Nagy, 2009)

$$\omega^2 = \omega_{pe}^2 + 3v_{e,th}^2 k^2 \quad (1.4)$$

where  $\omega_{pe}$  is the electron plasma frequency,  $k$  is the wave number ( $k = 2\pi/\lambda$ ), and  $v_{e,th}$  is the mean thermal speed of the electrons given by

$$v_{e,th} = \sqrt{\frac{k_B T_e}{m_e}} \quad (1.5)$$

where  $k_B$  is the Boltzmann constant,  $T_e$  is the electron temperature, and  $m_e$  is the electron mass ( $m_e = 9.11 \cdot 10^{-31}$  kg). The electron plasma frequency characterizes the oscillation frequency of electrons in response to variations in the electric field; it is given by (Schunk & Nagy, 2009)

$$\omega_{pe} = \left( \frac{N_e e^2}{\epsilon_0 m_e} \right)^{1/2} \quad (1.6)$$

where  $N_e$  is the electron density,  $e$  is the electron charge,  $\epsilon_0$  is the permittivity of free space, and  $m_e$  is the electron mass. In a cold plasma ( $v_{e,th} = 0$ ), the wave does not propagate through the plasma and represents electric field oscillations in a localized region (Schunk & Nagy, 2009).

The electron plasma frequency is proportional to the square root of the electron density and can be estimated using  $f_p = \omega_{pe}/2\pi \simeq 8.98 N_e^{1/2}$ , where the electron density  $N_e$  is given in units of  $m^{-3}$ , and the plasma frequency  $f_p$  is in Hz. For conditions in the Earth's ionosphere, this frequency is on the order of  $10^6$  Hz.

The relationship between  $f_p$  and  $N_e$  is used in measurements of the electron density in the ionosphere with ionosondes (Schunk & Nagy, 2009). An ionosonde transmits radio waves vertically into the ionosphere and the waves with a frequency less than the plasma frequency will be reflected while those with a frequency greater than the plasma frequency will propagate through the ionosphere and will not return to a ground receiver. The largest frequency at which a radio

wave is still reflected is called the critical frequency and it is equal to the plasma frequency (Schunk & Nagy, 2009). Thus, the maximum electron density in the ionosphere can be determined from the maximum frequency that is reflected back towards the instrument (Schunk & Nagy, 2009). This maximum density ( $N_mF2$ ) in the ionosphere occurs at the F2 layer peak (Section 1.4.1) and corresponds to the critical frequency of the F2 layer ( $f_oF2$ ).

### 1.1.3 $\vec{E} \times \vec{B}$ drift of plasma

Another important property of plasma in the Sun-Earth system is its bulk motion, known as the  $\vec{E} \times \vec{B}$  drift, which occurs because of the presence of crossed electric  $\vec{E}$  and magnetic  $\vec{B}$  fields. If only a magnetic field exists, charged particles will gyrate around magnetic field lines with frequency  $\Omega_\alpha = eB/m_\alpha$ , where  $e$  is the electron charge,  $B$  is the magnetic field strength, and  $m_\alpha$  is the mass of the charged particle. In the presence of an electric field crossed with the magnetic field, the gyration is accompanied with the overall directional shift of particles with the velocity

$$V_{\vec{E} \times \vec{B}} = \frac{\vec{E} \times \vec{B}}{B^2} \quad (1.7)$$

where  $E$  and  $B$  are the electric and magnetic fields, respectively. In the ionospheric plasma, collisions modify the expression in equation 1.7, but at heights above  $\sim 130$  km, the collision frequency of electrons and ions with each other and neutrals is smaller than the gyro frequency for both electrons and ions, implying that the collisional terms in the equations of motion for charged particles (Kelley, 2009) can be dropped, so that both electrons and ions move in the  $\vec{E} \times \vec{B}$  direction with the same velocity (equation 1.7). This motion is often referred to as the plasma “convection” (Kivelson & Russel, 1995). For typical conditions in the Earth’s ionosphere,  $B = 5 \cdot 10^{-5}$  T,  $E = 20$  mV/m (Ghezalbash, 2013), and  $|V_{\vec{E} \times \vec{B}}| = 400$  m/s.

## 1.2 The Sun, solar wind and IMF

The Earth’s ionosphere is only one domain involved in the electrical interaction between the Earth and the Sun. Outside the ionosphere, in space where plasma consists of mostly electrons and protons (experiencing negligible collisions), the motion of charged particles is highly controlled by the Earth’s magnetic field. This region is known as the Earth’s magnetosphere. The magnetosphere is a cavity formed as the plasma emanating from the Sun, through the solar wind

and embedded in its magnetic field, termed Interplanetary Magnetic Field (IMF), are both interacting with the Earth's magnetic field.

The solar wind is blowing continuously because the plasma pressure in the near Sun environment is higher than that in the surrounding space, as was originally suggested by E. Parker (e.g., Parker, 1959; Brekke, 2013; Cravens, 1997). At the distances where Earth orbits, the solar wind electron density is about several electrons per cubic centimeter and the IMF strength is on the order of several nT (Brekke, 2013; Kivelson & Russel, 1995). Due to the dynamic pressure of plasma flow and IMF magnetic pressure, the front side of the Earth's magnetic field dipole (facing the flow) is squeezed. The tail part of the Earth's magnetic dipole, being pushed outwards by the solar wind flow and IMF, is stretched away. Simultaneously, momentum and energy of the flow are transferred to the magnetospheric particles. These processes are called the quasi-viscous interaction of the solar wind and the Earth's magnetic field.

As the solar wind plasma flows around the Earth's magnetic field, the IMF lines are bent because the magnetic field is "frozen" in the solar wind magnetoplasma in the absence of charged particle collision. The frozen-in condition (Kivelson & Russel, 1995) states that the magnetic flux through a certain surface is conserved so that restructuring of the plasma flow tube leads to reconfiguration of the magnetic field geometry as well.

The interaction of the IMF/solar wind and the Earth's magnetic field also occurs through other types of processes known as magnetic merging and reconnection (Kivelson & Russel, 1995). It is believed that upon close contact of the IMF lines and the Earth's magnetic field line of opposite polarity, the annihilation of the magnetic fields occurs so that new magnetic field lines, in the southern and northern hemispheres, are created. These lines are extensions of the Earth's magnetic field line into infinity (large distances). These newly created magnetic field lines are carried by the solar wind to the magnetotail where reconnection occurs, resulting in development of outgoing IMF field line travelling into outer space and a closed field line forming the closed and stretched dipole magnetic field lines in the magnetotail.

The rates of the magnetic merging and reconnection processes are not the same, and particles are accumulated in the magnetotail. These particles, under the pressure gradient between the magnetotail and the Earth move toward the Earth within the magnetosphere, notably in the near equatorial plane of the Earth's magnetic dipole configuration. Due to several processes, the particles are energized as they approach the Earth and eventually become trapped in the radiation

belts, forming a magnetic bottle configuration with particles bouncing between the conjugate ionospheres. Under certain conditions, the energetic particles of the radiation belts precipitate into the upper atmosphere causing the creation of many electron-ion pairs. This is an important source of ionospheric plasma at relatively high latitudes.

Another effect of particle precipitation is agitation of atmospheric molecules and atoms. The energetic particles returning to their ground state emit photons perceived on the ground and in space as the aurora. The region with the highest probability of aurora occurrence is known as the auroral oval (e.g., Feldstein, 2016). Figure 1.1 is a sketch of the auroral oval configuration (yellow belt) for moderately disturbed conditions in the Sun-Earth system.

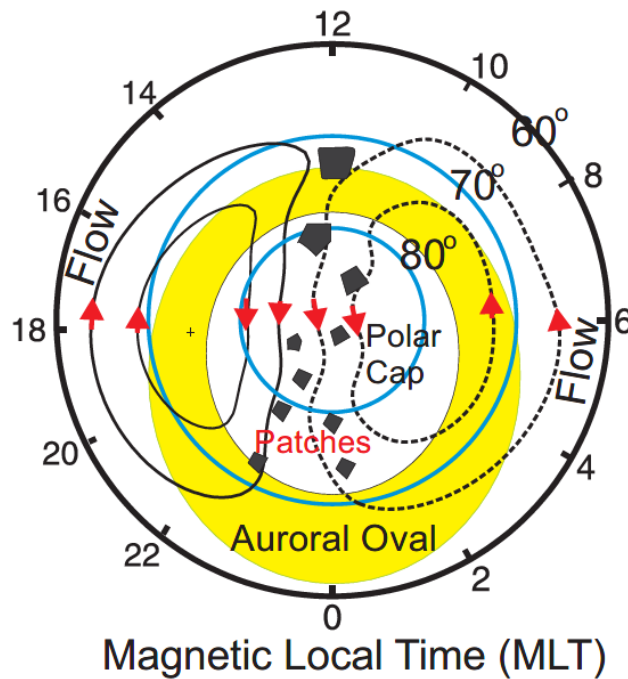


**Figure 1.1:** A sketch showing the auroral oval (Feldstein, 2016), yellow belt. Blobs of enhanced plasma, shown by black dots, are polar cap patches travelling from the dayside to the nightside with the bulk of the plasma. The plasma flow pattern at high latitudes is represented by two global-scale cells. The plot is given in magnetic local time-magnetic latitude coordinates (Kivelson and Russel, 1995). The plot was modified from that given by Larson (2021).

The aurora oval shown in Figure 1.1 is given in magnetic coordinates (see, for example, Kivelson & Russel, 1995). This is a tradition in space physics because particle motions and precipitation regions are governed by the Earth’s magnetic field. The auroral oval is located at higher magnetic (and geographic) latitudes on the dayside (12 MLT, Magnetic Local Time) compared to the nightside (00 MLT). An observer or instrument on the ground at a geographic

latitude of  $70^\circ$  N will be underneath the auroral oval during the night, and outside of the oval during the day. The region poleward of the auroral oval is called the polar cap, and the regions just equatorward of the auroral oval are called subauroral regions.

An important property of the auroral oval is that the magnetic field lines inside the oval, in the polar cap, are stretched far into space and particles from the magnetotail cannot reach the atmosphere. This leaves this region of the ionosphere void of plasma creation caused by particle precipitation, and the plasma in the polar cap is less dense than that in other regions around the globe. However, strong “islands” of dense plasma, known as polar cap patches, are still present here. This happens because the dense plasma from the middle latitudes can be transported here via the  $\vec{E} \times \vec{B}$  drift. The most frequent pattern of plasma flow in the polar cap is from mid-latitudes on the dayside toward the magnetic pole and the nightside with the return flow at much lower latitudes, as shown in Figure 1.1.

## 1.3 Solar activity cycles and their characterization

The Sun is known as a constantly changing star in terms of its electromagnetic radiation and fluxes of particles emerging from its environment (Brekke, 2013; Cravens, 1997). The impact of solar activity is traditionally characterized by two indices, the solar sunspot number (SSN) and the solar radiation flux at 10.7 cm (F10.7-cm flux).

### 1.3.1 Sunspot number

The sunspot number SSN is an index of the Sun’s activity inferred from observations of the entire visible disk of the Sun (Brekke, 2013). It is determined daily by counting the number of distinct spots, denoted as  $s$ , and isolated groups or clusters of the spots, denoted as  $g_s$ , and the SSN index is computed as  $K \cdot (10g_s + s)$  (e.g., Kivelson & Russel, 1995). The scale factor  $K$  (usually less than unity) depends on the observatory and is intended to adjust to the scale originated by Wolf (Wolf’s SSN). Originally, long term observations had been carried out in Zurich, but currently International Sunspot Numbers result from a statistical treatment of the data originating from a network of more than twenty-five observing stations, with the Locarno (Switzerland) station as the reference station, to guarantee continuity with the past SNN values reported from Zurich. The SSNs are produced

by the Solar Influences Data Analysis Center (SIDC), World Data Center for the Sunspot Index, at the Royal Observatory of Belgium (<https://www.sidc.be/silso/>).

### 1.3.2 F10.7-cm radio flux

Solar activity can also be characterized by measurements of the radio flux of electromagnetic radiation from the Sun at 10.7 cm (2800 MHz). F10.7-cm radio flux has been measured since 1947, and it is currently measured at the Dominion Radio Astrophysical Observatory, near Penticton, BC in Canada ([https://www.ngdc.noaa.gov/stp/space-weather/solar-data/solar-features/solar-radio/noontime-flux/penticton/documentation/dataset-description\\_penticton.pdf](https://www.ngdc.noaa.gov/stp/space-weather/solar-data/solar-features/solar-radio/noontime-flux/penticton/documentation/dataset-description_penticton.pdf)). Measurements are made around local noon (20:00 UT, Universal Time) using 1.8 m paraboloidal antennas. The measured values are expressed in solar flux units ( $1 \text{ s.f.u.} = 10^{-22} \text{ W}\cdot\text{m}^{-2}\cdot\text{Hz}^{-1}$ ). The measured values are affected by the changing distance between the Earth and Sun throughout the year and usually are not considered over the adjusted values that are also available.

### 1.3.3 Solar Cycles

The Sun shows multiple periodicities (e.g., Kane, 2002; Kontor, 1993; Usoskin, 2017) with the most important being the 11-year cycle (Brekke, 2013; Kivelson & Russel, 1995). Figure 1.2 shows daily values of SSN (Figure 1.2a) and F10.7-cm flux (Figure 1.2b) from 1965 to 2022. The maxima of both indices were achieved in approximately 1968, 1980, 1991, 2001/2002 and 2014/2015, which is roughly every 11 years and the maximum of each cycle varies in magnitude. The last solar cycle, known as solar cycle 24, was the weakest in recent history, shown by the maximum reached in 2014/15 in Figure 1.2. The solar minima have about the same magnitudes irrespective of the magnitude of the previous or next maximum.

The peaks in SSN and F10.7-cm flux do not coincide exactly in time, indicating that there is not one-to-one agreement between the indices. To support this conclusion, Figure 1.2c plots SSN versus F10.7-cm flux. Although generally a linear dependence is visually identifiable, the correlation coefficients between the two indices is only 0.84. For studies of the Earth's ionosphere, the F10.7-cm flux index is usually considered, see Space Weather Canada at <https://spaceweather.ca/index-en.php> or the USA National Oceanic and Atmospheric Administration, Space Weather Prediction Center website at <https://www.swpc.noaa.gov>.

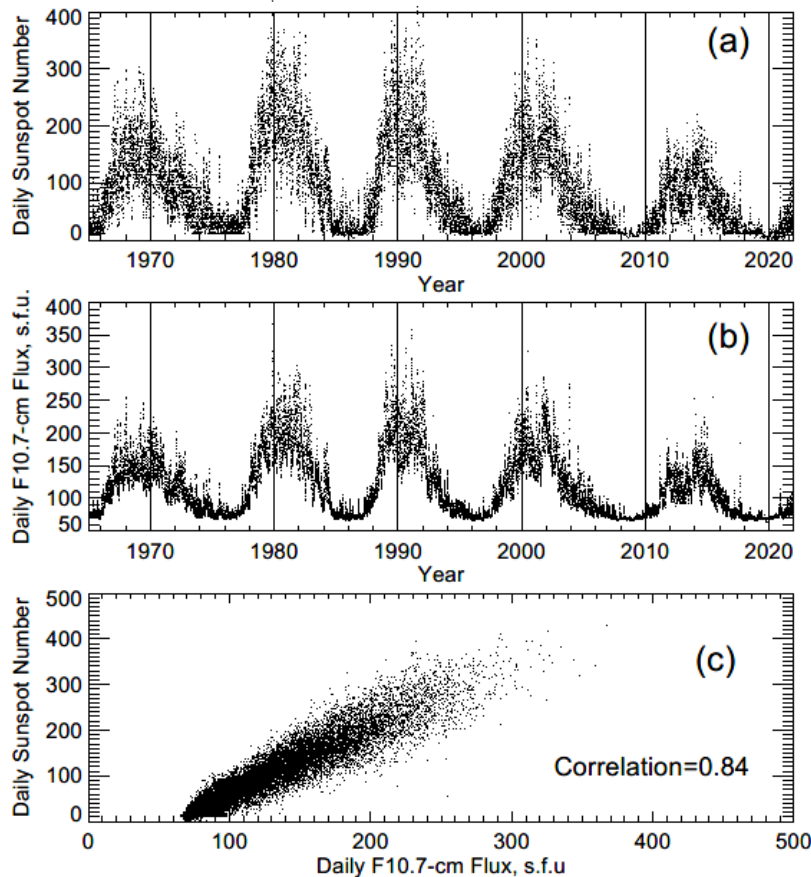


**Figure 1.2:** Daily values of (a) the sunspot number (SSN) and (b) the F10.7-cm solar radiation flux from 1965 to 2022. (c) Scatter plot of SSN versus F10.7-cm flux. The correlation coefficient between the two indices is shown in the bottom left corner. The data were taken from <https://omniweb.gsfc.nasa.gov/form/dx1.html> (last accessed 7 May 2022).

## 1.4 The Earth’s ionosphere

The electron density distribution in the ionosphere shows very complicated patterns of spatial and temporal variations (Brekke, 2013; Kivelson & Russel, 1995; Schunk & Nagy, 2009). This section will discuss the shape and formation of Earth’s ionosphere.

### 1.4.1 Ionospheric layers

The ionosphere is traditionally broken up into three distinct layers/regions (Schunk & Nagy, 2009) which are the D layer (50 to 90 km), the E layer (90 to 150 km), and the F layer (150 to 1000+ km). Figure 1.3 gives examples of the height electron density profiles based on the International

Reference Ionosphere (IRI) model (Bilitza, 2018) for 74.7°N and 94.9 °W, which are the coordinates of Resolute Bay (Canada), one of the regions of interest in this thesis. During the period of high solar activity (2013), the maximum electron density at the F region peak is larger than the maximum density observed during periods of low solar activity (2018) by a factor of ~1.5 during daytime and ~3 at nighttime. One can also notice larger daytime electron densities when comparing to the nighttime electron densities.

The F layer is often split into the lower F1 layer (present only during daytime) and F2 layer. The modeled electron density profile in Figure 1.3 does not show an F1 layer; it is not always present at high latitudes. The E layer at ~100 km altitude is seen during the day. This thesis is focused on the F2 layer and above (the topside ionosphere).

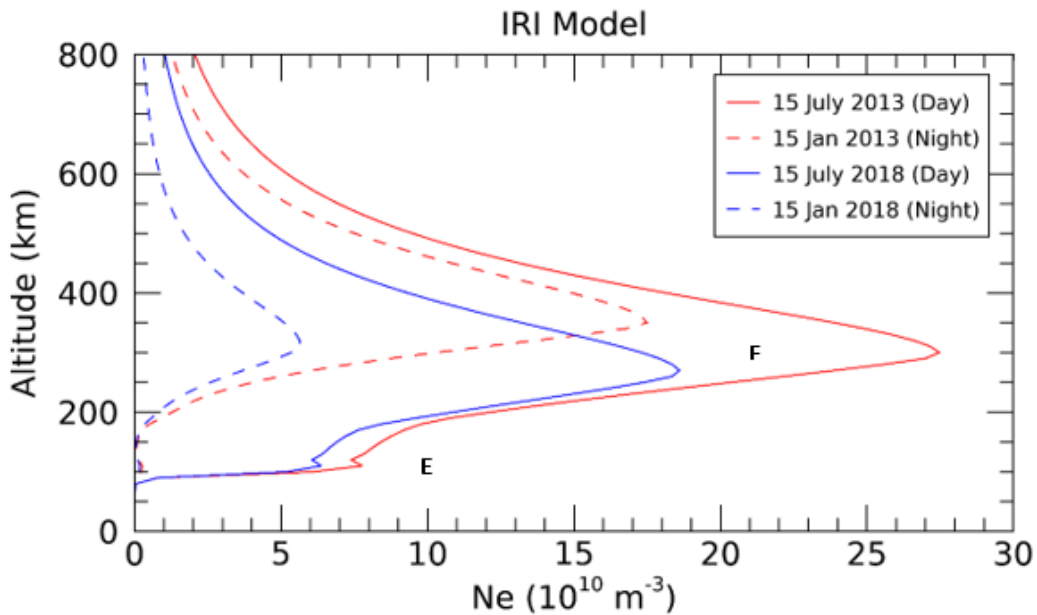


**Figure 1.3:** Electron density profiles over Resolute Bay, Canada in the ionosphere according to the IRI model (Bilitza, 2018). The solid traces are for a day ionosphere and the dashed traces are for a night ionosphere. Red and blue traces correspond to predictions for high (2013) and low (2018) solar activity, respectively.

### 1.4.2 Neutral atmosphere

The Earth’s ionosphere is created by ionization of atmospheric neutral particles that dominate over charged particles up to heights of ~1000 km. The shape of the electron density profile is controlled, to a significant extent, by the distribution of neutrals with height. The major neutral components at the ionospheric heights are N<sub>2</sub>, O<sub>2</sub>, and O, with N<sub>2</sub> dominating at heights below ~250 km and O

dominating above ~250 km (Brekke, 2013). In the topside ionosphere, He and H atoms become more abundant and H atoms dominate at heights above ~1000 km (Brekke, 2013).

The major force acting on neutral particles is the gravitational force. For the particles to be in a static equilibrium, the gravitational force must be balanced by a net pressure force acting on a parcel of air from its top and bottom. The change in pressure  $p$  over height  $z$  is given by (Brekke, 2013)

$$\frac{dp}{dz} = -N_n m_n a_g \quad (1.8)$$

where  $N_n$  is the density of the molecules,  $m_n$  is the mass of the molecules, and  $a_g$  is the gravitational acceleration. If the atmosphere is assumed to be an ideal gas, the pressure  $p = N_n k_B T$  as a function of height  $z$  can be derived from (1.8) as

$$p = p_0 \exp\left(-\frac{z - z_0}{H}\right) \quad (1.9)$$

where  $H = k_B T / m_n a_g$  is the scale height and  $p_0$  is the pressure at a reference height  $z_0$ . The typical scale height for the atmospheric neutral species is ~8.5 km (Brekke, 2013). According to (1.9), the pressure in the atmosphere decays exponentially with height. If the atmosphere is assumed to be isothermal, the molecule density  $N_n$  at a given height  $z$  is

$$N_n = N_{n,0} \exp\left(-\frac{z - z_0}{H}\right) \quad (1.10)$$

where  $N_{n,0}$  is the neutral density at reference height  $z_0$  and  $H$  is the scale height. The density of molecules in the atmosphere also decreases exponentially with height.

### 1.4.3 Chapman theory of ionization

Two sources for ionization of the neutral gas in the Earth's upper atmosphere are solar irradiation, mostly in the extreme ultraviolet (EUV) part of the electromagnetic spectrum, and energetic particle precipitations, which are important at high latitudes (Brekke, 2013). For ionization to occur, the supplied energy must be above the potential of ionization of ~36 eV (Kivelson & Russel, 1995) which is easily delivered by the Sun's photons or precipitating particles.

#### **Ionization by sunlight**

Ionization by sunlight can be described by the Chapman theory (Brekke, 2013). The Chapman theory assumes that as the light travels down through the atmosphere towards the Earth, the

intensity of light decreases as its energy is lost on ionization of neutral particles (creating electron-ion pairs) and eventually totally lost as the light reaches the progressively denser atmosphere. The reduction of the solar radiation intensity  $I$  per unit distance  $s$  is given by (Brekke, 2013)

$$\frac{dI}{ds} = -N_n \sigma_i I \quad (1.11)$$

where  $N_n$  is the density of neutral particles and  $\sigma_i$  is the cross-sectional area of ionization.

The production rate of electron-ion pairs  $q$  created through ionization from solar radiation is given by (Brekke, 2013)

$$q = CN_n \sigma_i I \quad (1.12)$$

where  $C$  is the ionization efficiency,  $N_n$  is the neutral density,  $\sigma_i$  is the cross-sectional area of ionization, and  $I$  is the solar radiation intensity. For atomic species, all the radiation energy goes into producing electron-ion pairs and  $C = 1$ . For molecules, not all the radiation energy is used for producing electron-ion pairs and  $C < 1$ . The neutral particle density in the atmosphere decreases with height (equation 1.10) while the intensity of solar radiation increases with height. Therefore, at some height the number of neutral particles multiplied by the intensity of light will be at a maximum, and this is where the highest production of electron-ion pairs occurs (from equation 1.12,  $q \propto N_n I$ ). To find the height of maximum production, one can find the derivative of  $q$  (equation 1.12) versus propagation path  $s$  and set it to zero. Because generally the solar light propagates at a certain angle  $\chi$  with respect to the zenith, called the solar zenith angle, it is convenient to change differentiation with respect to the vertical variable  $z$  according to

$$ds = -\frac{dz}{\cos\chi} \quad (1.13)$$

where  $s$  is the propagation path of the solar radiation. Analysis of equations 1.11 and 1.13 shows that the production rate is maximized at the height of

$$z_m = z_{m,0} + H \ln(\sec\chi) \quad (1.14)$$

where  $H$  is the scale height,  $\chi$  is the solar zenith angle, and  $z_{m,0}$  is the maximum production height for an overhead sun ( $\chi = 0$ ). To find the maximum of the ionization rate  $q_m$ , equation 1.11 is solved applying the conditions at the height of maximum production, resulting in (Brekke, 2013)

$$q_m = \frac{CI_\infty}{eH} \cos\chi \quad (1.15)$$

where  $C$  is the ionization efficiency,  $I_\infty$  is the radiation intensity at the source (the Sun),  $e$  is the electron charge,  $H$  is the scale height, and  $\chi$  is the solar zenith angle .

The expression for the production rate as a function of height is obtained by considering the height variation of the neutral density according to equation 1.10 and the exponential variation of the radiation intensity  $I$  with respect to that at the maximum ionization  $I_m$  (Brekke, 2013)

$$I = I_m \exp\left(1 - \frac{N_n}{N_{nm}}\right) \quad (1.16)$$

where  $N_m$  is the neutral density and  $N_{nm}$  is neutral density at the maximum of ionization. The final expression for  $q$  as a function of height  $z$  can be given as (Brekke, 2013)

$$q = q_m \exp\left[1 - \frac{z - z_m}{H} - \exp\left(-\frac{z - z_m}{H}\right)\right] \quad (1.17)$$

where  $H$  is the scale height, and  $z_m$  is the height of the maximum ionization rate  $q_m$ . Both  $q_m$  and  $z_m$  in expression 1.17 depend on the solar zenith angle in a such a way that the production rate at a given height is greatest for an overhead sun ( $\chi = 0$ ) and decreases as the solar zenith angle increases (Brekke, 2013).

### Recombination processes

Electron-ion pairs created by ionization from solar radiation or other processes can be lost through recombination processes. There are two types of recombination processes. They are radiative recombination and dissociative recombination. The radiative recombination process occurs when the electrons directly combine with the positive ion to produce a neutral species and a photon. An example of radiative recombination is an  $O^+$  ion combining with an electron to create an oxygen atom and a photon by



The dissociative recombination process occurs when an ionic compound combines with an electron to produce the two different components of the compound. For example, an  $NO^+$  ion combining with an electron to produce a nitrogen and oxygen atom by



In the upper atmosphere dissociative recombination is more likely to occur as it has a larger recombination rate compared to radiative recombination by a factor of  $10^5$ . When electrons and positive ions are involved in recombination processes and assuming quasi-neutrality in the plasma ( $N_e = N_i$ ), the loss rate  $L$  can be approximated as (Brekke, 2013)

$$L = \alpha N_e^2 \quad (1.20)$$

where  $\alpha$  is the recombination coefficient and  $N_e$  is the electron density.

Electrons can also be lost by attaching to a neutral molecule to create a negative ion, that would interact with positive ions. The loss rate  $L$  by attachment to a molecule is given by (Brekke, 2013)

$$L = \beta N_e \quad (1.21)$$

where the coefficient  $\beta$  is dependent on the mass of neutral molecules involved in the charge exchange interaction and  $N_e$  is the electron density.

### Photochemical equilibrium

In the ionosphere, an equilibrium between electron-ion pairs production and losses is usually established. The continuity equation for an ion species is (Brekke, 2013)

$$\frac{\partial N_i}{\partial t} = q - L \quad (1.22)$$

where  $N_i$  is the density of the ion species,  $t$  is time,  $q$  is the production rate of electron-ion pairs, and  $L$  is the loss rate of ions.

For a photochemical equilibrium ( $\partial N_i / \partial t = 0$ ), the production rate  $q$  is equal to the loss rate  $L$ . Then the electron/ion density  $N_e$  can be inferred from

$$N_e = \sqrt{q/\alpha} \quad (1.23)$$

for alpha type losses where  $q$  is the production rate and  $\alpha$  is the recombination coefficient and

$$N_e = q/\beta \quad (1.24)$$

for beta type losses where  $\beta$  is the charge exchange coefficient. Equations 1.23 and 1.24 are referred to as the Chapman  $\alpha$ -profile and the Chapman  $\beta$ -profile, respectively (Brekke, 2013). These profiles are representative of the E and F1 regions, respectively.

### 1.4.4 Plasma chemistry at F region heights

The dominant ions in the F region are  $O^+$  ions (Brekke, 2013). They are produced by solar radiation. Other ions such as  $NO^+$ ,  $O_2^+$ , and  $H^+$  are also present at these heights, but they are mostly produced through chemical reactions (Brekke, 2013).

The maximum photochemical production of  $O^+$  ions (equation 1.15) is located at heights of  $\sim 200$ - $250$  km, depending on the wavelength of the solar radiation (Brekke, 2013). The resulting height distribution of the electron density, constituting an ionospheric layer, depends also on ion losses incurred owing to various chemical reactions.

The  $O^+$  ions can be lost in several ways. One possibility is radiative recombination with an electron to produce an oxygen atom and a photon (equation 1.18). As discussed in the previous Section 1.4.3, this process is slow, and the  $O^+$  ions are more likely to be lost through a chain of reactions. First, the  $O^+$  ion bonds with an  $N_2$  molecule by



and then the  $NO^+$  ion undergoes dissociative recombination (equation 1.19). Another loss process for the  $O^+$  ions is combining with a neutral  $O_2$  molecule via charge rearrangement, producing an  $O_2^+$  ion



that then undergoes a dissociative recombination to produce two oxygen atoms.



In a quasi-chemical photoequilibrium, the production of  $O^+$  ions must be equal to their losses. The loss rate of the  $O^+$  ions at large heights, above  $\sim 300$  km, is proportional to the density of neutrals which gives a beta type of loss (Brekke, 2013). Because the number of neutrals decay with height exponentially, the loss rate  $\beta$  change with height  $z$  according to (Brekke, 2013)

$$\beta = \beta_0 \exp\left(-\frac{z - z_0}{H}\right) \quad (1.28)$$

where  $\beta_0$  is the effective loss rate at a reference height  $z_0$  and  $H$  is the scale height. Since the loss rate of  $O^+$  ions decreases with height, the electron density is expected to increase with height as it follows from equation 1.24. This is the reason why the formation of the F2 layer cannot be explained by simply using the Chapman theory as in Section 1.4.3, and diffusion processes must be taken into account which will be explained in the next section.

Below 250-300 km, the charge rearrangement reactions (equation 1.26) involving the  $O^+$  ions with  $O_2$  and  $N_2$  molecules become more frequent (because of exponentially larger neutral densities at smaller heights), and they can be described by the rate  $\alpha_{eff} \cdot N_e$  where the coefficient  $\alpha_{eff}$  is a function dependent on each component's density and reaction rate (Brekke, 2013). There is a transition height  $z_t$  where  $\beta = \alpha_{eff} \cdot N_e$ . Above this height, the electron density in equilibrium is controlled by the loss rate  $\beta$ , and below this height it is controlled by the rate  $\alpha_{eff} \cdot N_e$ . If  $z_t$  occurs below the height of the maximum production of electron-ion pairs  $z_m$  (equation 1.14), there will be a ‘‘ledge’’ in the electron density profile stretched between  $z_t$  and  $z_m$ , indicating some electron density increase with height, and no ‘‘layer’’ per se will exist (Brekke, 2013). If  $z_t$  occurs above  $z_m$ ,

there will be a local maximum in the electron density profile (“knee”) at  $z_m$  and a minimum at  $z_t$  (Brekke, 2013). This “knee” in the electron density profile can be identified in measurements as the F1 layer.

### 1.4.5 Formation of the F2 Layer

Above  $\sim 200$  km, the ionosphere is not in photochemical equilibrium, and diffusion processes become important as already mentioned. The diffusion coefficient for a collisional plasma is given by (Brekke, 2013)

$$D_p = \frac{2k_B T}{m_i \nu_i + m_e \nu_e} \quad (1.29)$$

where  $k_B$  is the Boltzmann constant,  $T$  is the temperature of the plasma,  $m_i$  and  $m_e$  are the ion and electron masses, and  $\nu_i$  and  $\nu_e$  are the ion and electron collision frequencies with the neutral molecules in the ionosphere. The diffusion coefficient increases with height (smaller collision frequencies) and counteracts the electron-ion pair creation. Even though the imbalance of the photo production above  $z_m$  and recombination processes leads to an increase of electron density (see Section 1.4.4), the situation changes at heights where the diffusion process becomes dominant.

Under dominating diffusion processes, analysis of the diffusion equation (Brekke, 2013) shows that an equilibrium can be achieved if the electron density  $N_e$  varies with height  $z$  by

$$N_e = N_{e0} \exp\left(-\frac{z - z_0}{H_p}\right) \quad (1.30)$$

where  $N_{e0}$  is the electron density at  $z_0$  that can be identified in observations as the height of the F2 layer maximum. In equation 1.30, the plasma scale height  $H_p = 2H$  is double the scale height for the neutral atmosphere.

The maximum electron density is achieved at large heights because even though the photochemical production of electron-ion pairs overpowers the recombination rate at heights above  $z_m$ , the diffusion process becomes progressively stronger with height and eventually become stronger than the production rate resulting in a decrease in the electron density. The location of the peak can be approximated as the height where the recombination rate is approximately equal to the rate of diffusion, which can be estimated as  $D/H^2$  (Hargreaves, 1992).

Above  $z_0$ , according to (1.30), the electron density decreases exponentially with height. Because the F2 layer is formed under a delicate balance of recombination, photoionization, and

diffusion processes, it is very sensitive to the composition of the atmosphere, making the electron density very responsive to changes in the neutral components of the atmosphere, notably the ratio of  $O/N_2$  (Richards, 2001).

#### 1.4.6 Topside ionosphere and protonosphere

In the topside ionosphere, right above the F2 layer peak,  $O^+$  ions continue to dominate but eventually, because the  $O^+$  density decays exponentially with height,  $He^+$  and  $H^+$  ions become dominant (Brekke, 2013). Above  $\sim 1000$  km,  $H^+$  ions are the major ions (Brekke, 2013). This region is referred to as the protonosphere (Schunk & Nagy, 2009). The electron density continues to decay in the protonosphere, but slower than just above the F2 peak (Schunk & Nagy, 2009). This effect is seen in Figure 1.3 at heights above 600 km.

### 1.5 Empirical modeling of the electron density in the ionosphere, NeQuick approach

To give an example of how the electron density in the Earth's ionosphere is modeled, below is a description of a model that is often used, the NeQuick model (Nava et al., 2001; 2008; Pignalberi et al., 2018; Radicella & Nava, 2020).

The NeQuick ionospheric model is a global-scale climatological model developed for quick calculations of ionospheric parameters, for example Total Electron Content (TEC, Pignalberi et al., 2022). Currently, the model is actively investigated by researchers to understand ways to improve it for the topside electron density profiles (e.g., Pignalberi et al., 2020; 2021; 2022; Themens et al., 2018). This model is a component of the classical IRI global model of electron density (Bilitza et al., 2017; 2018; 2022) and the Empirical-Canadian High Arctic Ionospheric Model (E-CHAIM) that is expected to perform better in the Canadian Arctic (Themens et al., 2017; 2018; 2019a,b; 2021).

The NeQuick model is a semi-Epstein layer function characterized by three parameters,  $r$ ,  $g$  and  $H_0$ . Additionally, it requires knowledge of values for the peak density  $N_mF2$  and the height of the maximum density of the F2 layer  $h_mF2$ . The modeled electron density  $N_e$  can be determined at any selected altitude  $h$  from

$$N_e(h) = \frac{4N_m F2}{(1 + \exp(z))^2} \exp(z) \quad (1.31)$$

where  $z$  is the reduced height given by

$$z = \frac{h - h_m F2}{H} \quad (1.32)$$

where  $H$  is the scale height given by

$$H = H_0 \left[ 1 + \frac{rg(h - h_m F2)}{rH_0 + g(h - h_m F2)} \right] \quad (1.33)$$

where  $r$ ,  $g$ , and  $H_0$  are parameters that describe the shape of the ionosphere with respect to height.

There is an uncertainty in the selection of NeQuick model parameters, especially at high latitudes. To illustrate the effect that the parameters  $r$ ,  $g$ , and  $H_0$  have on the NeQuick representation of the ionosphere, Figure 1.4 shows examples of model-predicted electron density profiles for various combinations of values for  $r$ ,  $g$ , and  $H_0$ . The values for  $r$  were selected to be 100, the original value proposed in Nava et al. (2008), and 20, the suggestion for high-latitude profiles by Themens et al. (2018). Values for  $g$  were selected to be 0.1, 0.2, and 0.35, close to the original value of 0.125 (Nava et al., 2008) and the value suggested by Themens et al. (2018) of 0.2024. Electron density profiles for an  $r$  value of 100 are shown by the black curves and profiles for an  $r$  value of 20 are shown by the blue curves.

Figure 1.4 shows that the parameter  $r$  does not affect the profiles significantly. The  $r$  parameter is important for determining electron density at very large heights, well above the F layer peak and into the plasmasphere (Pignalbery et al., 2020). Figure 1.4 (panels g, h, and i) show some larger values of electron density at heights above 500 km for  $g = 0.35$ . Figure 1.4 indicates that parameter  $g$  affects the rate of decay of  $N_e$  in the topside ionosphere.

For larger values of  $g$ , the electron density decay is less pronounced. This parameter affects the electron density profile at heights above the F2 peak noticeably, and the selection of a specific value is less justifiable. Figure 1.4 shows that the choice of parameter  $H_0$  is very critical.  $H_0$  affects the thickness of the F2 Layer for the model. Larger values of  $H_0$  result in a thicker F2 layer, which can be judged by the span of heights where  $N_e > 0.7 \cdot N_m F2$  (shown by the vertical dashed lines in Figure 1.4). The thickness of the F2 layer increases almost proportionally with increasing  $H_0$ . For  $H_0$  values of 20 km, 50 km, and 80 km the estimated thickness of the F2 layer is roughly 50 km,

125 km, and 200 km, respectively. This strong dependence on  $H_0$  justifies the use of the fixed values for  $r$  and  $g$  suggested by Themens et al. (2018).

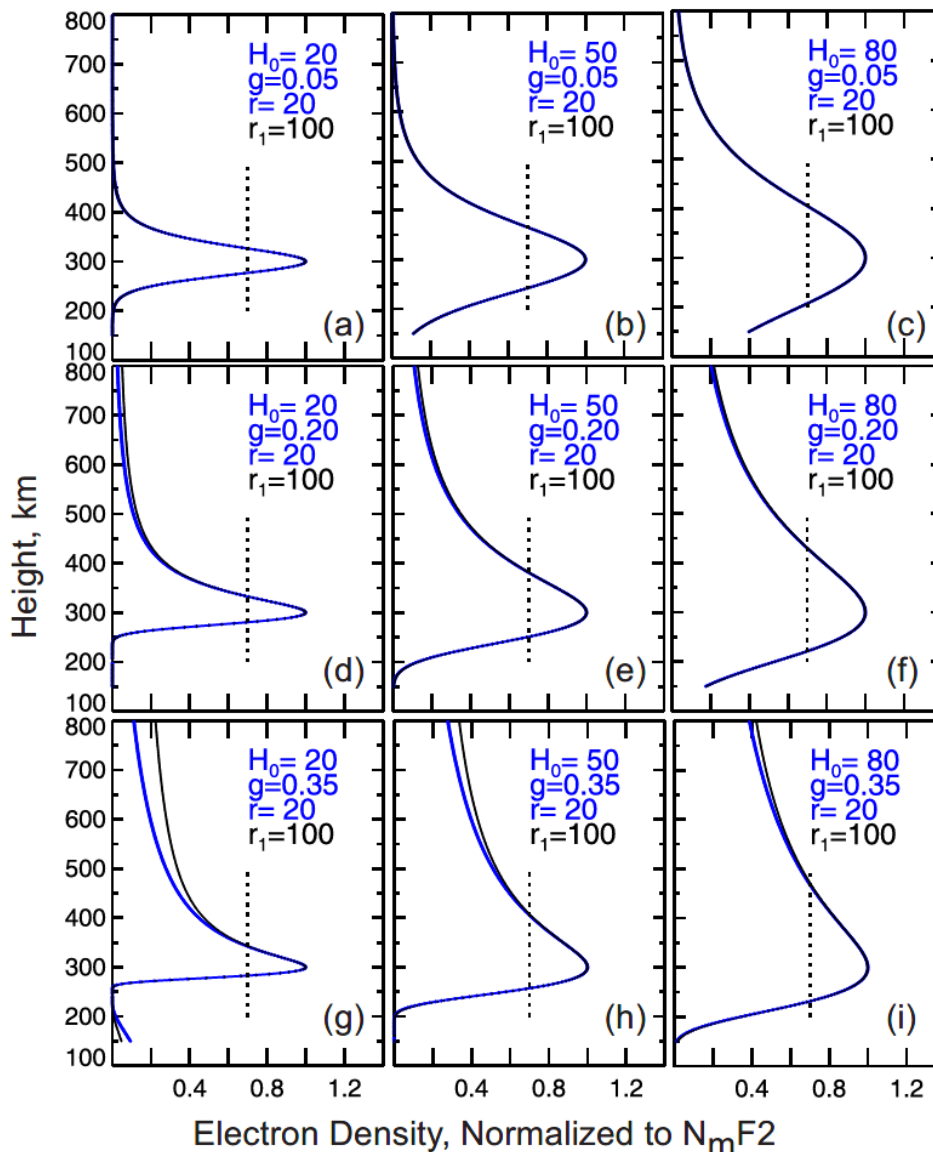


**Figure 1.4:** Electron density profiles according to the NeQuick ionospheric model for various values of parameters  $H_0$ ,  $g$  and  $r$ . The peak of the profiles was selected at 300 km. Blue lines in panels (d), (e) and (f) correspond to the “optimal” selection of parameters  $g$  and  $r$ , suggested by Themens et al. (2018). A vertical dashed line is shown in each panel intersecting where electron density is equal to 70% of the peak value,  $N_m F2$ , to assess the effective thickness of each profile.

The diagrams in Figure 1.4 illustrate that the selection of the  $H_0$  parameter is crucial for modelling electron density in the topside ionosphere. The diurnal and seasonal variations of the

parameter for the high latitude ionosphere above Alaska are investigated and discussed in Chapter 3.

## 1.6 Objectives of the thesis work

This thesis has two major objectives. The first is the investigation of the electron density distribution in the high-latitude ionosphere over one specific region, near Poker Flat, Alaska. This region was selected because a powerful incoherent scatter radar (ISR), the Poker Flat Incoherent Scatter Radar (PFISR), is located here and has been collecting electron density data since 2007. These data have been critical for the investigation of various electrodynamical processes in the high-latitude ionosphere, mostly as a single event (see, for example, the current PFISR publication list at <https://amisr.com/amisr/pubs/>). However, the data collected by PFISR are not often used for a statistical study of the average distribution in the ionosphere and short- and long-term trends important for setting up the benchmark values and thus quantitatively assessing the background space weather conditions. Knowledge on the electron density trends in the ionosphere is not only important for understanding physical processes in the ionosphere, but is also important for various applications. The area over Poker Flat is also monitored with three coherent scatter Super Dual Auroral Radar Network (SuperDARN) HF radars at Kodiak, Prince George, and Adak (Nishitani et al., 2019) providing information on the global scale  $\vec{E} \times \vec{B}$  drift of the ionospheric plasma. The combination of SuperDARN and PFISR observations might allow one to establish to what extent the electron density distribution is controlled by solar radiation, the neutral winds, and the  $\vec{E} \times \vec{B}$  transport of plasma from nearby regions. Electron density distribution in the ionosphere affects HF radio wave propagation paths, and thus occurrence of HF echoes. Ray paths are important to know for assessing HF radar performance and for planning future experiments. An important factor in starting the work with the PFISR data was the fact that the data are freely available for the space science community and help from the SRI International personnel in radar operation features was available. For this thesis, the goals of the first objective were selected as follows:

- 1.1. Investigate the diurnal and seasonal variations in the electron density height profiles for the PFISR radar area.

- 1.2. Quantitatively estimate differences in the ionospheric electron density response to a change in the solar activity level. Two years of PFISR data, corresponding to relatively high and low solar activity, were considered.
- 1.3. Implement the NeQuick (Nava et al., 2001, 2008) empirical model of the electron density distribution in the Earth's ionosphere to describe the trends in the thickness of the ionospheric F2 layer. Evaluate the consistency of the model for the topside ionosphere with measurements by the PFISR radar. These heights are of interest because of the work with the Swarm satellite data also undertaken in the thesis.

The second objective of this thesis is to investigate the reliability of electron density measurements with the Langmuir probe (LP) instruments onboard the Swarm satellites. Swarm is an Earth observation mission consisting of three satellites, Swarm A, B, and C, launched in 2013 by the European Space Agency (ESA) to study the electrodynamical parameters of the near space environment (Buchert et al., 2015; Friis-Christensen et al., 2008; Knudsen et al., 2017). All three satellites have near polar orbits (Friis-Christensen et al., 2008; Catapano et al., 2022) orbiting at heights of ~450 km (Swarm A and C) and ~510 km (Swarm B). The goal of the undertaken work is to compare Swarm electron density measurements with ISR radar measurements. This is continuation of a validation work for Swarm LPs with ISRs at high latitudes started by Larson (2021) and Larson et al. (2021). Larson et al. (2021) compared Swarm electron densities with those measured by the Resolute Bay Incoherent Scatter Radars (RISR-North and RISR-Canada). The authors selected conjunctions where the Swarm satellites were within 200 km of a radar beam. This condition is difficult to satisfy as the satellites pass close to the vicinity of the radar two times per day, at best. In addition to low data statistics, the distribution of points on the scatter plots of the ISR-Swarm electron density data made it difficult to make a robust quantitative assessment on the degree of agreement between the data. To some extent, this is because the electron density in the high latitude ionosphere is highly variable with time and space (Schunk & Nagy, 2009). In this thesis, a more traditional approach (e.g., Lomidze et al., 2018) was adopted and ISR data were averaged over multiple beams. The Swarm data were averaged over  $1^\circ$  of latitude as they passed over ISR zenith. Specific questions for investigation from the second objective of this thesis are:

- 2.1. Does the Swarm electron density under-estimation effect identified in Larson et al. (2021) for the polar cap latitudes hold while the new methodology to RISR and Swarm data handling is applied?

- 2.2. Does the Swarm electron density under-estimation effect weaken at the lower latitudes of PFISR measurements? The question comes from the fact that Lomidze et al. (2018) found a smaller underestimation effect at middle latitudes compared to the effect found by Larson et al. (2021) at high latitudes.
- 2.3. The possibility of Swarm electron density overestimations at low electron densities were mentioned by Larson et al. (2021). The effect was noticeable for  $N_e < 5 \cdot 10^{10} \text{ m}^{-3}$ . Is this a systematic effect? If yes, what are the geophysical conditions under which it exists?
- 2.4. Are there any differences in the strength of the Swarm underestimations and overestimations for the heights of ~450 km (Swarm A and C) and ~510 km (Swarm B)?

## 1.7 Thesis outline

The thesis is organized as follows. Chapter 2 describes the principles of electron density measurements in the ionosphere with ISRs and the Swarm satellites. Chapter 3 investigates variations of the electron density distribution by considering PFISR radar data for two full years of observations. It also compares PFISR measurements at ~450 km with predictions of the NeQuick ionospheric model. Chapter 4 considers joint ISR-Swarm measurements and investigates the compatibility of the instruments in the topside ionosphere. Most of the materials presented in Chapter 4 are part of a published paper:

Fast, H., A. Koustov, & R. Gillies, 2023. Validation of Swarm Langmuir probes by incoherent scatter radars at high latitudes. *Remote Sensing*, 15, 1846. <https://doi.org/10.3390/rs15071846>

Chapter 5 summarizes the work completed and gives suggestions for future work.

# Chapter 2

## Instruments

As mentioned in Chapter 1, this thesis will study the electron density distribution in the high latitude ionosphere including the topside ionosphere, at heights above 400 km. Over the years, significant information on the electron density at and below the F region peak has been obtained from ionosonde observations (e.g., Brekke; 2013; Hargreaves, 1992; Hunsucker, 1991; Schunk & Nagy, 2009). Incoherent scatter radars are another type of instrument capable of measuring electron density in the ionosphere, along with other plasma parameters, including the topside ionosphere not accessible by ionosondes (Beynon & Williams, 1978; Brekke, 2013; Schunk & Nagy, 2009; Sedgemore-Schulthess & St.-Maurice, 2001). Over the last decade, two high latitude ISRs have been in operation at Resolute Bay, Canada, RISR-Canada (RISR-C) and RISR-North (RISR-N), pointing southward toward the Canadian mainland and toward the magnetic Pole, respectively (Bahcivan et al., 2010; Gillies et al., 2016). The RISR radars operate at extreme high latitudes, in the polar cap. The Poker Flat Incoherent Scatter Radar is another high latitude ISR located in Poker Flat, Alaska. Its location is close to the auroral oval. Another type of instrument capable of measuring the electron density in the topside ionosphere is the Langmuir probe, which can be mounted on low Earth orbit satellites. One example is the European Space Agency Swarm satellites (a triad of satellites) that are equipped with two LPs each (Knudsen et al., 2017).

The following chapters of this thesis will consider data from the RISR-C radar, the PFISR radar, and the three Swarm satellites. This chapter will discuss the ISR and LP principles of operation in general, as well as give details of the specific instruments used.

### 2.1 Incoherent Scatter Radars

Incoherent scatter radars are commonly used instruments to measure plasma properties in the Earth's ionosphere. They are considered as one of the most powerful ground-based remote-sensing instruments for plasma diagnostics (Hunsucker, 1991; Schunk & Nagy, 2009). ISRs are capable of measuring multiple parameters such as the electron density, electron and ion temperatures, the line-of-sight Doppler velocity, and more (Beynon & Williams, 1978). Modern ISRs operate in

multiple beams pointing in different directions and can measure plasma properties at multiple heights ranging from ~100 km to ~700 km (e.g., Bahcivan et al., 2010). The result of these measurements is a three-dimensional view of the plasma properties that can be analyzed over experiments that usually run up to several days.

### 2.1.1 Principles of ISR operation

The main idea used for the justification of the first ISR construction was that after sending very intense radio waves vertically into the ionosphere, the radar would be able to detect return signals from individual electrons through a process known as Thomson scatter of electromagnetic radiation (Beynon & Williams, 1978; Hunsucker, 1991; Schunk & Nagy, 2009; Sedgemore-Schulthess & St.-Maurice, 2001). J. J. Thomson in 1906 established that a single electron can scatter electromagnetic waves, and the radar cross section  $\sigma_e$  of a single scattering event is given by (Schunk & Nagy, 2009)

$$\sigma_e = 4\pi(r_e \sin\psi)^2 \quad (2.1)$$

where  $r_e$  is the classical radius of an electron ( $r_e = 2.818 \times 10^{-15}$  m) and  $\psi$  is the angle between the direction of the incident electric field and the direction of the observer. The term “incoherent scatter” originates from understanding that the electrons are involved in thermal fluctuations of the plasma with short coherence time (Sedgemore-Schulthess & St.-Maurice, 2001). If the electron density fluctuations in the plasma come from random thermal motions, the cross section for energy backscatter by a unit volume  $\sigma_v$  in the ionosphere is given by (Schunk & Nagy, 2009)

$$\sigma_v = N_e \sigma_e \quad (2.2)$$

where  $N_e$  is the electron density and  $\sigma_e$  is the radar cross section. Equation (2.2) implies that the intensity of a received ISR signal is proportional to the electron density, and this is an indication that the electron density can be inferred from the power of received echoes.

After the first ISR was built (Bowles, 1958), it turned out that the spectrum of the returned signal was more narrow than one would expect if the radio waves were scattered by free electrons (Hargreaves, 1992). The spectrum around zero Doppler shift was found to be on the order of several kHz, and it became clear that ions are also involved in the scattering process. It is now accepted that the main component of ISR detected signals comes from radio wave scattering by ion-acoustic plasma waves formed by joint electron and ion motions (Hargreaves, 1992; Schunk & Nagy, 2009; Sedgemore-Schulthess & St.-Maurice, 2001). ISRs can also detect much weaker

scatter from plasma waves at the electron plasma frequency and ion gyrofrequency, corresponding to plasma fluctuations governed exclusively by electron and ion motions, respectively (Hargreaves, 1992; Sedgemore-Schulthess & St.-Maurice, 2001). Although the presence of ions in the ionosphere introduces some degree of coherence in plasma fluctuations, the term “incoherent scatter” is still used to describe the return signal (Sedgemore-Schulthess & St.-Maurice, 2001).

ISRs operate by transmitting high-power (on the order of MWs) radio wave pulses into the ionosphere (Häggröm, 2017). Plasma scatters the signal at a given height, but the amount of scattered power is very small compared to the transmitted power, a reduction by a factor of  $\sim 10^{-19}$  (Häggröm, 2017). Large aperture receiving antennas, often the same device as the transmitter antennas, are used to detect the scattered signals. Besides having higher gain, the large aperture antennas provide a narrow beam allowing for a better spatial resolution of measurements. The beamwidth of ISR antenna is on the order of  $1^\circ$  (Beynon & Williams, 1978). A sketch of ISR geometry of observations at high latitudes with the beam oriented close to the Earth’s magnetic field lines is shown in Figure 2.1a.

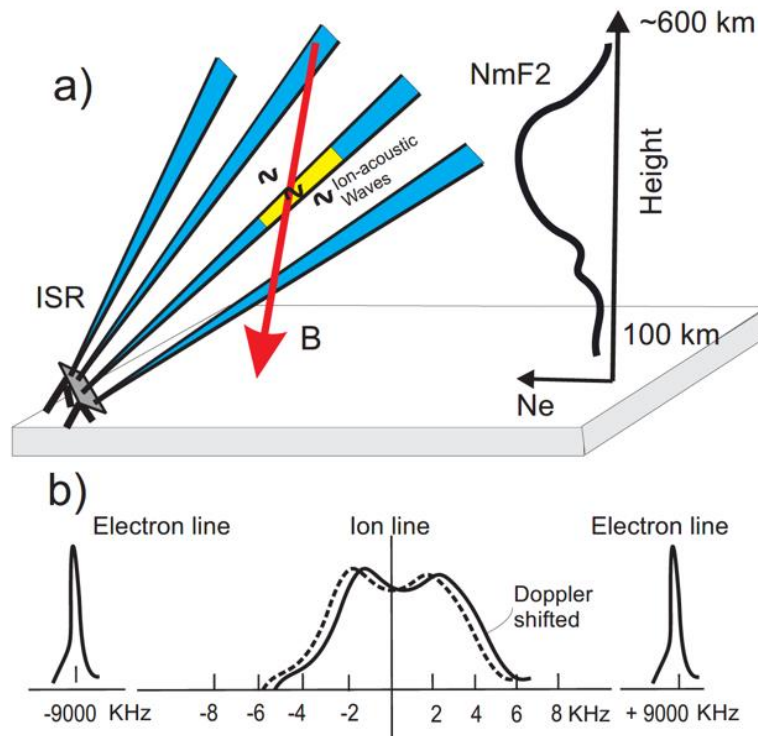


**Figure 2.1:** (a) A sketch illustration of ISR radar configuration for measurements at high latitudes. Insert on the right shows a generic electron density profile in the ionosphere for altitudes from 100 km to 600 km. (b) A sketch of the typical spectrum of a signal received by an ISR. The dashed line represents an ion spectrum without Doppler shift.

The pulse length of each transmission determines the range resolution of the measurements. A shorter pulse length will achieve a higher range resolution, at the cost of spectral resolution, and a longer pulse length will result in poorer range resolution with a better spectral resolution (Häggström, 2017). ISRs transmit specially designed pulse sequences consisting of five or more pulses with certain pulse separation. Each transmitted pulse is separated by a time delay equal to multiples of a base delay time,  $\tau$ . An image showing a two-pulse sequence is given in Figure 2.2.

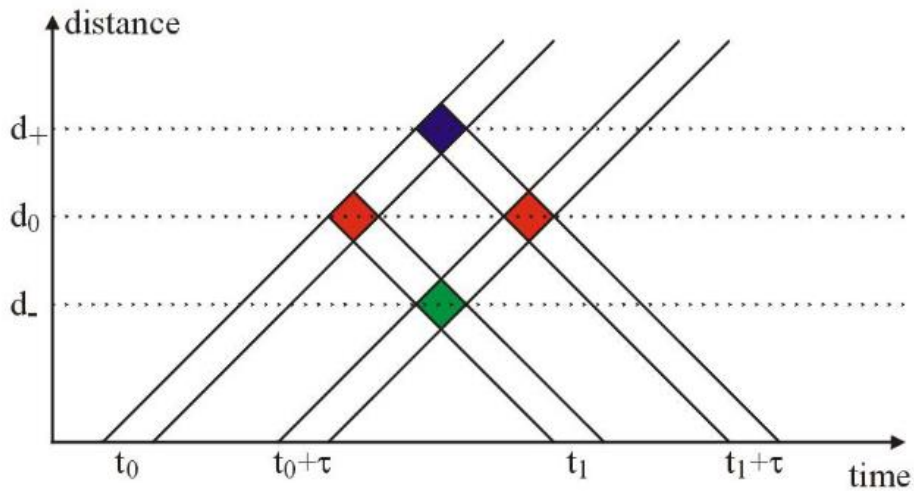


**Figure 2.2:** Sketch of a two-pulse sequence transmitted and received by an ISR system. Horizontally is time and vertically is the distance traveled by the transmitted and scattered signal. Image from McWilliams et al. (2003).

A pulse transmitted at time  $t_0$  will be scattered at multiple heights, for example  $d_0$  which will be received by the radar at time  $t_1$  and  $d_+$  which will be detected at time  $t_1 + \tau$ . Similarly, a pulse transmitted at time  $t_0 + \tau$  will be scattered at multiple heights and detected at multiple times. The return signal at a given time may be from two pulses separated by a time lag from two different heights. Multiple received pulses are placed into the time domain, and the autocorrelation function (ACF) of the pulses is evaluated for different time delays between the pulses. The average autocorrelation function at lag  $\tau$  for a two-pulse sequence (Figure 2.2) is given by (McWilliams et al., 2013)

$$\langle ACF(\tau) \rangle = \langle X_1(d_0) \cdot X_2(d_0) \rangle + \langle X_1(d_0) \cdot X_1(d_+) \rangle + \langle X_2(d_-) \cdot X_1(d_+) \rangle + \langle X_2(d_-) \cdot X_2(d_0) \rangle \quad (2.3)$$

where  $X$  is the amplitude from the received signal, and  $d_0$ ,  $d_-$ , and  $d_+$  are distances from the radar shown in Figure 2.2. A spectrum of the returned signals is obtained by taking the Fourier transform of the ACF. A sketch of a typical spectrum received by an ISR is shown in Figure 2.1b.

Figure 2.1b shows that the spectrum of the received signal has two main components: the wide ion line and the narrow electron lines. The electron lines are located at  $\pm f_p$  (the plasma frequency) which is related to the electron density by equation 1.6 given in Chapter 1. Unfortunately, the electron lines are typically too weak to be analyzed as they are well below the noise level of the returned signal, and the ion line is used to determine the electron density (Hargreaves, 1992).

The ion line consists of two “humps”, each separated from the base frequency by either a positive or negative frequency shift. The frequency shift is given by (Hargreaves, 1992)

$$F(\Lambda) = \frac{1}{\Lambda} \left[ \frac{k_B T_i}{m_i} \left( 1 + \frac{T_e}{T_i} \right) \right]^{1/2} \quad (2.4)$$

where  $\Lambda$  is half the radar wavelength,  $k_B$  is the Boltzmann constant,  $m_i$  is the ion mass, and  $T_i$  and  $T_e$  are the ion and electron temperatures, respectively. The radar detects waves moving toward the radar and moving away from it giving a two-hump shape of the ion line (Hargreaves, 1992).

The ion line can be used to measure not only electron density, but also the electron and ion temperatures, ion mass, and the velocity of plasma motion along the radar beam (Beynon & Williams, 1978). Hargreaves (1992) and Sedgemore-Schulthess & St.-Maurice (2001) give a description of how the plasma parameters are obtained from the spectrum of the received signal. The total area of the ion line spectrum represents the total receiver power, which is proportional to  $N_e/(1 + T_e/T_i)$ , where  $N_e$  is the electron density and  $T_e$  and  $T_i$  are the electron and ion temperatures, respectively. Thus, the total area under the ion line can be used to determine electron density. The location and height of the spectrum peaks are used to determine the electron and ion temperatures, and the ion mass. The height of each peak relative to the local minimum between them gives an indication of the electron-ion temperature ratio  $T_e/T_i$ , and the separation of the peaks is proportional to  $(k_B T_i/m_i)^{1/2}$ , where  $k_B$  is the Boltzmann constant,  $T_i$  is the ion temperature, and  $m_i$  is the ion mass. The frequency offset of the spectrum is used to determine the Doppler shift and thus the line-of-sight velocity of the ion-acoustic waves, which corresponds to the bulk plasma motion along the radar beam.

Although the total power received by the ISR is related to the electron density, the absolute values cannot be inferred from the ion line analysis, and the radar requires calibration. One method for calibrating the data is to use the peak frequency from the electron line to determine the absolute value of density. However, due to noise and the relatively weak electron line intensity, this method

is often unsuccessful. A more commonly used calibration method, and the method used to calibrate RISR-C data (e.g., Gillies et al., 2016), is to compare the data to a local ionosonde (Canadian Advanced Digital Ionosonde, CADI, for RISR-C). First, the electron density is determined from the spectrum using a place-holder scaling constant while the CADI ionosonde is run over the same time period. The peak densities are determined from the CADI ionograms for each time interval and compared to the peak densities of each RISR-C profile. At each time interval, a scaling factor is determined from the comparison for each individual beam.

A typical pulse length for an ISR is on the order of  $\sim 1$  ms (Gillies et al., 2016). When creating the spectrum, as sketched in Figure 2.1b, information on arrival time for multiple pulses is considered. By combining pulses, the noise caused by random radiation in the plasma scattering volume is reduced (Diaz et al., 2008). When more pulse sequences are considered (i.e., longer integration time is used), the resulting spectrum becomes less noisy.

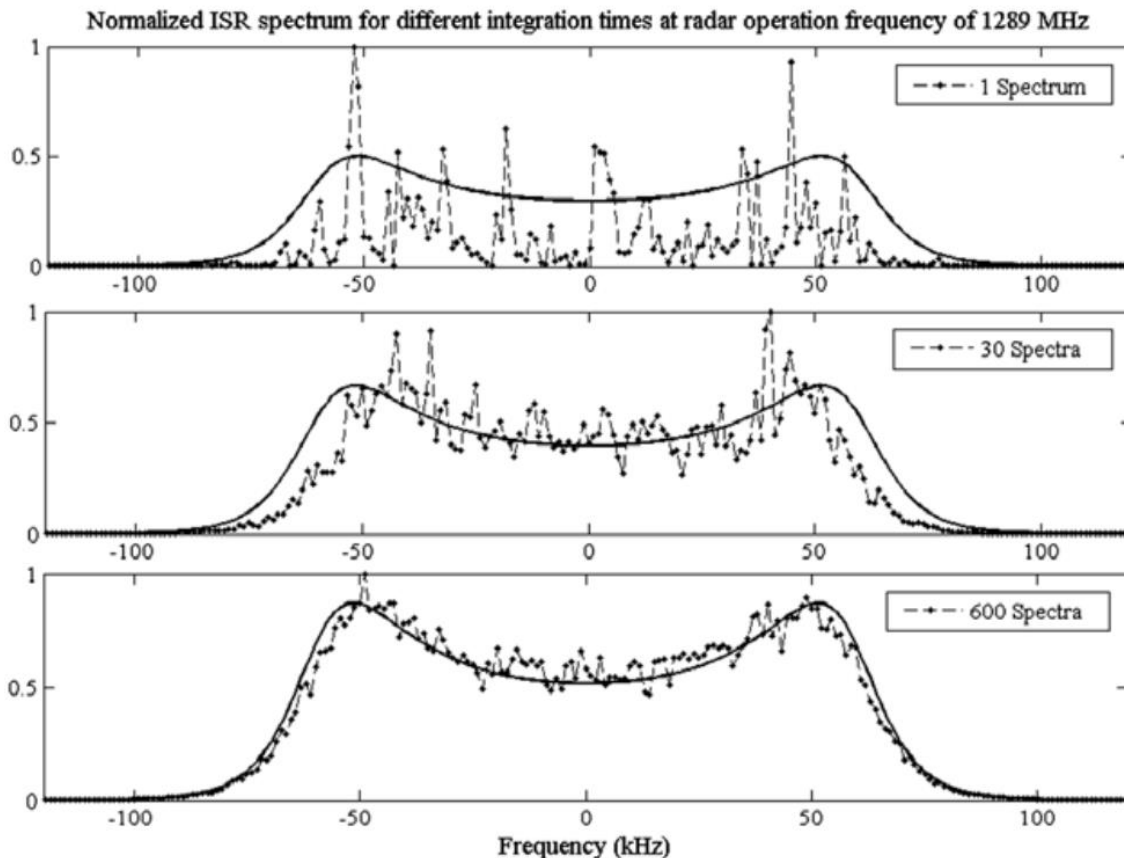


**Figure 2.3:** Simulated ISR spectra for 1, 30, and 600 independent computer runs illustrating the effect of integration time on the shape of the ion line. The solid line is the theoretical spectral line expected for the conditions of modeling. This is Figure 5 from Diaz et al. (2008).

Figure 2.3, from Diaz et al. (2008), illustrates how integration time affects the resulting spectrum by comparing simulated data with the theoretical spectrum expected for the modeling conditions. As seen in Figure 2.3, when only one pulse sequence (1 spectrum) is considered, the spectrum is very noisy, and the agreement with the theoretical spectrum is poor. For 30 pulse sequences, the resulting spectrum is still noisy but shows better agreement with the expected spectrum. 600 spectra show the best agreement with the theoretical spectrum. Diaz et al. (2008) considered a pulse width of 0.92 ms for the simulation, resulting in a total integration time of ~0.55 s for 600 spectra. This is still a relatively short integration time for ISR data, which is typically 1 min or greater (Gillies et al., 2016).

### 2.1.2 Advanced Modular ISRs and the Poker Flat ISR

The Advanced Modular Incoherent Scatter Radar (AMISR) is a special type of ISR instrument. AMISR systems use electronic beam steering to quickly reposition the beam in multiple directions. The PFISR radar is one of few AMISR designs in the world (Mathews et al., 2008). Typical AMISR systems have up to 10000 possible beam positions (Valentic et al., 2013). Each beam position has a different elevation and azimuth angle to cover a large three-dimensional area around the radar. Different modes of operation use different number of beams for a given AMISR system. AMISR systems use multiple transmitter/receiver elements called antenna element units (AEUs), each with a 500 W power amplifier and a cross-dipole antenna (Valentic et al., 2013). Each panel on an AMISR face includes 32 AEUs grouped together. An image of the face of an AMISR with individual AEUs is shown in Figure 2.4.

Each panel has a panel control unit which monitors the state of each AEU and records voltage, current, temperature, humidity, and measurements of the transmitted and received power (Valentic et al., 2013). A typical AMISR face contains 128 panels producing a peak transmission power of ~2 MW across the 4096 AEUs (Valentic et al., 2013). The AEUs used in AMISR systems can switch between transmitting and receiving mode in ~0.6  $\mu$ s, and AMISR systems can switch between beams over time on the order of 1 ms (Valentic et al., 2013).



**Figure 2.4:** Image of individual antenna element units (AEUs) on the face of the RISR-C radar. Image from Gillies & Varney (2016).

The geographic location of the PFISR radar is  $65.12^{\circ}$  N and  $-147.47^{\circ}$  E, near Fairbanks, Alaska. The magnetic local time at Fairbanks, Alaska is  $\sim 13$  h behind universal time (UT), meaning that magnetic midnight occurs around 11 UT. PFISR operates at a transmission frequency of 449.3 MHz with a typical transmission power of 0.5 MW (Mathews et al., 2008). PFISR electron density measurements are available in two data sets, which are alternating code and long pulse data. The alternating code mode uses short pulse lengths for a finer range resolution in the measurements and is typically used to measure the bottomside ionosphere (Mathews et al., 2008; Whittier, 2014). The alternating code pulse type has a range resolution of 4.5 km, and the long pulse type has a range resolution of 72 km (Whittier, 2014). This thesis will only consider data obtained from the long pulse type.

The major operating mode of PFISR is the International Polar Year (IPY) mode which began observations in March 2007 (Sojka et al., 2009). In this mode, PFISR uses only 4 beams pointed near the zenith of the radar. A plot showing the configuration of four beams from the

PFISR radar is shown in Figure 2.5. The radar measurements span  $\sim 4^\circ$  of magnetic latitude and  $\sim 13^\circ$  of magnetic longitude at their maximum range.

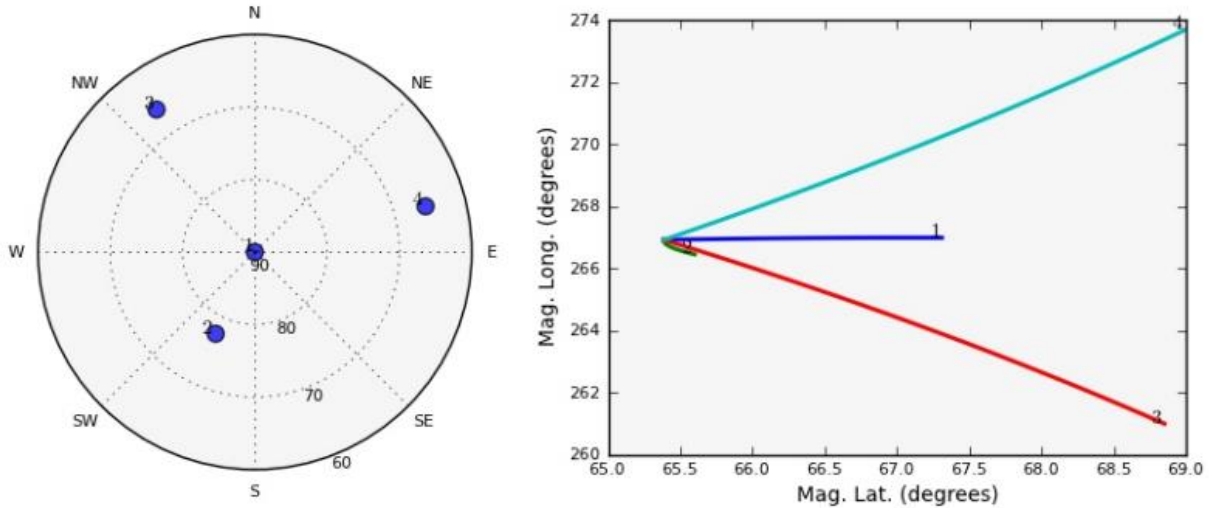


**Figure 2.5** PFISR beam geometry in International Polar Year (IPY) mode. The left plot shows the direction of each beam with the radar located at the center of the plot. Radially is elevation angle and tangentially is the azimuth angle of each beam. The right plot shows the magnetic coordinates covered over the entire range of each beam. Image from <https://isr.sri.com/madrigal>.

The objective of the IPY mode is to gain understanding of the polar terrestrial environment across the globe over long periods, and PFISR is operated in this mode for the majority of its available operation time (Sojka et al., 2009). For this reason, the dataset available is far greater than for other radars, such as RISR-C. PFISR data in IPY mode are available with both 1 min and 5 min integration times. A plot of electron density measurements from the PFISR radar is shown in Figure 2.6. Measurements from one of the 4 beams in IPY mode are shown in Figure 2.6, along with the azimuth and elevation angle the beam. For each beam, electron density is at a maximum around the F-region peak ( $\sim 250$  km) and at local noon ( $\sim 23$  UT). The electron density decays slowly as altitude increases above the peak, and decays quicker below the peak. For all altitudes, minimum electron density occurs around local midnight ( $\sim 11$  UT) and dusk.

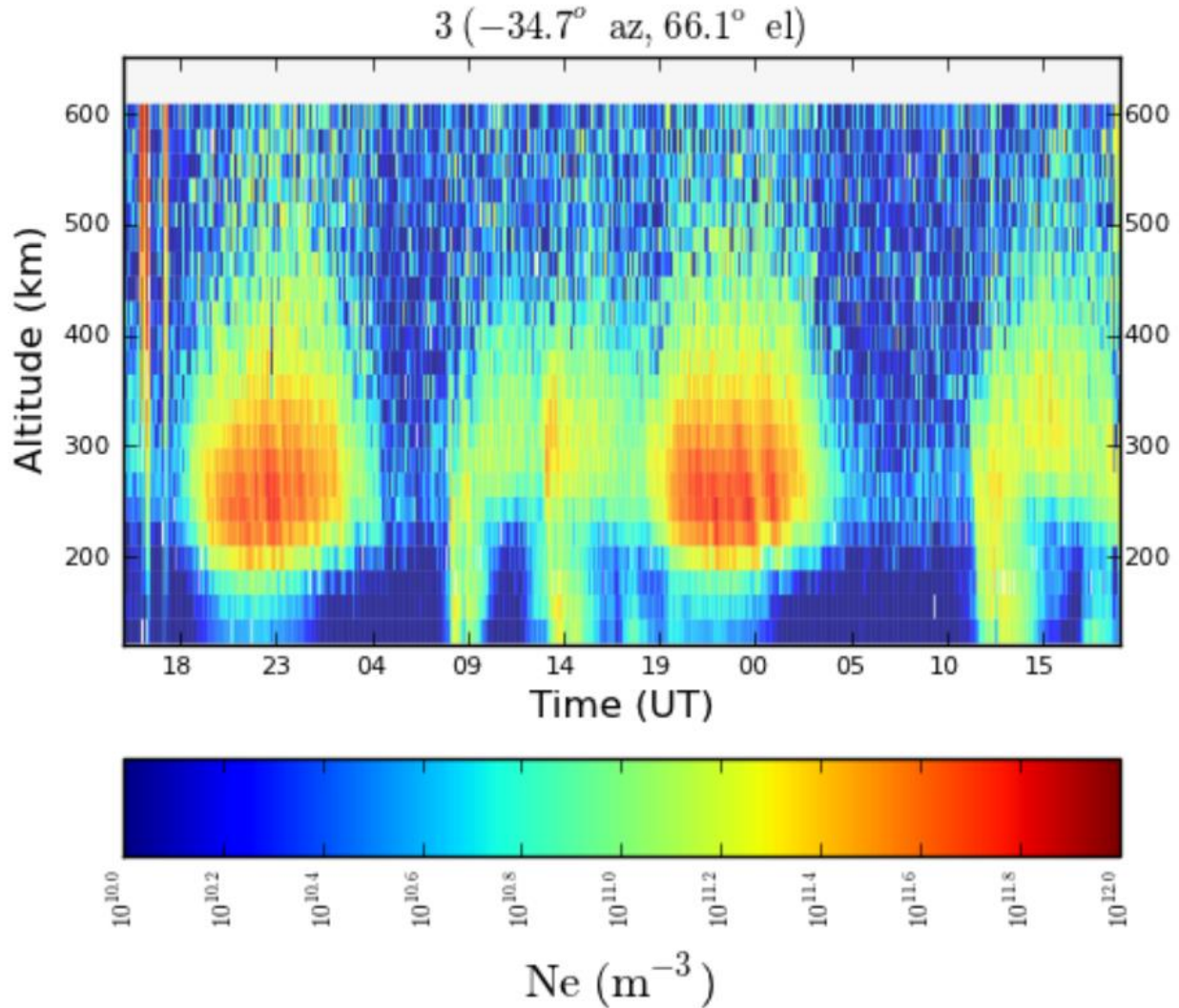


**Figure 2.6:** PFISR observations in the IPY mode from ~15 UT on 16 January, 2016 to ~19 UT on 18 January, 2016. Data shown are from one of the 4 beams in IPY. Azimuth and elevation angles for the given beam are shown at the top of the plot. On the horizontal axis is UT time in hours, and on the vertical axis is altitude in kilometers. Electron density is represented by the color bar at the bottom of the figure. Image from the SRI Madrigal Database: <https://isr.sri.com/madrigal>.

### 2.1.3 Resolute Bay ISR

Similar to the PFISR radar, RISR-C is also an AMISR type of a system. The geographic location of the RISR-C radar is  $74.70^\circ$  N and  $-94.83^\circ$  E, and all its beams are oriented equatorward of the radar (Gillies et al., 2016). The radar can take measurements of the ionosphere at latitudes as low as  $68^\circ$  N and for longitudes ranging from  $-105^\circ$  E to  $-75^\circ$  E (Gillies et al., 2016). The MLT at Resolute Bay is ~7 h behind UT. The operational frequencies of RISR-C range from 441.9 MHz

to 443.9 MHz (Gillies & Varney, 2016). The typical pulse width for RISR-C is  $\sim 0.33$  ms, corresponding to a range resolution of  $\sim 50$  km (Gillies et al., 2016). The transmitter/receiver system used by RISR-C has 121 panels, each containing 32 individual AEU's (Gillies & Varney, 2016). Commonly used operation modes of RISR-C are the World Day mode and Imaging mode, which use 11 beams and 51 beams, respectively. For this thesis, only data from the Imaging mode are considered. RISR-C imaging mode data are available with 1 min or 5 min integration times. The differences between data of the two integration times will be discussed in Section 2.2.

#### 2.1.4 Data sources

RISR-C data were downloaded from <https://madrigal.phys.ucalgary.ca>. PFISR data were downloaded from <https://isr.sri.com/madrigal/>. Calibrated electron density data were provided by both sources.

## 2.2 Comparison of 1-min and 5-min RISR electron density data in Imaging Mode

In Chapter 4 of this thesis, ISR and LP measurements from the Swarm satellites in the topside ionosphere will be compared with each other to further validate the LP instruments. Larson (2021) and Larson et al. (2021) performed a similar analysis using the RISR-N and RISR-C radars. While comparing the data at close locations, Larson (2021) and Larson et al. (2021) discovered that the disagreements between the ISR and Swarm measurements were visibly larger whenever 1-min resolution RISR data were selected for the comparison. For a shorter time resolution, one would expect a better agreement of Swarm and RISR data because of the closer time intervals of the measurements. One working hypothesis was that 1-min measurements are affected by signals from ionospheric plasma perturbations caused by satellites crossing a radar beam. It was also noticed that RISR 1-min resolution electron density profiles at times close to the satellite crossing are often unphysical, and the errors were likely caused by echo returns from the satellites themselves. These unphysical data were filtered out from the analysis automatically because of large error measurements provided in the data.

If the ionospheric plasma perturbations in the wake of a satellite are indeed strong, they should affect both 1-min and 5-min data, but the effect is expected to be stronger for 1-min data. This is because the standard ACF analysis of a returned signal in the RISR analysis is supposed to be over 72 s (Ashton Reimer of Stanford Research Institute, the headquarters of the RISR radars), but the data beyond 60 s of each 72 s run are truncated to achieve the 1-min resolution. The truncation effect is expected to be stronger for measurements at low electron densities, which is the case for RISR observations at the ionospheric topside.

This section investigates the quality of 1-min and 5-min RISR data by considering data at all heights, irrespective of whether the Swarm satellites were in the vicinity of radar beams. Initially, RISR-C World Day mode data were considered as a follow up to work performed by Larson. Later, the focus was shifted towards Imaging Mode data, as the entirety of this thesis work is focused on this type of data. Accordingly, observations in 51 beams of RISR-C were considered. For assessing 1-min and 5-min data, the data base included two experiments in March 2016, see Table 2.1.

For the comparison, the median value of five consecutive electron density profiles with 1-min resolution were taken at every height corresponding to the intervals of the 5-min resolution data. The pairs of data, median of 1-min resolution electron densities ( $N_e^{1min}$ ) and 5-min resolution electron densities ( $N_e^{5min}$ ), at the same height were plotted together. Figure 2.7 and Figure 2.8 present data for two heights of comparison, 300 km and 450 km, respectively. These heights were chosen since they represent the central part of the F2 region (300 km) and the height which the Swarm A and Swarm C satellites orbit (450 km). Data with relative error greater than 50% were not considered.

**Table 2.1** List of RISR-C experiments considered for the comparison of 1-min and 5-min data.

Start Day	UT for Start	End Day	UT for End
March 02	17:04	March 03	05:36
March 03	05:43	March 04	22:59

Figure 2.7a is a scatter plot of the 1-min and 5-min electron density values in bins of  $1 \times 10^{10} \text{ m}^{-3}$ . The majority of the data is located fairly close to the bisector of a perfect agreement,

shown by the darker color surrounding the line. Slightly larger values of  $N_e^{1min}$  are recognizable, at least at smallest and largest electron densities.

Figure 2.7b is a histogram distribution for the difference,  $D_{300km} = (N_e^{5min} - N_e^{1min})/N_e^{5min}$ , expressed in percent. The distribution is asymmetric with a tail towards negative values of  $D_{300km}$ . However, the number of points within the tail is visibly not large, and the majority of the points are near the center of the distribution. The median value of the distribution,  $\mu$ , is -4% and the standard deviation of the distribution,  $\sigma$ , is 23% indicating that, typically, the 1-min and 5-min values are in reasonable agreement.

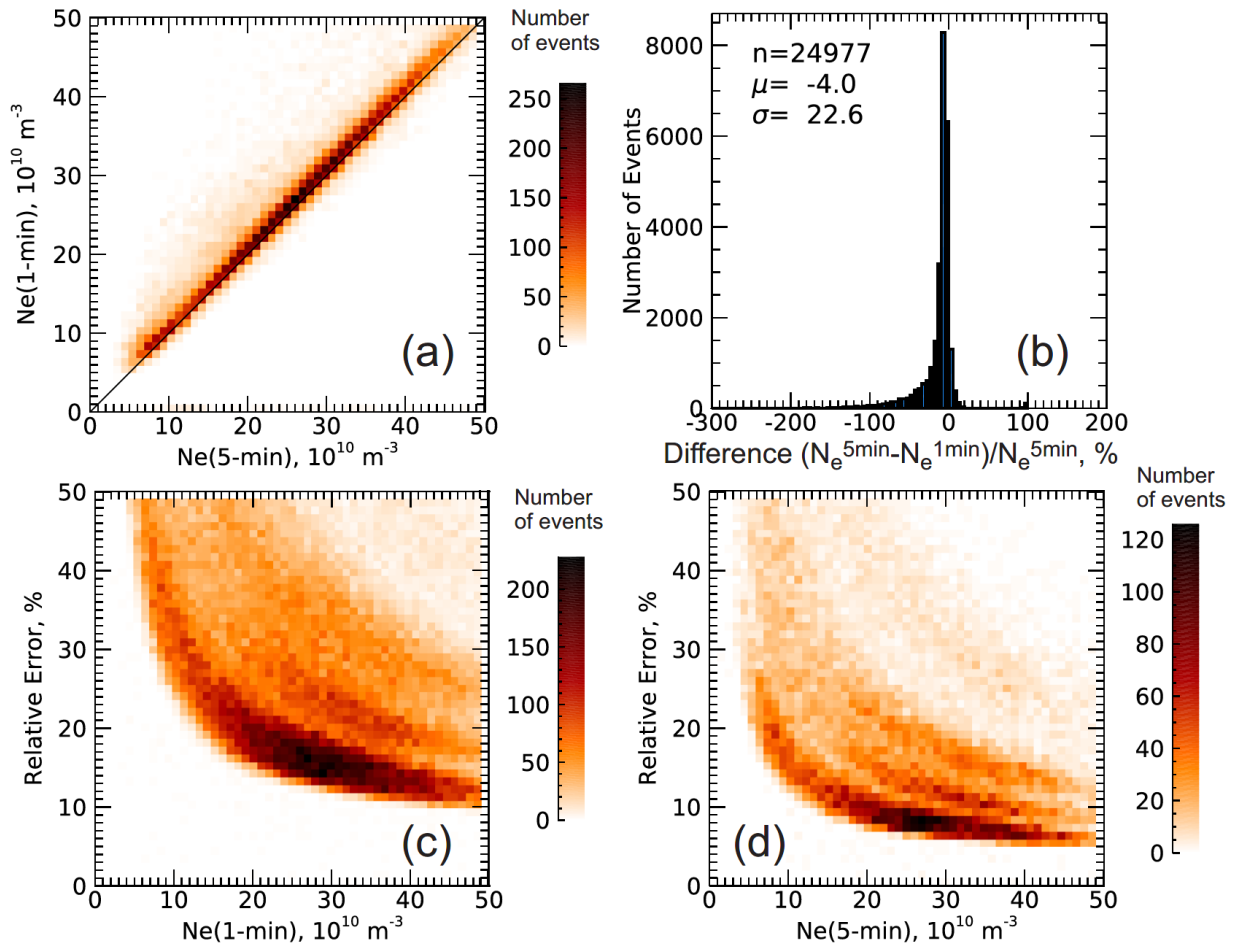


**Figure 2.7:** Electron density ( $N_e$ ) data collected by the RISR-C radar at the height of 300 km for multiple events in March 2016 (Table 2.1) in the Imaging Mode of operation (51 beams). (a) Scatter plot of  $N_e$  with 1-min resolution versus  $N_e$  with 5-min resolution. Shown also is the bisector of perfect agreement, the thin black line. (b) Histogram of the relative difference,  $(N_e^{5min} - N_e^{1min})/N_e^{5min}$ , expressed in percent. Shown also are the total number of points,  $n$ , median of the distribution,  $\mu$ , and the standard deviation for the distribution,  $\sigma$ . (c) Scatter plot of the relative error in  $N_e$  measurements (in percent) for the  $N_e^{1min}$  data. (d) the same as (c) but for the  $N_e^{5min}$  data.

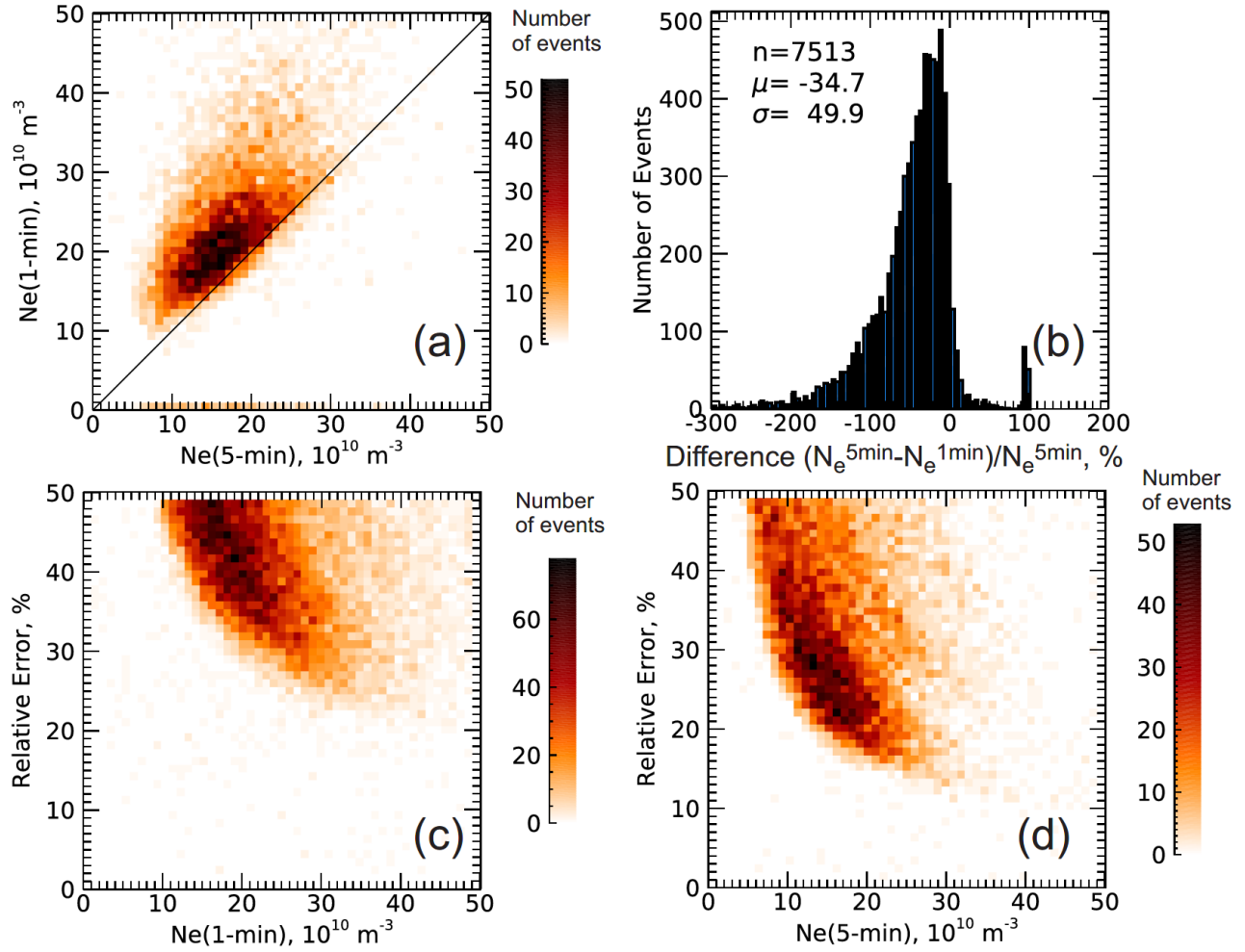
Figures 2.7c and 2.7d give a sense of errors (relative values) for measurements with 1-min and 5-min resolutions. The 1-min measurement errors are all above 10% and some of them can be as large as 50%. A significant portion of the points are clustered between 15% and 20%. The 5-min errors are visibly smaller, with the clustering of data points between 5% and 15%. Larger measurement errors for 1-min data are expected because of the much smaller radar signal integration time. Both Figure 2.7c and Figure 2.7d show a gradual decrease of relative errors toward larger electron densities, in both  $N_e^{1min}$  and  $N_e^{5min}$ , indicating that larger electron densities reported by RISR are more reliable, independent of the collection time.

Figure 2.8 presents data for a height of 450 km, the ionospheric topside, in the same format as Figure 2.7. Figure 2.8a, a scatter plot of the 1-min and 5-min electron density values in bins of  $1 \times 10^{10} \text{ m}^{-3}$  at a height of 450 km, shows a round cloud of points above the bisector of perfect agreement. Thus,  $N_e^{1min}$  values are typically larger than  $N_e^{5min}$  values in the topside ionosphere at ~450 km.

Figure 2.8b is a histogram distribution for the difference  $D_{450km}$ . The distribution is asymmetric and much wider compared to the distribution at 300 km, with  $D_{450km}$  values ranging from +100% to -300%. The median and standard deviation of the distribution are  $\mu = -34.7\%$  and  $\sigma = 49.9\%$ . Both values are much greater than the values of the distribution at a height of 300 km, showing that the difference between 1-min and 5-min RISR measurements is much greater at the topside ionosphere compared to the center of the F2 region.

One can conclude that, overall, the  $N_e^{1min}$  values are larger than  $N_e^{5min}$  values. To quantify the differences, the percentage of the averaged 1-min data points that were within a factor of 2 times greater or smaller than the 5-min RISR values was computed. At 300 km, 97.8% of points satisfied this criterion while at 450 km it was only 85.5%.

In terms of error of measurements, Figures 2.8c and 2.8d show that the 1-min errors are larger than the 5-min errors. The majority of the points in Figures 2.8c and 2.8d are clustered between 30% and 50% for 1-min data and between 15% and 40% for 5-min data, judging only by the darkest pixels on each plot.



**Figure 2.8:** The same as Figure 2.7 but for the height of 450 km.

To assess the height variation of the differences between 1-min and 5-min data, histogram distributions similar to those of Figure 2.7b and 2.8b were produced for every height above 300 km with a step of 20 km. The median and standard deviation of the obtained distributions were computed and are plotted in Figure 2.9.

Figure 2.9 shows that the median of the absolute difference between the data and the distribution width, represented by the standard deviation,  $\sigma$ , both increase with height. The median values are larger than 50% at heights greater than 490 km, where the relative error of the 5-min RISR data is typically less than 40%. For these heights, the width of the distribution is also greater than 50%. One can judge that the discrepancies between 1-min and 5-min electron density RISR measurements at heights above 500 km are strong, and these require further investigation.

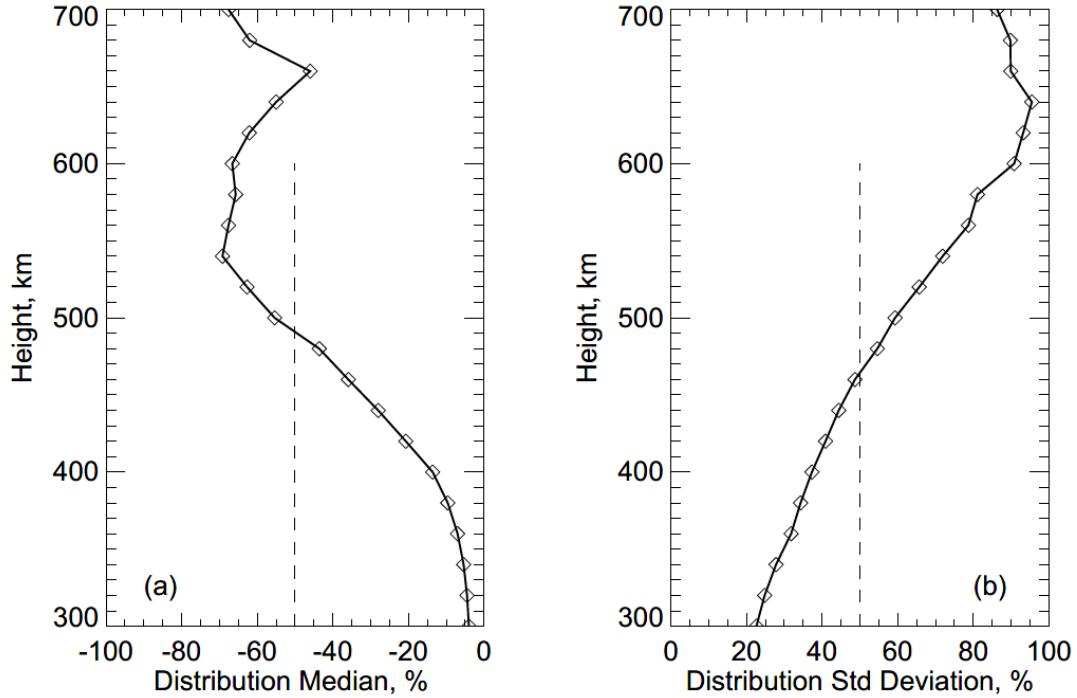


**Figure 2.9:** Variation with height of (a) the histogram distribution median,  $\mu$ , and (b) standard deviation,  $\sigma$ , for the quantity  $(N_e^{5min} - N_e^{1min})/N_e^{5min}$  expressed in percent.

To the best of my knowledge, the discrepancies between 1-min and 5-min RISR-C topside data have not been reported in the past and the reasons for the discrepancies are not known. One explanation is that perhaps the RISR-C data at low returned signals do not correctly describe the total energy of the signal whenever truncated ACFs are considered. This issue is beyond the scope of the present thesis and is a task for RISR engineers and researchers who have the capabilities to perform ACF analysis of specific events with various integration time. Also, over the years, special experiments optimized for studying the topside ionosphere have been run. Studying these data in detail would be useful to understand the differences in the data. Because of the inconsistencies between the 1-min and 5-min RISR data, this thesis considers only 5-min electron density measurements, corresponding to larger signal integration time, similar to the decision made by Larson (2021) and Larson et al. (2021).

## 2.3 Langmuir probe instruments in space

The Langmuir probe is an instrument used to measure electron density and electron temperature in a plasma (Chen, 2003; Bhattarai & Mishra, 2017; Schunk & Nagy, 2009). The probe is a

cylindrical, spherical, or planar electrode that is placed in an ionized gas or plasma. The probe is operated by applying a varying bias voltage and measuring the current flowing through the probe. The resulting current-voltage (I-V) curve is then analyzed to obtain the plasma characteristics (Chen, 2003; Schunk & Nagy, 2009).

Although LP instruments attached to satellites have been used in space measurements for many decades (Schunk & Nagy, 2009), there are still challenges in analyzing and interpreting the I-V curves. The ambient plasma in the ionosphere has multiple components and the plasma particles interact with both the LP instrument and the satellite. One of the results of the interaction between the satellite and the plasma is the formation of plasma perturbations in the wake of the fast-moving satellite. A recent trend in LP technology is the development of directional LP instruments (e.g., Samaniego et al., 2020), but traditional LP instruments, similar to those used in laboratory plasmas, are still widely used (Schunk & Nagy, 2009).

### 2.3.1 Classical Langmuir probes

Initially probes called “sounding electrodes” were used to measure the voltage distribution in gas discharges. A gas discharge was produced in a tube by applying a high voltage between two electrodes at the ends of the tube. It was initially assumed that the plasma potential,  $V_p$ , could be determined by measuring the potential of a probe placed in the plasma relative to one of the electrodes. However, it turned out that this procedure measures the floating potential,  $V_f$ , which is usually negative relative to  $V_p$ .

A conducting probe that is electrically disconnected from external bodies does not collect current from the plasma, so the potential of the probe becomes negative relative to the plasma to maintain zero net current (Chen, 2003; Merlino, 2007). After a probe placed into a plasma, initially it will draw a higher electron flux (current) because the electrons reach the probe faster than positive ions. Electrons reach the probe first because they have a higher thermal speed than ions by a factor of  $\sqrt{m_i/m_e}$ , since the electron mass  $m_e$  is less than the ion mass  $m_i$ . The accumulation of electrons on the probe will create a negative electric potential relative to the plasma which will increase the positive ion current to the probe and reduce the electron current until there is an equilibrium, and the net current is zero (Merlino, 2007). These processes result in the development of a sheath, or cloud, of positive ions around the probe, an effect known from the pioneering work

by Langmuir and Mott-Smith (1926). The thickness of the sheath can be estimated as  $\sim 5-10$  electron Debye lengths.

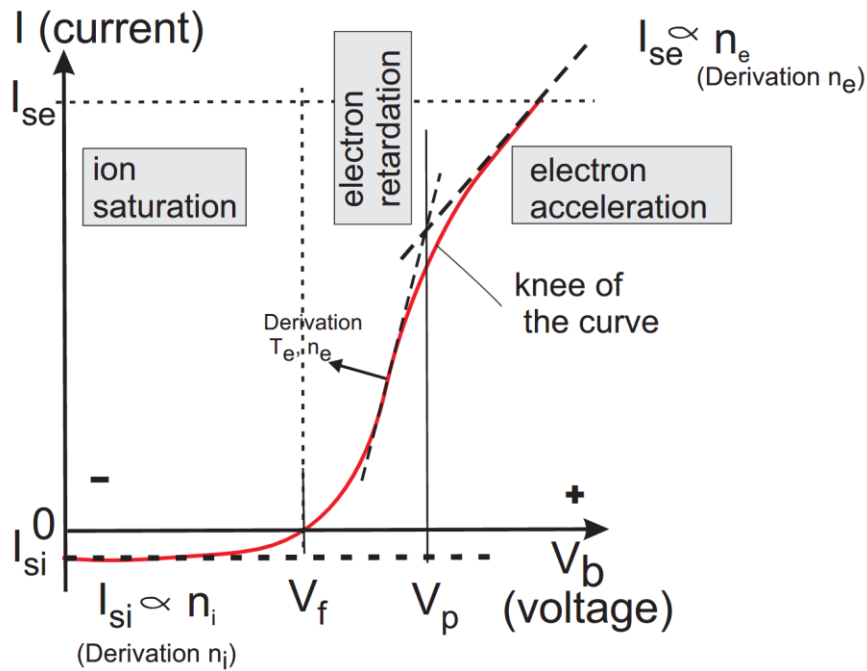


**Figure 2.10:** Langmuir probe current as a function of bias voltage. The ion saturation, electron retardation, and electron acceleration regions are indicated. Electron temperature can be measured at the point indicated by  $T_e$ . Adapted from Schunk & Nagy (2009). The sketch is a courtesy of A.V. Koustov.

Because of the difference between the plasma potential  $V_p$  and the floating potential  $V_f$ , an unbiased electrode placed in a plasma does not represent  $V_p$ , and the characteristics of the plasma cannot be determined. However, Irving Langmuir and Harold Mott-Smith (1926) proposed a method for determining  $V_p$  by applying a bias voltage,  $V_b$ , that is swept through a range of values, from negative to positive, and analyzing the obtained I-V curve. A sketch of a typical I-V curve obtained for an entire sweep of  $V_b$ , from strongly negative to strongly positive values, is shown in Figure 2.10. The analysis of the I-V curve allows one to infer, additionally, the electron density and electron temperature in the plasma which is of a great importance for plasma diagnostics (Chen, 2003; Schunk & Nagy, 2009).

Figure 2.11 illustrates what happens when a strongly negative biasing voltage is applied to a probe in a plasma. In this case, electrons are repelled from the vicinity of the probe while positive ions are pushed towards its surface which provides a positive current that can be measured by an independent instrument. This domain of applied voltages on the I-V curve is known as the ion

saturation region (e.g., Chen, 2003; Schunk & Nagy, 2009), the region on the left side of the diagram in Figure 2.10.

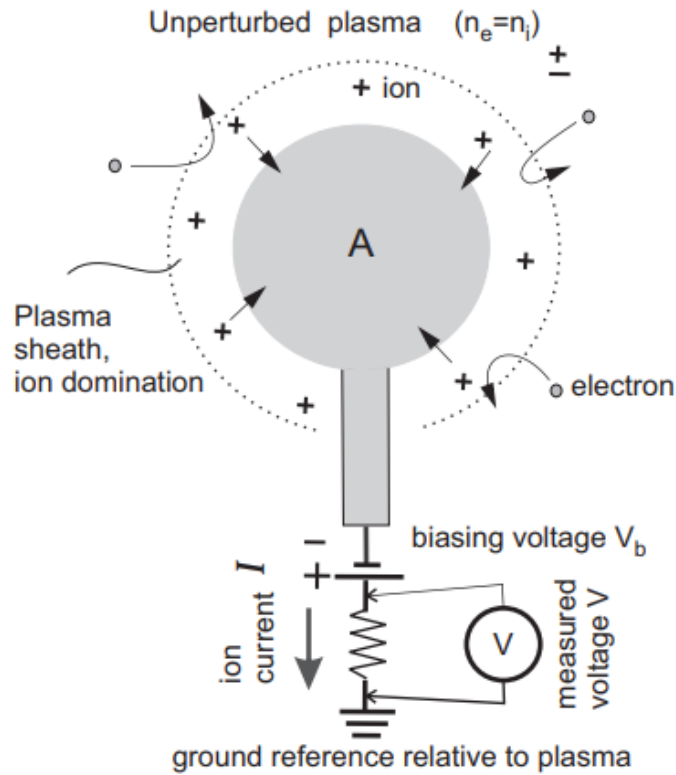


**Figure 2.11:** A schematic illustrating ion-driven current excitation in a negatively biased Langmuir probe.

When a probe is positively biased with a high voltage, the positive ions are repelled while electrons are attracted to the probe which provides a negative current through the probe. This domain of applied voltages on the I-V curve is referred to as the electron saturation or electron acceleration/accelerating region (e.g., Chen, 2003; Schunk & Nagy, 2009), the region on the right side of the diagram in Figure 2.10.

When the bias voltage of the probe is near the plasma potential, both ion and electron currents coexist and are collected by the probe, although the electron current dominates in the region because of the electrons' higher mobility. This domain of applied voltages on the I-V curve is referred to as the transition or electron retardation/retarding region (e.g., Chen, 2003; Schunk & Nagy, 2009), the central region in Figure 2.10. One comment with respect to the I-V curve in

Figure 2.10 is that, traditionally, the ion current is denoted as negative in the analysis despite the current being positive (Chen, 2003; Damba, 2020).

For the analysis of the I-V curve, two different approaches are used: orbital motion limited (OML) theory and sheath area limited (SAL) theory (e.g., Bhattarai & Mishra, 2017; Quinn, 2019; Resendiz Lira & Marchand, 2021). The OML theory requires that the radius of the probe is much smaller than the thickness of the plasma sheath. The SAL theory considers the case where the probe radius is comparable to or larger than the sheath thickness.

For ionospheric measurements, the OML theory is usually applied even though the probe is not significantly smaller than the thickness of the sheath (Bhattarai and Mishra, 2017; Schunk & Nagy, 2009; Quinn, 2019). Other simplifying assumptions of the OML theory, but not obviously satisfied, are that particles follow the Maxwellian distribution, the plasma is isotropic, and no magnetic field is present. However, with the presence of a magnetic field the probe current is reduced, as shown by Dote et al. (1965).

According to the OML theory, the probe draws electron and ion currents, each of which has a fixed saturation component  $I_{is}$  and  $I_{es}$  (corresponding to the ion and electron saturation regions, Figure 2.10) and an exponentially decaying component more relevant to the transition region (e.g., Merlino, 2007). The saturated current  $I_{\alpha s}$  for the dominant species is given by (Merlino, 2007)

$$I_{\alpha s} = \frac{1}{4} e N_{\alpha} v_{\alpha, th} A \quad (2.5)$$

where  $\alpha$  is either  $e$  for electrons or  $i$  for ions,  $N_{\alpha}$  is the density of the species,  $v_{\alpha, th}$  is the thermal velocity of the species, and  $A$  is the surface area of the probe. The thermal velocity is given by

$$v_{\alpha, th} = \sqrt{\frac{2k_B T_{\alpha}}{m_{\alpha}}} \quad (2.6)$$

where  $k_B$  is the Boltzmann constant,  $T_{\alpha}$  is the temperature of the species, and  $m_{\alpha}$  is the mass of the species. The presence of the  $v_{\alpha, th}$  term indicates that the currents are dependent on thermal effects in the ionosphere. The decaying current component  $I_{\alpha}$  for a given species when the current is not saturated is given by

$$I_{\alpha} = \pm I_{\alpha s} \exp\left[\mp e(V_p - V_b)/k_B T_{\alpha}\right] \quad (2.7)$$

where  $I_{\alpha s}$  is the saturated current of the species,  $e$  is the electron charge,  $V_p$  is the plasma potential,  $V_b$  is the bias voltage,  $k_B$  is the Boltzmann constant, and  $T_{\alpha}$  is the temperature of the species. In

equation 2.7, electron current is given by the top sign convection and ion current is given by the bottom sign convention. The total current,  $I$ , in any of the three regions is a combination of both the ion current,  $I_i$ , and electron current,  $I_e$  and is given by

$$I = \begin{cases} -I_{is} + I_{es} \exp[-e(V_p - V_b)/k_B T_e], & V_b < V_p \\ -I_{is} \exp[e(V_p - V_b)/k_B T_i] + I_{es}, & V_b > V_p \end{cases} \quad (2.8)$$

where  $e$  is the electron charge,  $V_p$  is the plasma potential,  $V_b$  is the bias voltage,  $k_B$  is the Boltzmann constant,  $T_\alpha$  is the temperature of the species, and  $I_{\alpha s}$  is the saturated current of the species, where  $\alpha$  is either  $e$  to denote electrons or  $i$  to denote ions.

When the bias voltage  $V_b$  is much less than the plasma potential  $V_p$  (in the ion saturation region), the exponential term of the electron current will go to zero, and the remaining current will be the ion saturation current. Similarly, in the electron accelerating region, where  $V_b$  is much greater than  $V_p$ , the exponential term from the ion current will go to zero and the remaining current will be from the electron saturation current. The electron saturation current is greater than the ion saturation current by a factor of approximately  $\sqrt{m_i/m_e}$ , which is  $\sim 170$  in the ionospheric F region where  $O^+$  ions dominate (assuming  $T_e \simeq T_i$  and  $N_e \simeq N_i$ ). This means that the ion saturation current magnitude sketched in Figure 2.10 is much smaller than how it is depicted in the diagram, and that electron current will dominate in the transition region. It is also important to note that with an increase of magnitude of the biasing voltage, the sheath thickness increases resulting in a minor increase of the saturation current, such that the slope of the I-V curve can be non-zero in the saturation regions (Merlino 2007). Another important caveat of the OML theory is that, if  $T_e \gg T_i$ , (which is not always the case in ionospheric F region), the ion saturation current  $I_{is}$  is controlled by the Bohm current, not a thermal current as in equation 2.5, and is given by (e.g., Merlino, 2007)

$$I_{is} = 0.6eN_i \sqrt{\frac{k_B T_e}{m_i}} A \quad (2.9)$$

where  $N_i$  is the ion density,  $k_B$  is the Boltzmann constant,  $T_e$  is the electron temperature,  $m_i$  is the ion mass, and  $A$  is the area of the probe.

To infer the electron density, current collected in the electron acceleration region is usually considered (e.g., Schunk & Nagy, 2009) by applying equations 2.5 and 2.8. To determine the electron density in this way, the electron temperature must be known. To determine  $T_e$ , the I-V curve in the electron retardation region is analyzed by considering a plot of the derivative of the

natural logarithm of the electron current  $I_e$  versus the bias voltage  $V_b$  (Schunk & Nagy, 2009). According to equation 2.7, the derivative is

$$d_e = \frac{d(\ln(I_e))}{dV_b} = \frac{e}{k_B T_e} \quad (2.10)$$

where  $e$  is the electron charge,  $k_B$  is the Boltzmann constant, and  $T_e$  is the electron temperature. From equation 2.10,  $d_e$  and  $1/T_e$  are related linearly. Fitting a curve to the data will allow for  $T_e$  to be determined. This method does not account for the presence of ion current (which is small compared to the electron current) or other currents produced by various processes, for example the production of photoelectrons (Schunk & Nagy, 2009). The electron temperature  $T_e$  can also be inferred from the electron retarding portion of the I-V curve using the more sophisticated Druyvestyn-type analysis (Schunk & Nagy, 2009).

The plasma potential  $V_p$  is found at the “knee” of the I-V curve (Bhattarai & Mishra, 2017; Damba, 2020), by finding the voltage corresponding to the intersection of the linear lines characterizing the electron saturation region and the electron retardation region of the I-V curve, see Figure 2.10.

### 2.3.2 Specific features of the Swarm LPs

Swarm A, B, and C are three ESA satellites with near polar orbits launched to study the near Earth’s electrodynamic environment (Buchert et al., 2015; Friis-Christensen et al., 2008; Knudsen et al., 2017). After the initial stage of the mission (lasting several months beginning in December 2013), Swarm A and Swarm C were set to fly side-by-side with a separation in longitude of  $\sim 1.4^\circ$  (near the equator) and  $\sim 10$  s in time, at an initial altitude of 460 km. Swarm B was set to fly in a different meridional plane, significantly shifted from two other satellites and at a higher initial altitude of 510 km.

Each Swarm satellite is equipped with two LPs. They are solid titanium spheres with a radius of 4 mm mounted on 8 cm long posts (Knudsen et al., 2017). Each probe can be operated with either high or low gain. The term gain is used to describe the probe’s sensitivity to the drawn current. The high gain (HG) probe is used to measure lower probe current, and therefore lower electron densities, and the low gain (LG) probe is used to measure higher probe current, and thus higher electron densities. The sensitivity ratio between the HG and LG units is  $\sim 50$  (Catapano et al., 2022). The two probes on each satellite each have a separate surface coating/plating. One has

a titanium nitride (TiN) surface and the other has a gold-plated (Au) surface. The TiN probe operated as the HG probe from December 2013 until 14 December 2018, when it was switched to operate as the LG probe (Quinn, 2019). The Au probe operated as the LG probe from December 2013 until 14 December 2018 before switching to the HG probe. The Au surface was introduced in the later stages of the instrument construction (Quinn, 2019) since it was expected that a layer of oxidation on the TiN surface would affect the performance of the probe in high density plasma, as evident in previous ESA experiments (Knudsen et al., 2017). Each probe has a sample rate of 2 Hz at which the measured plasma parameters, such as the electron density and electron temperature, are produced (Catapano et al., 2022; Knudsen et al., 2019). The electron density can also be estimated from the current through the face plate of each satellite, at a rate of 16 Hz (Catapano et al., 2002; Xiong et al., 2022), but analysis of the face plate data has only recently began (e.g., Xiong et al., 2022).

The technique and procedure in which the plasma parameters are routinely obtained from Swarm measurements differs from a traditional voltage sweep mode (SM) technique, described in Section 2.3.1, although the SM data are also available upon request. The Swarm LPs alternate between two sub-modes: the classic SM (voltage sweep between +5 V and -5 V), and a Harmonic Mode (HM) which was introduced for the first time for measurements in space via a satellite as part of the Swarm mission (Quinn, 2019). The SM is operated for 1 s in a 128 s cycle while the HM is operated for the remaining time. Thus, most of the collected data are from the HM measurements. In HM, the bias voltage is cycled between three bias points in which measurements are performed, shown in Figure 2.12 (sketched from the diagrams in Knudsen et al. (2017) and Quinn (2019)). An important statement was made by the LP Principal Investigator, Dr. S. Buchert, regarding the SM and HM measurements (Buchert, 2021): “sweep results turned out to be systematically different from harmonic mode results, the difference pattern is not yet understood.” This conclusion is a very strong argument for the need of comprehensive work in the validation of the Swarm LP measurements, both for SM and HM data, which is the subject of Chapter 4 of this thesis.

The three bias points are selected to be in the ion saturation region (point 1), the electron retarding/transition region (point 2), and the linear electron acceleration region (point 3) of the I-V curve (Buchert, 2019; Quinn, 2019). As described in Knudsen et al. (2017) and Quinn (2019), to identify the voltage of each point, the bias is shifted through a range of voltages between +2.8 V

and -1.5 V in 256 steps until there is no current flowing through the probe. This allows for the measurement of the floating potential and a confident estimate of the bias voltage required for the LP to be in the ion saturation region of the I-V curve (point 1). Measurements at points 2 and 3 are used to determine the electron temperature and spacecraft potential. Since electron density is the only type of data from the LP instruments considered in this thesis, the derivation of the electron temperature and spacecraft potential will not be discussed here. A detailed description and respective equations for these values can be found in Knudsen et al. (2017) and Quinn (2019).

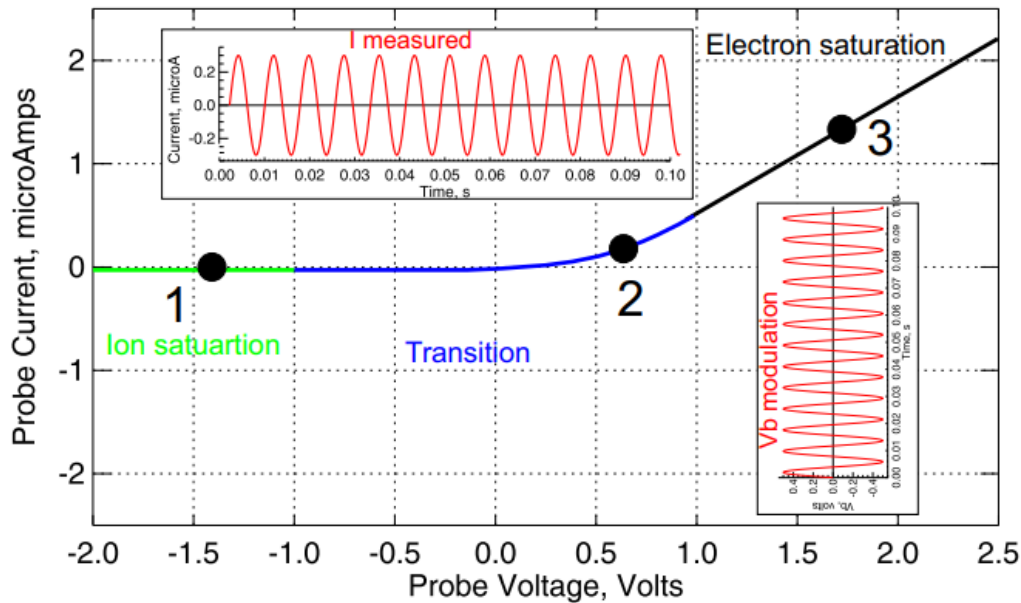


**Figure 2.12:** A schematic illustration of the Swarm measurement technique in harmonic mode. The plot was sketched from Figure 7 of Knudsen et al. (2017) and Figure 2.6 of Quinn (2019). Courtesy of A.V. Koustov.

At each of the biasing points, the voltage is modulated sinusoidally at frequencies up to 4 kHz with a nominal value of 128 Hz and with adjustable amplitude (Knudsen et al., 2017). Accordingly, the measured current is also sinusoidal, shown in Figure 2.12. Each modulation lasts for ~0.1 s. The harmonic modulation at each bias point allows for both the current and the admittance, which is the derivative of the current with respect to the bias voltage, to be obtained. The real part of the admittance is the derivative of the I-V characteristics, and the capacitance (imaginary part) is expected to be small and can be used to detect external natural or instrumental disturbances (Knudsen et al., 2017).

For the plasma density derivation, measurements in the ion saturation portion of the I-V curve (point 1 in Figure 2.12) are considered. Analysis of the data shows that the ion saturation region (point 1) is much less disturbed than the electron regions, so the electron density is calculated using the measurements from point 1 instead of point 3 as expected from the classical LP approach and equation 2.8. For this reason, Swarm researchers often refer to the obtained plasma density as the ion density ( $N_i$ ) (e.g., Xiong et al., 2022). However, for plasma the ion density is the same as the electron density with a high degree of agreement.

For a LP attached to a satellite, the ion ram energy which is dependent on the speed of the ions relative to the satellite is much greater than the thermal energy of the ions. The ion ram energy is  $\sim 4.7$  eV and the thermal energy of  $O^+$  ions is only  $\sim 0.17$  eV. For a satellite orbiting in the ionosphere, the speed of the ions relative to the satellite is roughly equal to the speed of the satellite ( $\sim 7.5$  km/s for Swarm). The ion ram energy replaces the thermal energy in the expression for the ion saturation current  $I_{is}$  and equation 2.5 is modified to (Knudsen et al., 2017)

$$I_{is} = -\pi r_p^2 e u_i N_i (1 - e(V_b + V_s)/E_i) \quad (2.11)$$

where  $e$  is the electron charge,  $N_i$  is the ion density,  $V_b$  is the bias voltage,  $V_s$  is the spacecraft potential,  $r_p$  is the radius of the probe,  $u_i$  is the speed of the satellite, and  $E_i$  is the ion ram energy given by  $E_i = \frac{m_i u_i^2}{2}$ , where  $m_i$  is the ion mass. The ion density can be determined from the derivative of the current with respect to the applied bias voltage from equation 2.11. Solving for the ion density  $N_i$  gives

$$N_i = \frac{dI_{is}}{dV_b} \cdot \frac{m_i u_i}{2\pi e^2 r_p^2} \quad (2.12)$$

where  $I_{is}$  is the ion saturation current,  $V_b$  is the bias voltage,  $m_i$  is the ion mass,  $u_i$  is the speed of the satellite,  $e$  is the electron charge, and  $r_p$  is the radius of the probe.

### 2.3.3 Data Source

The Swarm data used in this thesis are classified as “level1b”, calibrated electron density readings at 2 Hz provided by the European Space Agency. Only data obtained from the high gain probe, which is more sensitive to electron density fluctuations (Quinn, 2019), were used in this thesis. The data were downloaded from [swarm-diss.eo.esa.int](http://swarm-diss.eo.esa.int).

## 2.4 Summary

This chapter introduced the major two instruments used to collect the electron density data that are presented in this thesis. ISR systems collect electron density data by transmitting pulses into the ionosphere and analyzing the spectrum from the backscattered pulses. PFISR and RISR-C are the two ISR instruments selected for this thesis. LPs operate by applying a variable bias voltage and measuring the collected current from either electron or ions, or both. Electron density is determined from the resulting I-V curves. Electron density data from the LPs on the Swarm A, B, and C satellites are presented and analyzed in Chapter 4 of this thesis.

# Chapter 3

## Electron density over Poker Flat, Alaska

The plasma in the Earth's ionosphere is a complex medium, with the electron density height profiles constantly changing with various temporal scales for any given location. The electron density distribution become particularly complex as one considers observations at high latitudes, where bombardment by energetic particles creates a great deal of variability in the ionization of neutral particles, both in time and space. The electron density distribution in the Earth's ionosphere has been studied for almost a century, and major features of the ionosphere have already been established (e.g., Brekke, 2013; Kutiev et al., 2013; Schunk & Nagy, 2009). However, many details still require refinement. This chapter assesses electron density distributions in the ionosphere over Poker Flat, Alaska where the PFISR incoherent scatter radar has been in operation since March 2007. This chapter focuses on seasonal and diurnal trends in the electron density variations. Two years of observations are considered, 2014 and 2016, corresponding to periods of relatively high and low solar activity, so that possible solar cycle differences can be evaluated. Besides a general curiosity about electron density profiles over Poker Flat, assessing the profiles is useful for understanding HF radio wave propagation paths for SuperDARN radars operating in this area such as the Kodiak, King Salmon, and Prince George radars. Exact radar locations are given in Nishitani et al. (2019) or on the Virginia Tech website (<http://superdarn.ece.vt.edu>).

### 3.1 Variations in solar activity over the last decade

Since the last maximum solar activity observed between 2001 and 2002, the Sun became calmer and has not shown as high levels of activity since this period, as shown in Figure 1.2 of Chapter 1. Only data for 2014 and 2016 are considered in this chapter, and the data from Figure 1.2 are re-

plotted on a shorter time scale, 2009 to 2020. Figure 3.1 presents monthly medians of the SSN and the F10.7-cm radio flux.

There is a great deal of similarity between the variations in the indices. Both indices show overall enhancements between 2011 and 2015. These years can be classified as a period of high solar activity in solar cycle 24. However, the actual values of SSN and F10.7-cm flux are not particularly high compared to other solar cycles (see Figure 1.2). Outside of the 2011 to 2015 period, month-to-month variations are small. During 2011 to 2015, the month-to-month variations in SSN and F10.7-cm flux are strong and not always synchronous. The plot of SSN has rather smooth and minor changes in 2014 while F10.7-cm flux was clearly enhanced at the beginning and at the end of the year.

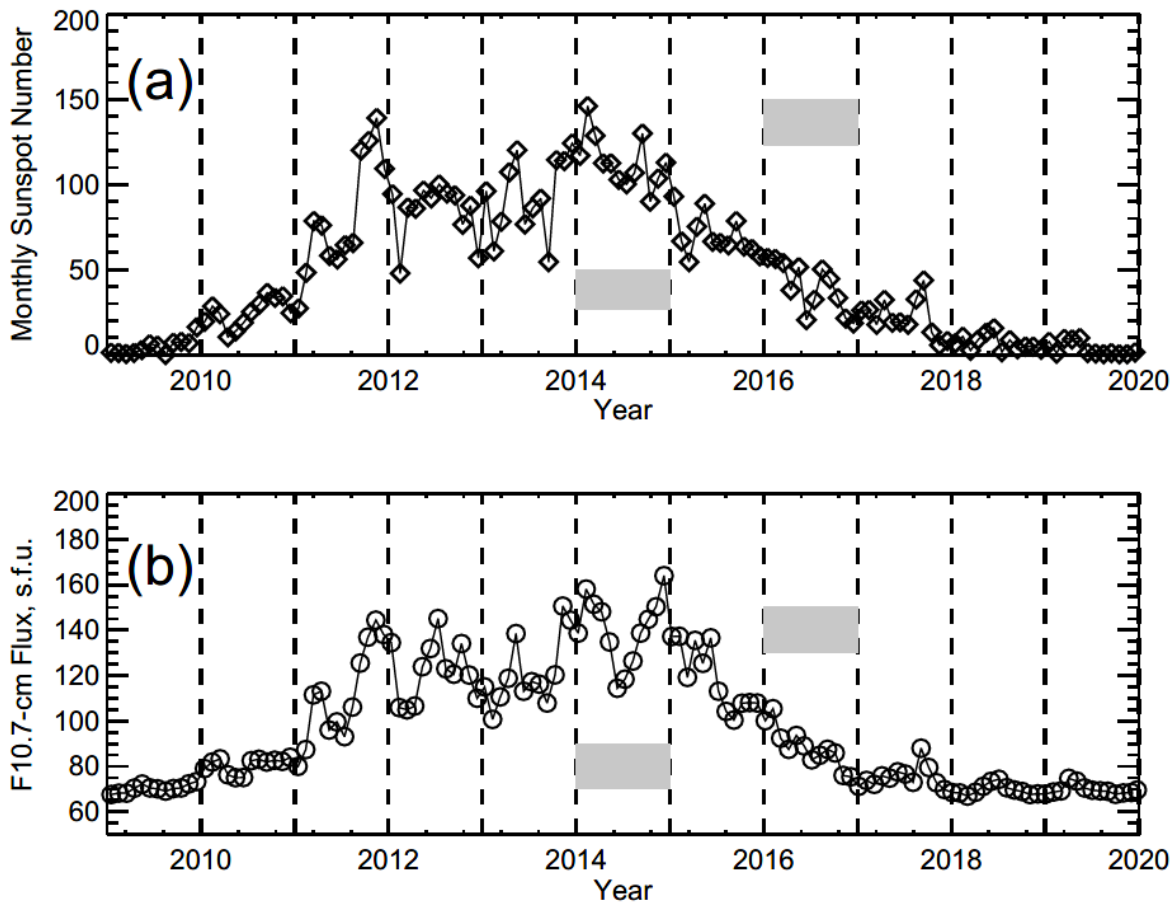


**Figure 3.1:** Variations of the solar activity between 2009 and 2020 as characterized by (a) the sunspot number (SSN) and (b) the F10.7-cm radio flux. Shaded horizontal bars mark periods selected for the ionospheric electron density analysis in this chapter. The SSN data were downloaded from <https://www.sidc.be/silso/newdataset> (Royal Observatory of Belgium, Brussels, 13 April 2023) while the F10.7-cm flux data were downloaded from <https://omniweb.gsfc.nasa.gov/form/dx1.html>.

The selection of PFISR observations in 2014 and 2016 was made for multiple reasons. First, the desire was to have data from periods of both high and low solar activity to identify any differences in the measurements due to solar cycle effects. An ideal analysis of this effect would include more years of measurements, which was not feasible to accomplish within the time limit of this thesis. Figure 3.1 shows that lowest SSN and F10.7-cm flux occurred from 2018 to 2020, which would give better contrast between high and low solar activity for the analysis. However, PFISR data available after 2016 are mostly 1-min resolution data, while 5-min resolution data are available from 2014 to December 2016. Chapter 2 shows that 1-min data might show different features in the ionospheric topside compared to 5-min data. The topside ionosphere is the primary interest of the analysis presented in Chapter 4, and the 5-min data available in 2016 were chosen for this reason. The other reason for the limited analysis is computation time. Downloading and median averaging PFISR data requires significant time if data for an entire year are considered. However, considering data for two extreme conditions will allow expected solar cycle differences in the profiles to be assessed, and further details can be investigated in the future. The choice of 2014, aside from the high solar activity as shown in Figure 3.1, is simply because it was the year when the Swarm satellites started regular observations and these measurements are of interest in Chapter 4.

## 3.2 Methodology of the analysis

For the analysis, 5-min integrated electron density data collected by the PFISR radar in the IPY mode were considered. The data consist of measurements from four beams near the zenith of the radar (see Chapter 2). The exception is December 2016, when only 1-min data were available. Although 1-min data can be different in quality compared to 5-min data, as discussed in Chapter 2, these are the only data available at this time and an entire year of measurements was desired. All the data were downloaded from the SRI International Website (<https://isr.sri.com/madrigal/>). The individual measurements in the four beams of observations were median averaged at every height in steps of 20 km.

PFISR data coverage versus month is presented in Figure 3.2. The coverage varied with time, with more data available for summer and daytime. For the PFISR location, the magnetic

midnight is at ~1100 UT (Whittier, 2014). Typically, ~100 or more profiles were available for each UT hour and for most of the months of each year.

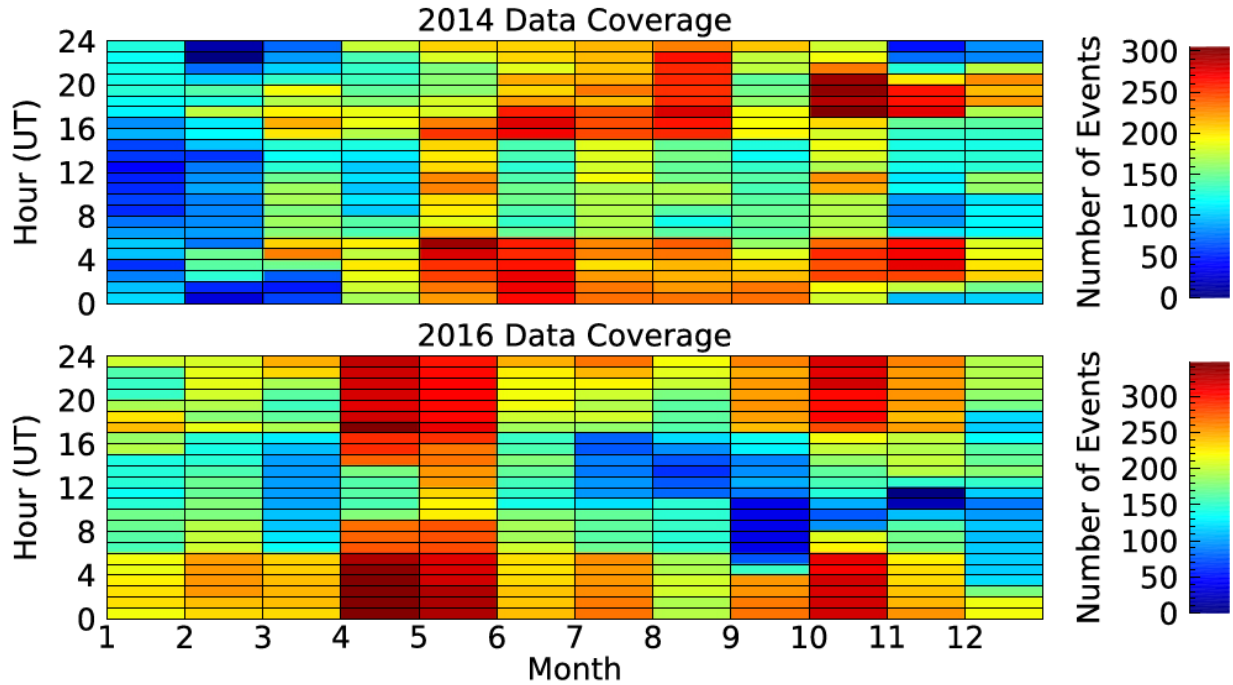


**Figure 3.2:** Number of Poker Flat ISR radar measurements on the UT-month plane for observations in 2014 and 2016.

### 3.3 Overall electron density profiles versus UT time

An overall survey of the electron density distribution is given by merging all the data in two separate data sets (2014 and 2016) and splitting each set on data for four seasons, Figure 3.3. The seasons were defined as spring (February through April), summer (May through July), autumn (August through October), and winter (November through January). The data were split in this way to analyze differences between electron density distributions at high and low solar activity versus time of the day separately for four seasons.

Figure 3.3 shows that the overall patterns are the same for all seasons and for both years with clear maxima around noon hours, from 20 to 02 UT where typical maximum values were on the order of  $80 \cdot 10^{10} \text{ m}^{-3}$  in 2014 and  $40 \cdot 10^{10} \text{ m}^{-3}$  in 2016. Minimum electron density values occur around late dusk to early morning sectors, 06-16 UT, with densities as low as  $15 \cdot 10^{10} \text{ m}^{-3}$  in 2014 and  $5 \cdot 10^{10} \text{ m}^{-3}$  in 2016. The data clearly show a dependence on solar activity. 2014 daytime electron density is greater than 2016 daytime electron density by a factor of ~2 ( $80 \cdot 10^{10} \text{ m}^{-3}$  and

$40 \cdot 10^{10} \text{ m}^{-3}$ , respectively). This solar activity effect is comparable with other high latitude locations from other studies. For example, Ma et al. (2009) presented data for the Norilsk ionosonde, their Figure 1. Norilsk is located at geomagnetic latitude of  $\sim 64^\circ \text{ N}$ , which is comparable with the latitude of Poker Flat. Their Figure 1 shows that electron density decreased by a factor of  $\sim 1.6$  for summer and  $\sim 1.8$  for winter, for F10.7-cm flux values decreasing from 130 and 80 s.f.u.

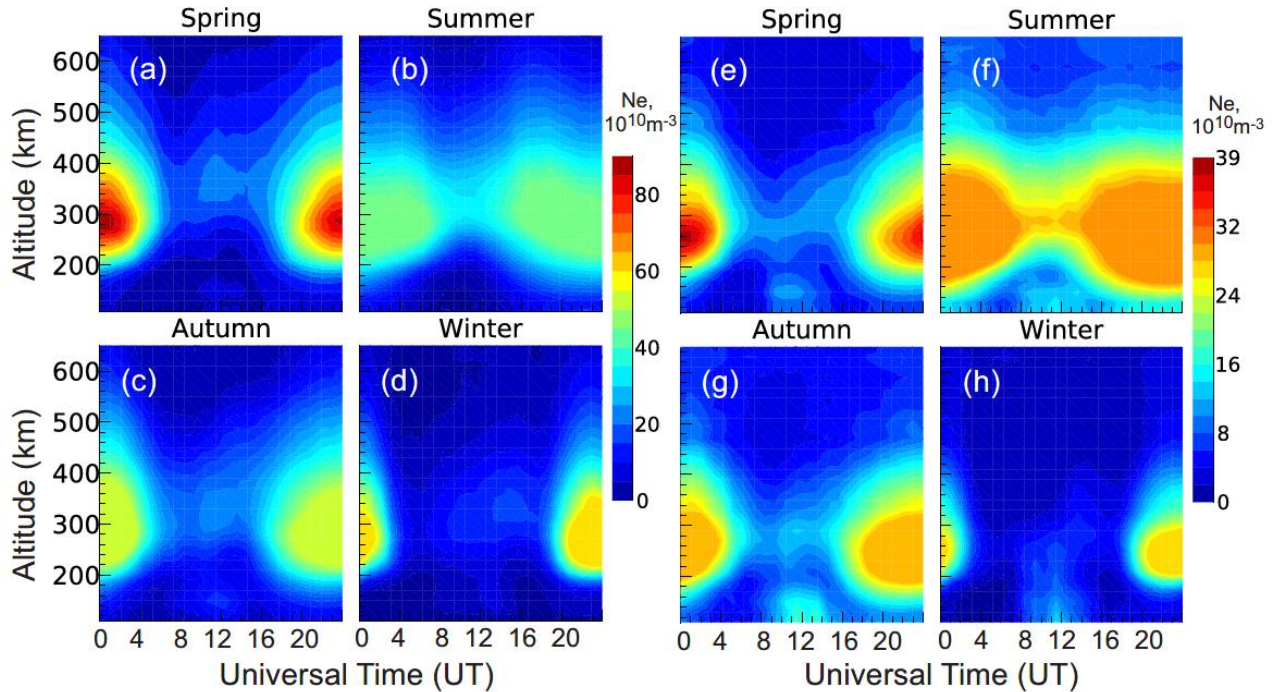


**Figure 3.3:** Electron density  $N_e$  at various heights versus UT for four seasons. Panels (a-d) and (e-h) are for observations in 2014 and 2016, respectively. The values are given in units of  $10^{10} \text{ m}^{-3}$ . All data obtained by the Poker Flat ISR in the International Polar Year mode were considered.

Ghezelbash (2013) presented data for the Sodankyla ionosonde, located at geographic (geomagnetic) latitude of  $67.4^\circ \text{ N}$  ( $64.1^\circ \text{ N}$ ). His Figures 1.6 and 1.7 show a decrease of daytime electron density, for a two-year separation on the decaying phase of solar activity, by a factor of  $\sim 3$ . This is a greater decrease compared to what is shown over Poker Flat, but the data presented by Ghezelbash (2013) were for much stronger solar cycles (22 and 23). Thus, the solar activity effect at Poker Flat is close to that in the Siberian and European sectors.

One interesting feature in the 2016 data presented in Figure 3.3 is an electron density enhancement around midnight (11 UT) at the ionospheric bottomside (150 to 200 km). Signatures of this feature are also recognizable in the 2014 data. Line plots of the data presented in Figure 3.3 at heights of 150 km, 300 km, and 450 km are shown in Figure 3.4. The solid and dashed lines show data for 2014 and 2016, respectively. The red and blue lines represent summer and winter,

respectively, in panels a, c, and e, and represent spring and autumn in panels b, d, and f. Analysis of the line plots for a height of 150 km shows that the enhancement is of a comparable magnitude in 2014.

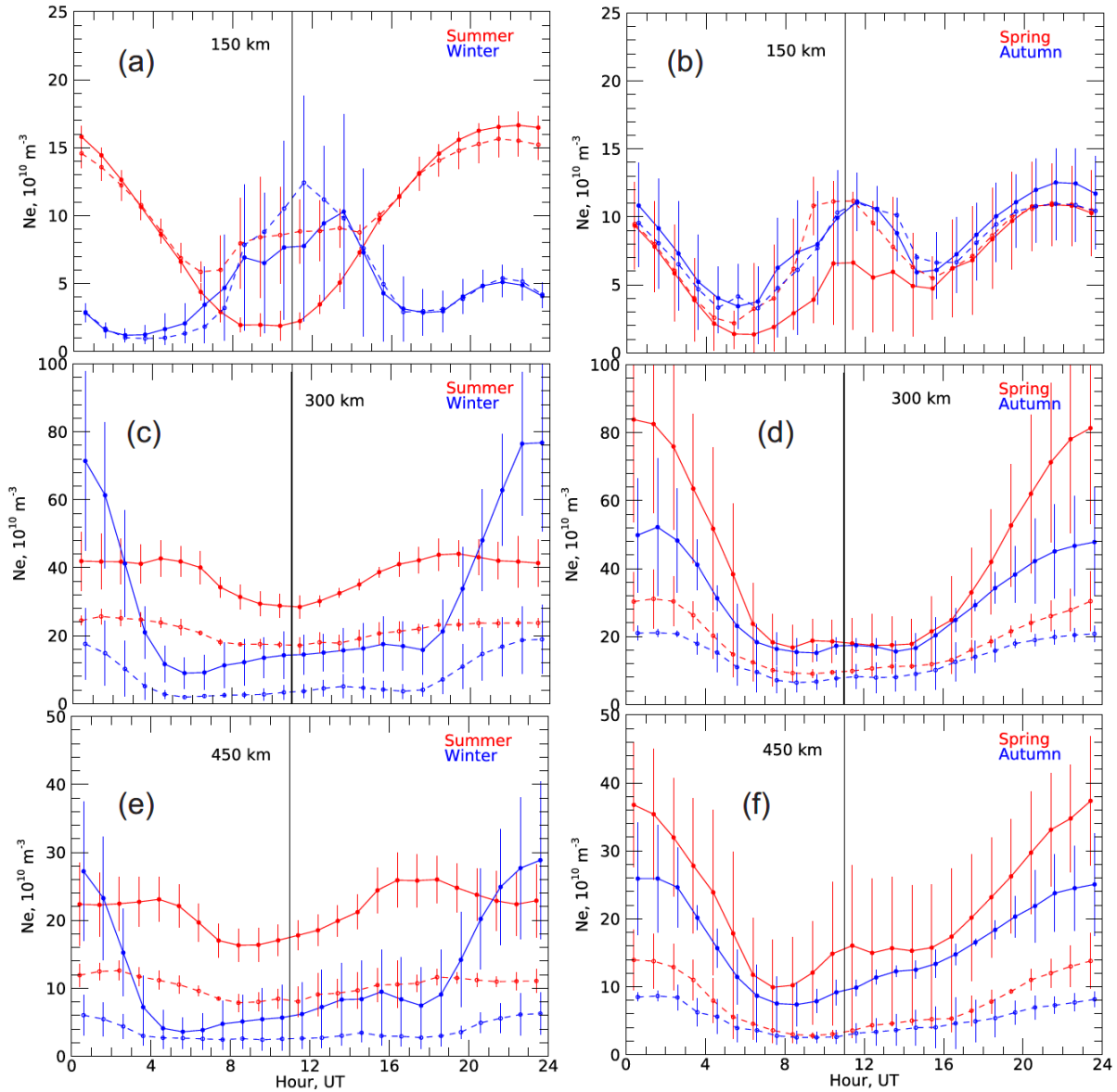


**Figure 3.4:** Line plots of the electron density  $N_e$  at the heights of 150 (panel a and b), 300 km (panels c and d), and 450 km (panel e and f) versus UT for 2014 (solid lines) and 2016 (dashed lines) as measured by the PFISR radar. The dots are hourly medians. Vertical bars are median values  $\pm$  one standard deviation for each bin of UT hour.

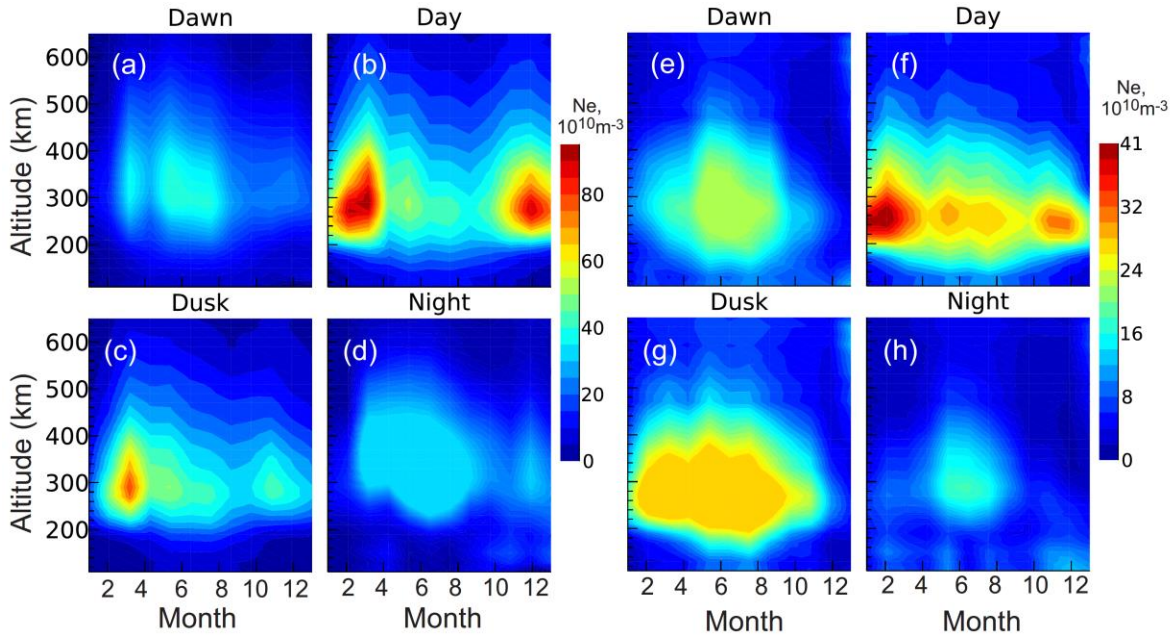
In terms of time of the day, the patterns of variations are the same for all seasons with the largest electron density values occurring during daytime and lowest values during nighttime. The day-night contrast is largest in winter and spring of 2014, where electron density is greater by a

factor of 4 to 5 during the day. This effect is smaller during spring 2016, where daytime electron density is greater by a factor of  $\sim 2.5$ . Daytime electron density is greater by a factor of  $\sim 1.3$  in summer, and  $\sim 3-4$  in autumn for both years. These values are obtained from line plots in Figure 3.4 of the electron density at  $\sim 300$  km, the central part of F2 layer. The winter data show the longest period of low electron density, lasting from  $\sim 5$  UT to 17 UT in 2014 and 03 UT to 19 UT in 2016 indicating more prolonged periods of low densities at low solar activity. A more detailed analysis of electron density variation versus UT at the ionospheric topside (450 km) is given in Section 3.8.

Figure 3.3 shows that the pattern does not change significantly with season, but the values vary noticeably. The largest electron density values were recorded in the spring for both 2014 and 2016 with smaller values in summer and lowest values in autumn and winter.

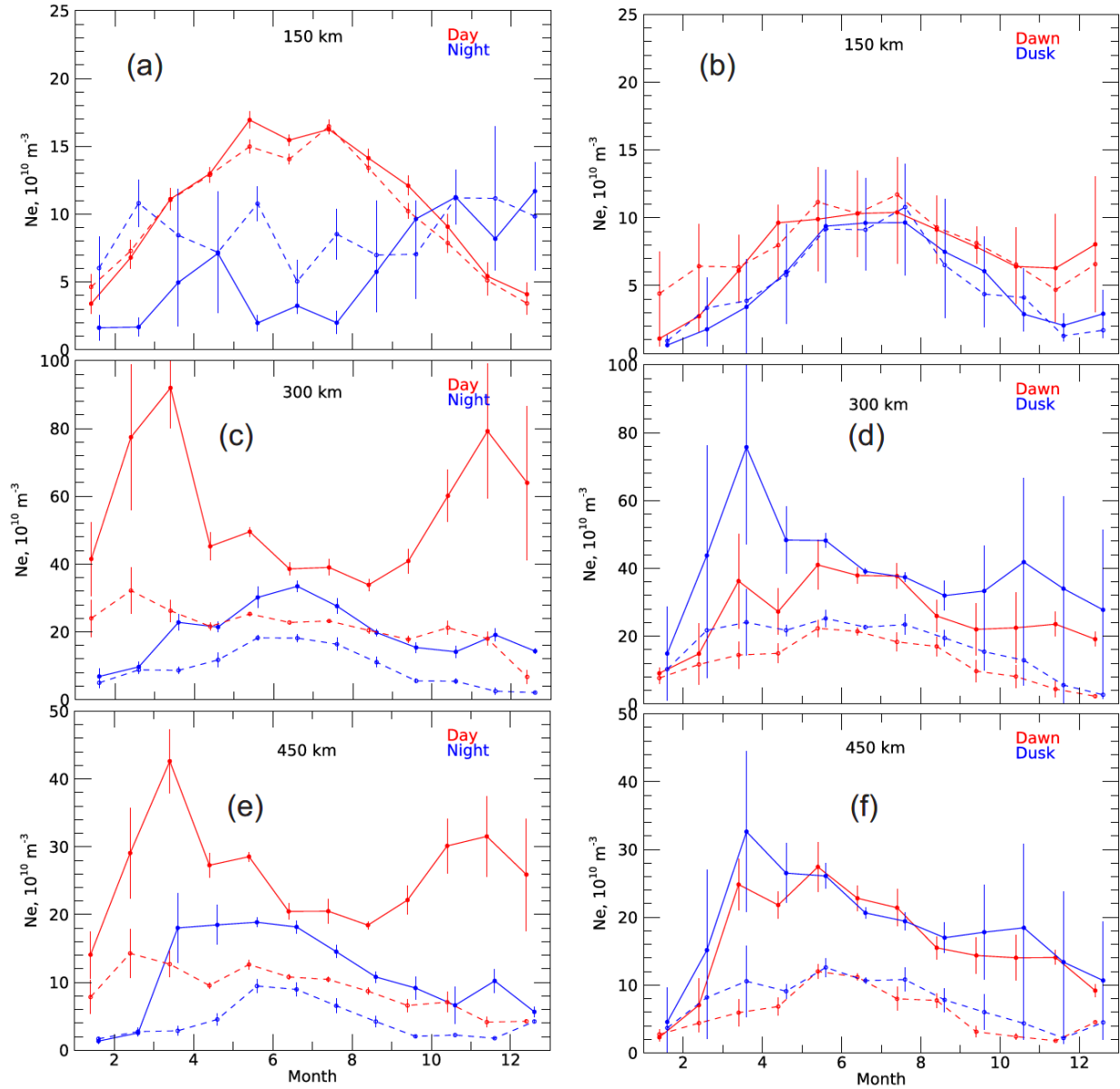
### 3.4 Overall electron density profiles versus season

To explore the seasonal variation of electron density in more detail, the data were grouped by time sector, separately for 2014 and 2016 and plotted in Figure 3.5, as Figure 3.3 clearly indicated different values over various seasons. The time sectors are defined as dawn ( $17 \text{ UT} \pm 3 \text{ UT}$ ), day ( $23 \text{ UT} \pm 3 \text{ UT}$ ), dusk ( $05 \text{ UT} \pm 3 \text{ UT}$ ), and night ( $11 \text{ UT} \pm 3 \text{ UT}$ ).



**Figure 3.5:** Electron density at various heights versus month in four time sectors. Panels (a-d) and (e-f) are for observations in 2014 and 2016, respectively. The values are given in units of  $10^{10} \text{ m}^{-3}$ . All data obtained by the Poker Flat ISR in the International Polar Year mode were considered.

Line plots of the data presented in Figure 3.5 for heights of 150 km, 300 km, and 450 km are shown in Figure 3.6. The solid and dashed lines represent data for 2014 and 2016, respectively. The red and blue lines represent day and night, respectively for panels a, c, and e, and represent dawn and dusk for panels b, d, and f.



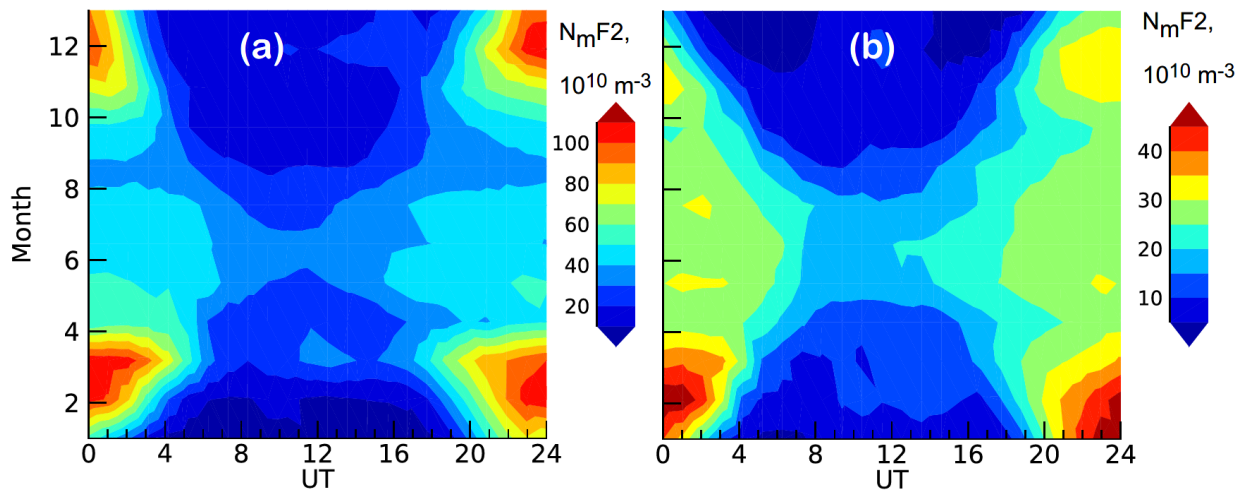
**Figure 3.6:** Line plots of the electron density  $N_e$  at the heights of 150 km (panels a and b), 300 km (panels c and d), and 450 km (panels (e) and f) versus month for 2014 (solid lines) and 2016 (dashed lines) as measured by the PFISR radar. The dots are monthly medians. Vertical bars are median values  $\pm$  one standard deviation for each month.

Figure 3.5 shows that the patterns of seasonal changes are different in 2014 and 2016. Although both years show maxima in winter and spring months during daytime and perhaps dusk, the summer-winter contrast is stronger in 2014 simply judging by the color of the contours. For other time sectors, an overall electron density enhancement toward the summer season is evident, shown clearly by the night data. The dusk data for 2014 show a strong enhancement in March. This enhancement correlates well with an increase of F10.7-cm flux, seen in Figure 3.1b, and is perhaps a seasonal anomaly specific for 2014.

Examining the summer-winter contrast for the dawn and night sectors shows that summer electron density is greater by a factor of 2 for dawn and  $\sim 3$  for night for both 2014 and 2016, as shown by Figure 3.6. The seasonal variations are more prominent during nighttime. One interesting feature from Figure 3.6 is that the daytime electron density at 150 km is maximized in the summer for both 2014 and 2016, opposite of the effect seen around 300 km in Figure 3.5.

### 3.5 Diurnal variation of $N_mF2$

The overall electron density profiles measured by PFISR change with time of day and season, and the shape of the profiles with respect to altitude is variable. This section analyzes seasonal and diurnal variations of the peak electron density,  $N_mF2$ , shown in Figure 3.7.  $N_mF2$  is a well-defined characteristic of every electron density profile. Many previous studies have examined this parameter in detail (Kutiev et al., 2013; Richards, 2001; Themens et al., 2018).



**Figure 3.7:** Electron density at the maximum of F2 layer ( $N_mF2$ ) versus UT for various months for (a) 2014 and (b) 2016. All data obtained by the Poker Flat ISR in the International Polar Year mode were considered. The values are given in units of  $10^{10} \text{ m}^{-3}$ .

Figure 3.7 presents  $N_mF2$  values on the month-UT plane. All the values inferred from the individual profiles in 2014 (panel a) or 2016 (panel b) were binned with steps of 1-hour and 1-month. The overall patterns for 2014 and 2016 are similar, with maximum  $N_mF2$  occurring around noon in winter and equinoctial months in 2014 and winter in 2016. The winter maximum is less evident at the end of 2016 (Figure 3.7b), corresponding to the period of lowest solar activity (Figure 3.1).

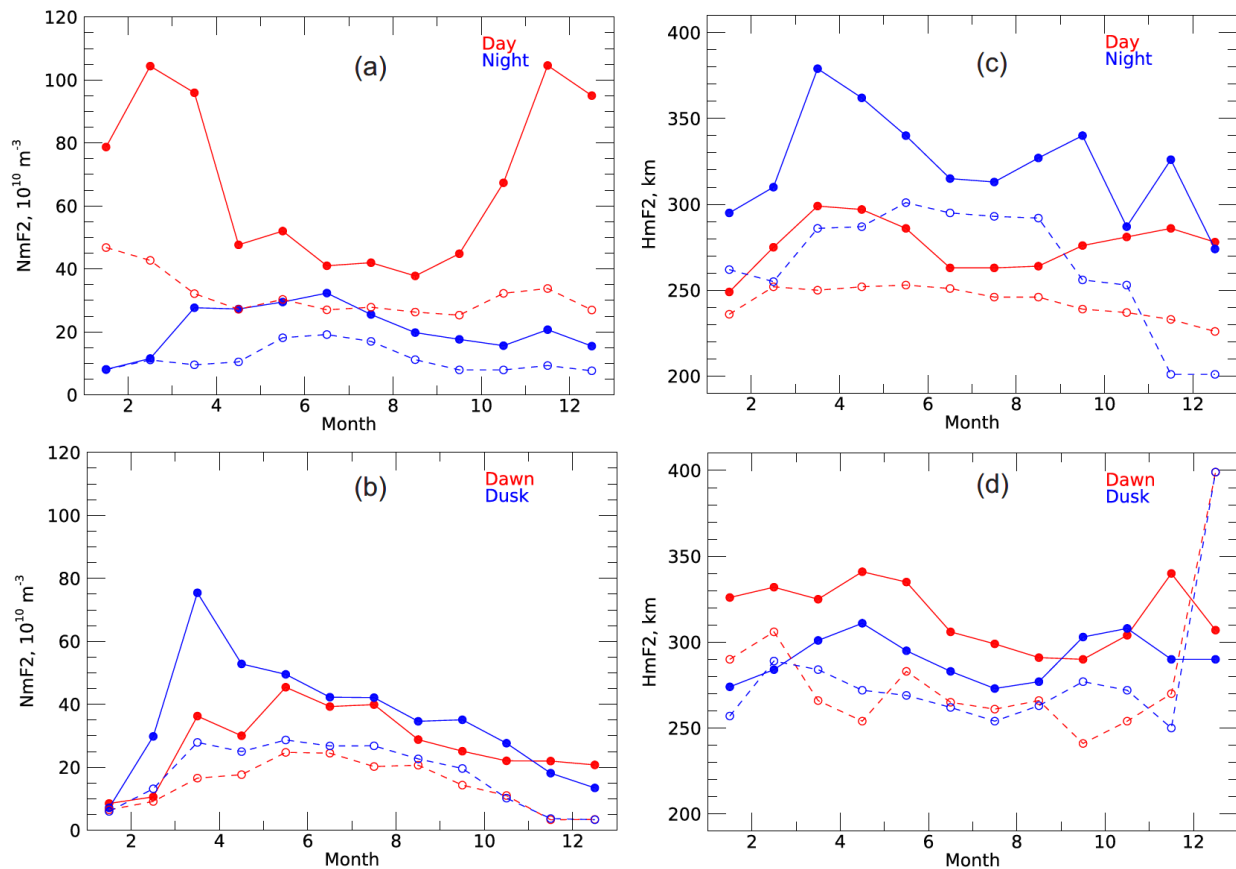


**Figure 3.8:** Line plots of the (panels a and b) peak electron density  $N_mF2$  and (panels c and d) peak height versus month for 2014 (solid lines) and 2016 (dashed lines) as measured by the PFISR radar. The dots are monthly medians.

Figure 3.8 shows line plots of the  $N_mF2$  (panels a and b) and  $h_mF2$  (panels c and d) for 2014 and 2016. The winter-summer contrast ratio, determined from Figure 3.8, is  $\sim 2.5$  in 2014 and  $\sim 1.5$  in 2016. Around local midnight ( $\sim 11$  UT),  $N_mF2$  values are maximized in summer. The summer-winter contrast ratio for night is  $\sim 2$  in both 2014 and 2016. Both plots in Figure 3.7 show “islands” of anomalous values, for example at 12 UT in April 2014. These “islands” indicate that

other periodicities are present in the data. These details probably reflect atypical geophysical conditions over Poker Flat.

### 3.6 Diurnal variation of $h_mF2$

Another well-defined parameter of electron density profiles is the height of the peak,  $h_mF2$ . This section analyzes seasonal and diurnal variations of this parameter.

Figure 3.9 is a contour plot of  $h_mF2$  on the UT-month plane. All the values inferred from the individual profiles in 2014 (panel a) or 2016 (panel b) were binned with steps of 1-hour and 1-month. The overall patterns for 2014 and 2016 are not quite the same although there are common features. The largest  $h_mF2$  values are reached during nighttime in spring of both 2014 and 2016, although the maximum values are larger by  $\sim 50$  km in 2014. However, the 2014 data also show an enhancement in autumn, which is not seen in 2016. The lowest heights are seen in summer of 2014 and 2016. Both 2014 and 2016 measurements show a relative decrease of heights in winter daytime.

The data for the dawn and dusk sectors show complicated patterns. One interesting feature in 2016 data is that the region of enhanced  $h_mF2$  forms a cross, which could be reflecting changes of the Sun's illumination of the ionosphere. This feature is not seen in 2014 data, perhaps because the ionosphere is more affected by particle precipitation events in 2014 due to greater solar activity. This feature requires further investigation in the future.

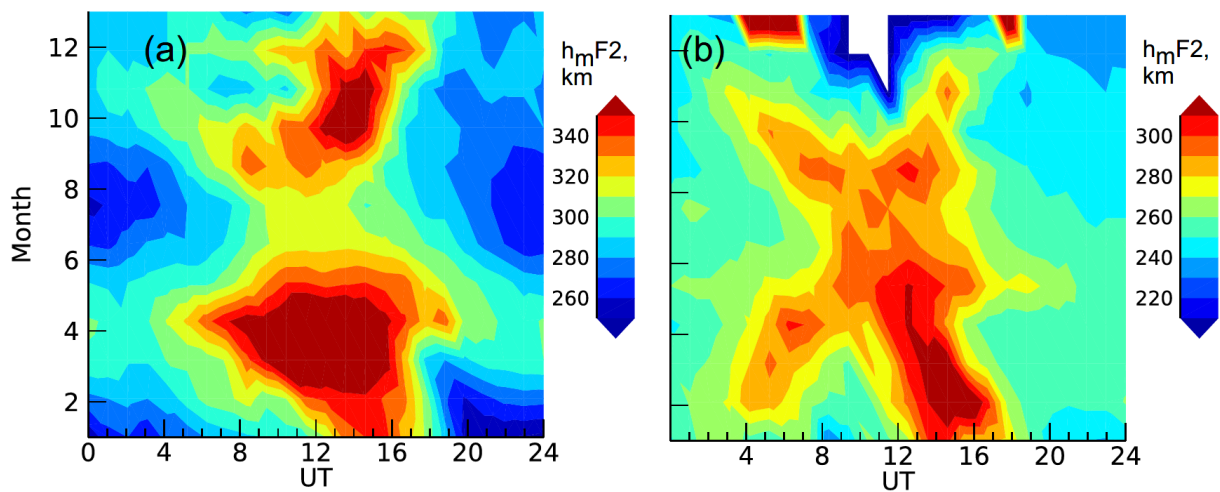


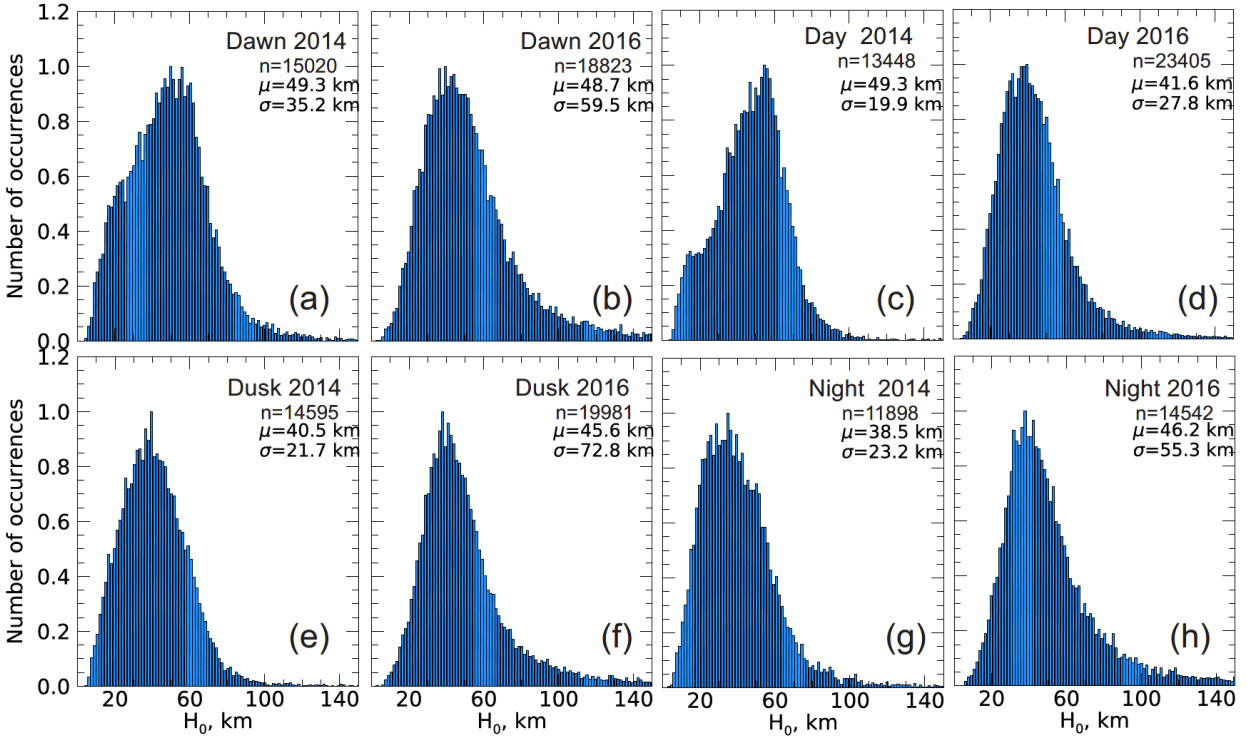
**Figure 3.9:** Height of the peak electron density of F2 layer ( $h_mF2$ ) versus UT for various months of (a) 2014 and (b) 2016. All data obtained by the Poker Flat ISR in the International Polar Year mode of observations were considered.

## 3.7 Trends in the thickness of the F2 layer inferred from NeQuick analysis

This section assesses the thickness of the F2 layer by applying the NeQuick model to the experimental data obtained by PFISR. A general description of the NeQuick model was given in Section 1.5. Electron density profiles in the topside ionosphere are represented as a semi-Epstein layer function characterized by three parameters,  $r$ ,  $g$  and  $H_0$  (equations 1.31, 1.32, and 1.33). Generally, all three parameters are independent, and all three parameters affect the shape of the profile. Themens et al. (2018) concluded that varying the  $r$  and  $g$  parameters had minor effects on the NeQuick profiles at high latitudes, and these parameters could be selected as fixed values of  $r$  equal to 20 and  $g$  equal to 0.2024. These typical  $r$  and  $g$  values determined by Themens et al. (2018) are significantly different than the original values stated as 100 and 0.125, respectively (Nava et al., 2008). Since the  $r$  and  $g$  parameters can be selected as fixed values, the focus of this section is trends in the scale height parameter  $H_0$ .

For the analysis, the 2014 and 2016 PFISR observations in the IPY mode were selected. The electron density profiles were fit with the Interactive Data Language (IDL) function CURVEFIT with  $r$  and  $g$  set to constant values of 20 and 0.2024, respectively. A value for the scale height at the F2 layer peak, or scale height parameter  $H_0$ , was then determined for each PFISR electron density profile. The results are displayed in Figures 3.10, 3.11, and 3.12.

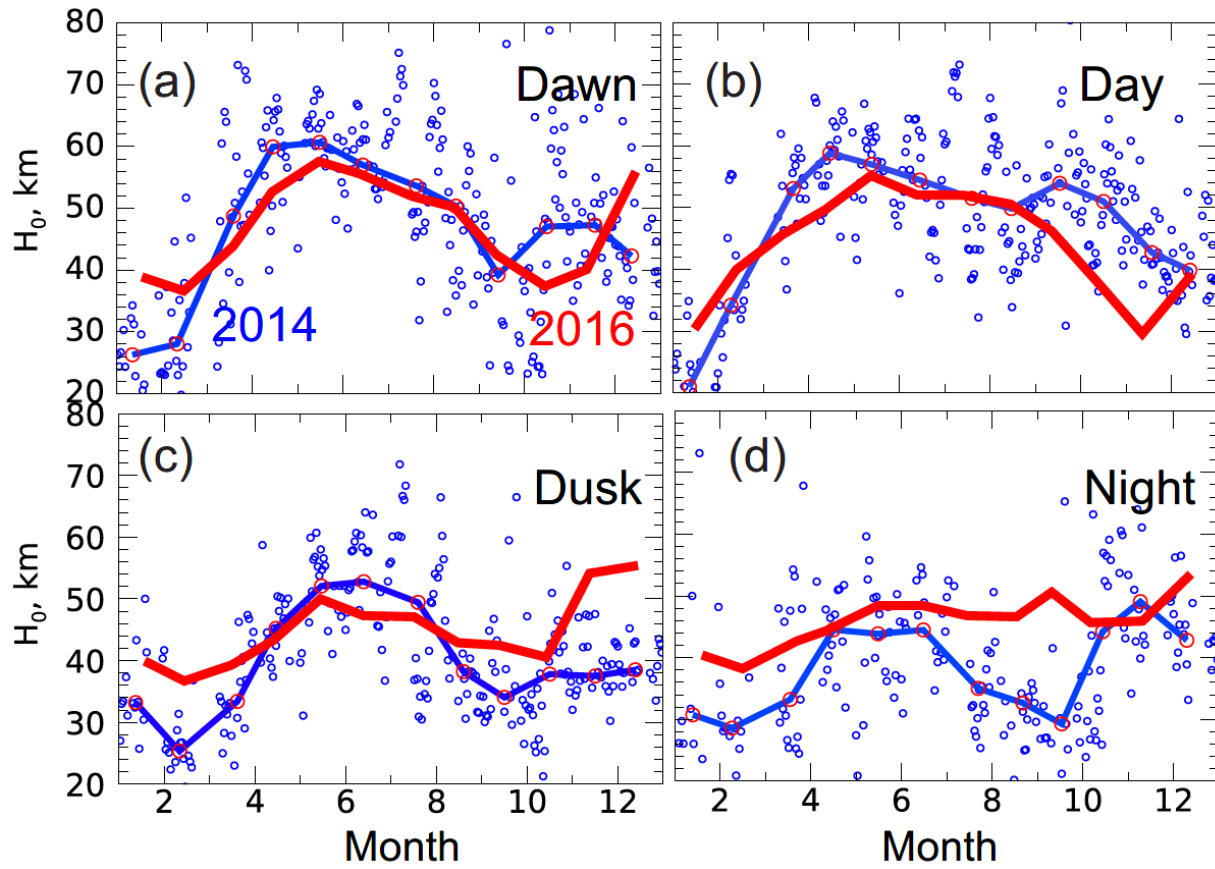
Figure 3.10 shows histogram distributions of the parameter  $H_0$  for the four different time sectors, separately for 2014 and 2016. The panels are paired such that for each season 2014 and 2016 data are displayed side-by-side, so that high and low solar activity histograms can be compared directly. Figure 3.10 indicates that, overall,  $H_0$  is largest during daytime (largest median value  $\mu$ ) and smallest during nighttime (smallest  $\mu$ ). The distribution of  $H_0$  values is narrower during the daytime (smallest standard deviation  $\sigma$ ). Overall, the differences between 2014 and 2016 data are not large. The 2014 data for dawn and day show an additional enhancement at small values, making the distributions more distorted and less of a Gaussian compared to the rest of the distributions. The main conclusion from these plots is that, on average, the thickness of F2 layer stays in between 20 km and 70 km.



**Figure 3.10:** Histogram distributions of the parameter  $H_0$  in four separate time sectors. All data obtained by the Poker Flat ISR in the International Polar Year mode of observations were considered. Each panel shows the total number of points  $n$ , median  $\mu$ , and standard deviation  $\sigma$ , of the distribution.

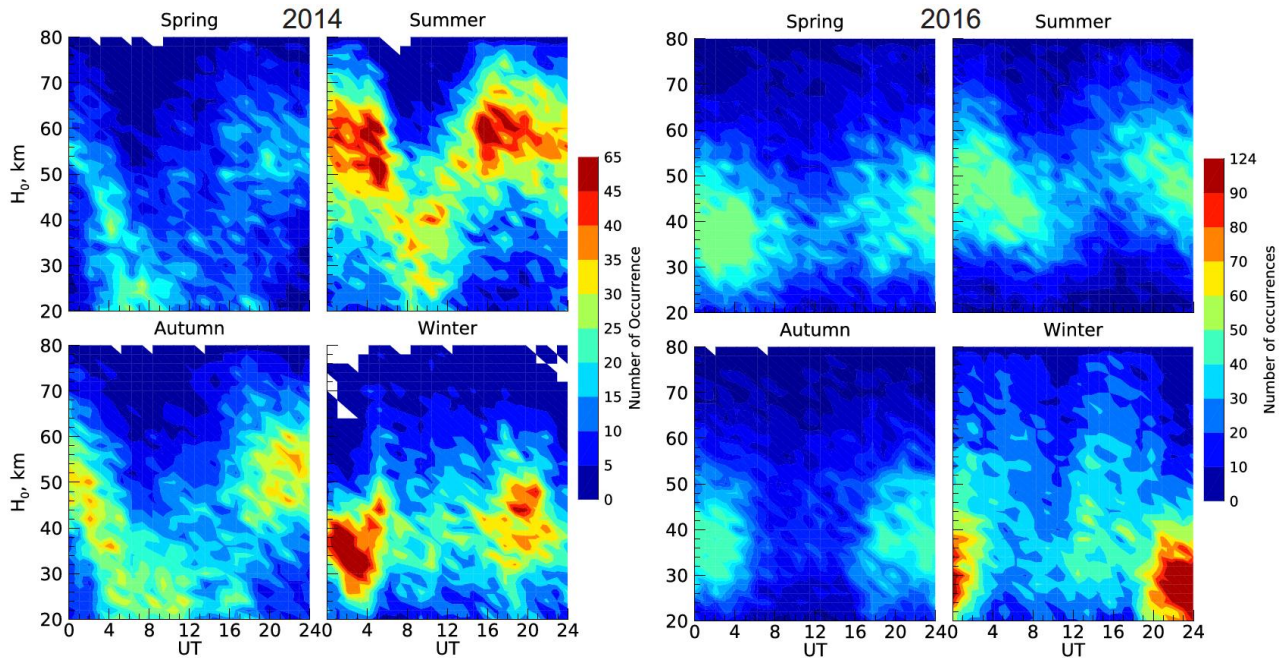
The histogram distributions in Figure 3.10 give a sense of typical values of  $H_0$ . Because the electron density distribution in the ionosphere is known to vary with season (e.g., Figure 3.5), the  $H_0$  data are split by time sector and plotted versus year in Figure 3.11 to assess seasonal changes in  $H_0$ . Single blue points in Figure 3.11 represent daily medians of  $H_0$  in 2014, the solid blue and red lines show the monthly medians of  $H_0$  for 2014 and 2016, respectively. The daily medians for 2016 are not shown in Figure 3.11 as the data show a comparable cloud of points as those shown in Figure 3.11.

Figure 3.11 shows that the trends in  $H_0$  monthly medians versus season are comparable in 2014 and 2016, with less degree of agreement during night hours.  $H_0$  values are largest during the summer at dawn and daytime, except for November and December 2016 where  $H_0$  values are larger than those reported in the summer for the dawn and dusk sectors. The decline of  $H_0$  from summer to winter is very clear during daytime, and the effect is not as noticeable during nighttime.



**Figure 3.11:** Scatter plots of the parameter  $H_0$  (open blue circles) versus time of the year (month) for four separate time sectors of measurements in 2014. Solid blue lines represent monthly median values in 2014. Solid red lines are monthly medians for measurements in 2016.

Because the electron density distribution in the ionosphere is known to vary with time of the day (e.g., Figure 3.5), Figure 3.12 illustrates how  $H_0$  varies with time of day. Figure 3.12 is a four-panel contour plot (corresponding to four seasons) for  $H_0$  occurrence versus UT time in 2014 (left four panels) and 2016 (right four panels). Figure 3.12 shows that the pattern of occurrence for specific  $H_0$  values are similar in 2014 and 2016. During daytime, summer  $H_0$  values are the largest and winter values are the smallest. During nighttime, the differences are less obvious. Patterns in  $H_0$  versus UT time near equinox in spring and autumn are similar to each other.



**Figure 3.12:** Contour plots for the parameter  $H_0$  occurrence versus UT time for four seasons in 2014 (left four panels) and 2016 (right four panels).

### 3.8 Diurnal and seasonal variations in the ionospheric topside

One of the reasons for assessing the electron density distribution over Poker Flat was to identify periods of large electron densities at the ionospheric topside. A specific area of interest is heights  $\sim 450$  km, where the Swarm satellites have been measuring electron density with Langmuir Probes since 2014, as reported in Chapter 2. Previous Swarm validation work by Larson et al. (2021) for the polar cap area (Resolute Bay) revealed that measurements at large electron densities are critical for understanding how the Swarm electron density measurements compare to measurements from ISRs. It is also important to establish an understanding of typical conditions in the ionosphere where the joint satellite-radar measurements are taken to determine if these measurements correspond to typical conditions. There is also a general curiosity about electron density trends at heights above the F2 layer peak (e.g., Kutiev et al., 2013; Themens et al., 2018). This section will investigate the typical electron density values and trends at heights of 450 km for two years of observations, 2014 and 2016, corresponding to high and low solar activity.

Figure 3.4e shows the diurnal variation of the electron density at a height of 450 km.

Data for 2014 show three interesting features. First, at nighttime the electron density is the smallest, with values ranging from  $5 \cdot 10^{10} \text{ m}^{-3}$  to  $15 \cdot 10^{10} \text{ m}^{-3}$ . In winter, these values are smaller than in summer by a factor of 2 to 3. Second, the decrease of the nighttime electron density in winter is greater than in summer, and decreased densities last for a longer period of time, 04 to 19 UT in the winter compared to 06 to 15 UT in the summer. Third, during daytime from 22 to 01 UT, the electron densities are largest in the winter. This is a phenomenon similar to the winter anomaly (WA) effect for  $N_m F2$ .

Data for 2016 show that electron densities are  $\sim 2$  times smaller for both winter and summer compared to 2014, reflecting a decrease in solar activity. The data also show a decrease of electron density during nighttime, similar to the 2014 data, by a factor of 4 to 5. The WA effect observed in the 2014 data does not exist in 2016.

Figure 3.6e shows seasonal trends in electron density at a height of 450 km. The 2014 data, represented by solid lines, show an enhancement in electron density near equinoctial time during daytime, with lowest values occurring in the winter. Nighttime electron density is enhanced from March to September, with the smallest values again occurring in the winter. The difference between day and night data is small during the summer, but much greater during the winter where daytime densities are larger than nighttime densities by a factor of 5 to 10.

The 2016 data, represented by dashed lines, do not show equinoctial enhancements during daytime. Instead, the electron densities steadily decrease toward the end of the year, corresponding to a decrease in solar activity shown in Figure 3.1. The nighttime data show a clear summer enhancement which is more pronounced compared to the 2014 data. The major conclusion made from Figure 3.6e is that seasonal variations are different for 2014 and 2016.

## 3.9 Discussion of the results

The results presented above are a contribution to the knowledge of the ionosphere for a specific region over Poker Flat, Alaska. Poker Flat is located at magnetic latitude of  $61.2^\circ$  (Michell et al., 2014) implying that during daytime the radar is located equatorward the auroral oval and can be considered as a subauroral/midlatitude station. During nighttime, the radar is in the subauroral region. During periods of strong magnetic activity or substorms the auroral oval expands equatorward, and the radar can be within the auroral oval (Brekke, 2013, Fig. 7.12). Therefore, the radar will detect enhanced electron densities below 150 km, in the upper E region and bottomside

of the F region during nighttime, shown by Figure 3.3 (e) to (h). These midnight enhancements of electron density are similar to near-midnight enhancements detected by ISRs in the polar cap, related to a poleward expansion of substorm active regions (Cai et al., 2007).

### 3.9.1 Solar cycle variation

The data presented in this chapter clearly indicate a dependence of the electron density on solar activity. The overall decrease of the electron density from 2014 to 2016 was evident in the contour plots for the central part of F2 layer (Figure 3.3),  $N_mF2$  (Figure 3.7), and the ionospheric topside (Figure 3.4e). A quantitative estimation of the effect has been done with respect to  $N_mF2$  for the middle latitudes (e.g., Alfonsi et al., 2009; Ma et al., 2009; Richards, 2001; Sheng et al., 2007).  $N_mF2$  increases almost linearly with F10.7-cm flux up to 200 s.f.u. where it begins to saturate (e.g., Ma et al., 2009; Özgüç et al., 2008). For F10.7-cm flux ranging from 80 to 130 s.f.u., corresponding to the range of values for 2016 and 2014, an increase of  $N_mF2$  is estimated to be a factor of 2 to 3 for most of stations shown by Ma et al. (2009) in their Figure 1.  $N_mF2$  at high latitudes is not investigated as thoroughly as at low latitudes. Themens et al. (2017) presented ionosonde data for several locations in the Canadian Arctic. Data from the ionosonde in Eielson, Alaska (their Figure 2) show that  $N_mF2$  in the winter decreases by a factor 2 from 2014 to 2016. Figure 3.7 of the current study shows a stronger solar cycle effect, with a decrease of daytime  $N_mF2$  by a factor of 4 to 5.

### 3.9.2 Seasonal variation

The data presented in this chapter also indicate a seasonal dependence of the electron density. The most remarkable feature in the data is the presence of a strong WA effect. The WA effect is the occurrence of stronger daytime electron densities in the winter ionosphere compared to the summer ionosphere (Yasukevich et al., 2018). This is counterintuitive to the expectation that sunlight would produce more electron-ion pairs during periods with more exposure to sunlight (Yasukevich et al., 2018). The WA effect is strongest at middle latitudes in the North American sector (Yasukevich et al., 2018). As mentioned, Poker Flat is located equatorward of the auroral oval, and signatures of the WA are expected. Figure 3 indicates that the WA effect is stronger in 2014, at higher solar activity. The ratio of winter to summer electron density is  $\sim 2$  in 2014 and  $\sim 1.5$  in

2016, which is expected. The data from the Sodankyla ionosonde reported by Ghezelbash (2013) also show that the WA effect only occurs at high solar activity, agreeing with the results shown in Figure 3.4e for the ionospheric topside.

An interesting result of the WA effect is an expectation of more frequent occurrence of ground scatter in SuperDARN observations with the Kodiak (Alaska) radar. A brief inspection of the Kodiak radar data on the Virginia Tech website (<http://superdarn.ece.vt.edu>) appears to support this expectation, but a detailed analysis similar to the analysis performed by Koustov et al. (2022) is required to confirm it.

Another feature identified in the data is a weaker seasonal variation in electron density for daytime  $N_mF2$  during lower solar activity. The effect is also observed in other locations, such as in the Sodankyla data presented by Ghezelbash (2013) in their Figure 1.6. It should be noted that the seasonal variation in 2014 reported in this chapter (Figures 3.4, 3.9 and 3.11) is likely affected by strong changes in solar activity within the year, as indicated by the F10.7-cm flux variations shown in Figure 3.1. A similar analysis for a year with less sporadic behavior in F10.7-cm flux is required.

Seasonal variations in  $N_mF2$  for the Tromso ionosonde in Europe have been investigated by Xu et al. (2007). Tromso (Norway) is located at a geographic latitude of  $69.6^\circ$  N, somewhat poleward of Poker Flat. The plots presented by Xu et al. (2007) agree with the results of this study presented in Figure 3.7. Figure 3.4e shows that during nighttime, electron density is higher in the summer and lower in the winter. This result is consistent with results obtained from ionosonde data (e.g., Alfonsi et al., 2009; Themens et al., 2017; Xu et al., 2007) and does not require further discussion.

### 3.9.3 Diurnal variation

The data presented in this chapter also indicate strong diurnal variations of electron density. These diurnal variations are a well-known feature in the ionosphere for individual events. For example, Whittier (2014) presented data for a single day of equinoctial PFISR observations in 2007, a year with low solar activity. Figure 3.13, from Whittier's M.Sc. thesis, indicates that his reported electron density distribution is typical for the Poker Flat location, with maximum electron densities of  $\sim 30 \cdot 10^{10} \text{ m}^{-3}$  during daytime and minimum electron densities of  $\sim 3 \cdot 10^{10} \text{ m}^{-3}$  during nighttime. The minimum electron densities reported by Whittier (2014) are lower than typical values that are

presented in Figure 3.6. According to Figure 3.13, the heights  $h_mF2$  are  $\sim 250$  km during daytime and larger during nighttime, with strong variations. These values are consistent with the typical values reported in Figure 3.9 for daytime. The typical values during nighttime from Figure 3.9 are  $\sim 300$  km.  $h_mF2$  values greater than 500 km are a rare phenomenon. Thus, the data presented in this chapter provide benchmark electron density profiles as a function of UT.

Data presented in Figure 3.9 about the height of the F2 layer are consistent with the expectation that the peak height is larger at nighttime compared to daytime (Themens et al., 2018). The largest heights for  $h_mF2$  occur more frequently during equinoctial nighttime (Figure 3.9 for 2014). Richards (2001) performed an extensive analysis of  $h_mF2$  at middle latitudes. His plots also show larger heights at nighttime. However, the seasonal dependencies are different during daytime and nighttime. For some locations, e.g., Port Stanley shown by Richards (2001) in his Figure 7, daytime  $h_mF2$  values increase during the winter, with greater increases at higher solar activity, while nighttime seasonal changes are less significant. The data presented in Figure 3.9 show stronger seasonal variations at nighttime for both 2014 and 2016.

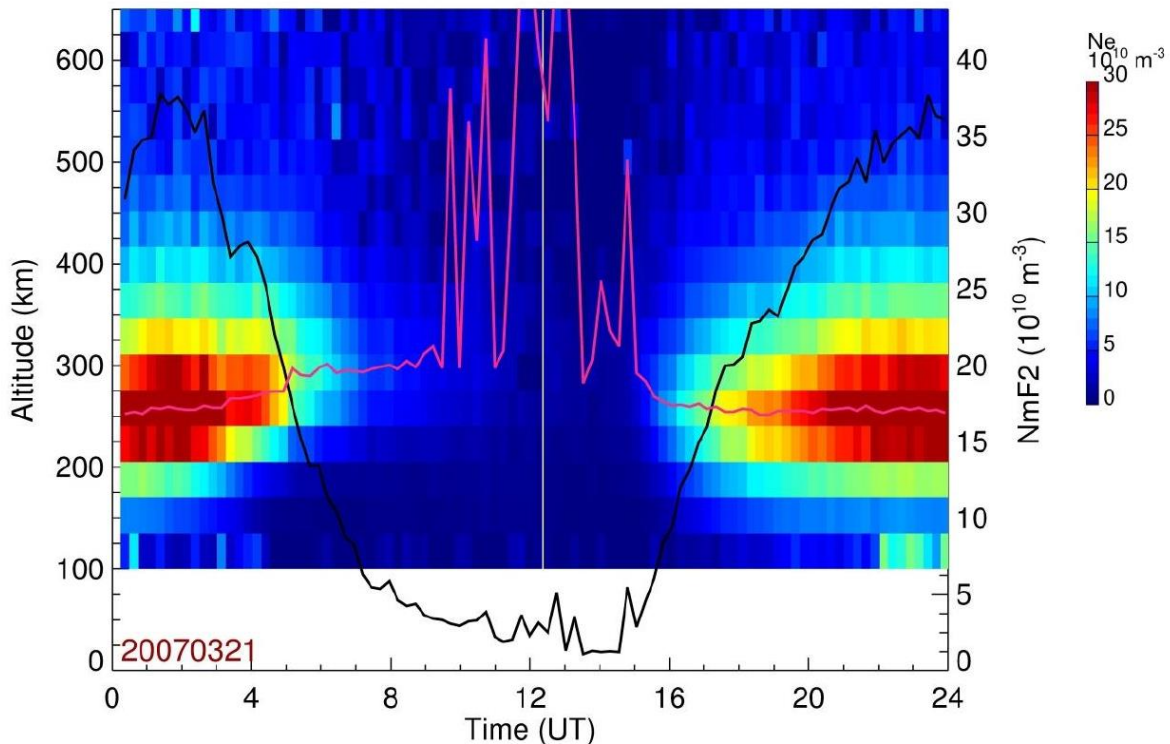


**Figure 3.13:** Diurnal variation of the electron density as measured by the Poker Flat ISR system near Fairbanks, Alaska on 21 March, 2007. ISR-derived  $h_mF2$  is shown by the pink line and ISR-derived  $N_mF2$  is shown by the black line. From Whittier (2014).

### 3.9.4 Thickness of F2 layer and electron density in the ionospheric topside

Results on the thickness (scale height parameter  $H_0$ ) of the ionospheric F2 layer, inferred with the NeQuick analysis, confirm that the layer is thicker (i.e., a more inflated ionosphere) during high solar activity, specifically in the day and dawn time sectors. Seasonally, the ionosphere is more inflated near equinoxes or summer, shown by largest  $H_0$  values in Figure 3.11. When the ionosphere is more inflated during these seasons, electron density in the topside ionosphere is expected to be higher than the other seasons. This effect can be recognized in the data of Figure 3.4e as well. Thus, the lowest electron densities occur in winter and on the nightside. This conclusion is consistent with observations in the polar cap with RISR-C radar (Larson et al., 2023). One potential implication of these findings is that winter electron density measurements with the Swarm LP instruments occur under a lower density ionosphere. Larson et al. (2021) indicated that the LP instruments might overestimate the densities in this environment (their Figures 4.6 and 4.7). This overestimation effect has not been discussed until recently (e.g., Xiong et al., 2022). This overestimation effect will be investigated further in Chapter 4 of this thesis.

The diurnal and seasonal variations in the topside ionosphere  $\sim 450$  km are not commonly discussed in literature, to the best of my knowledge. Several interesting findings that were expected but now confirmed by this study are as follows. A decrease in electron density during nighttime is stronger during high solar activity. Largest daytime electron densities occur in the winter, not the summer, which is an analogue of the WA effect for  $N_mF2$ . The seasonal variation in the topside ionosphere was found to be strong during high solar activity, although this could be a result of the enhancement of F10.7-cm flux during equinoctial times in 2014 (Figure 3.1).

Publications focusing on the diurnal and seasonal variations of electron density trends in the topside ionosphere are limited. Themens et al. (2018) investigated the NeQuick (and E-CHAIM) model predictions based on the electron density profiles' shape for multiple years of measurements from four ISRs. They determined that the original suggested values for parameters  $r$  and  $g$  in the NeQuick model does not result in a good representation of the topside ionosphere at high latitudes. They concluded that the topside ionosphere is better represented with the selection of new  $r$  and  $g$  parameters of 20 and 0.2024 respectively. These values have been adopted for the analysis of  $H_0$  in this thesis.

If the fixed values of  $r$  and  $g$ , suggested by Themens et al. (2018), along with the optimized values of  $H_0$  for each individual profile are used in the NeQuick model, the electron density can be determined at every height by equation 1.31. The electron densities produced by the NeQuick model can be compared to the PFISR measurements at a height of 450 km to verify whether the PFISR measurements support the predictions from the NeQuick and E-CHAIM ionospheric models in the topside ionosphere. The results of this comparison are shown in Figure 3.14.

Figure 3.14 shows the hourly medians of the electron densities at 450 km for (a) summer (red) and (b) winter (blue) for observations in 2016. These are the same values shown in Figure 3.4e and are direct measurements from PFISR. The grey dots represent individual electron density values predicted by the NeQuick model at 450 km for each profile. The green dots connected by the green line represent the hourly medians of the values obtained from NeQuick model. The vertical bars are the median value  $\pm 1$  standard deviation of the individual values in each hourly bin.

Figure 3.14 shows great variability in the individual NeQuick values by the large cloud of grey dots and the standard deviation in each bin. The difference between the individual values and the median values measured directly from PFISR can be as large as a factor of 2. However, the medians of the predicted values, shown by green, are very close to the actual PFISR measurements, and the trends in the data are the same. This result shows that the NeQuick (E-CHAIM) predicted electron density values above the F2 region peak agree with the actual measurements from PFISR in 2016. A similar analysis can be conducted to determine how the NeQuick model performs with seasonal variations in electron density, by plotting NeQuick predicted values and PFISR measurements with respect to month. This analysis was performed, and good agreement was found between the NeQuick predictions and actual PFISR measurements, but the plots are not presented here.

The comparison in Figure 3.14 supports one of the main conclusions of Themens et al. (2018) that the fixed values of the  $r$  and  $g$  parameters in the NeQuick model adopted for E-CHAIM reproduce the diurnal variation in electron density reasonably well.

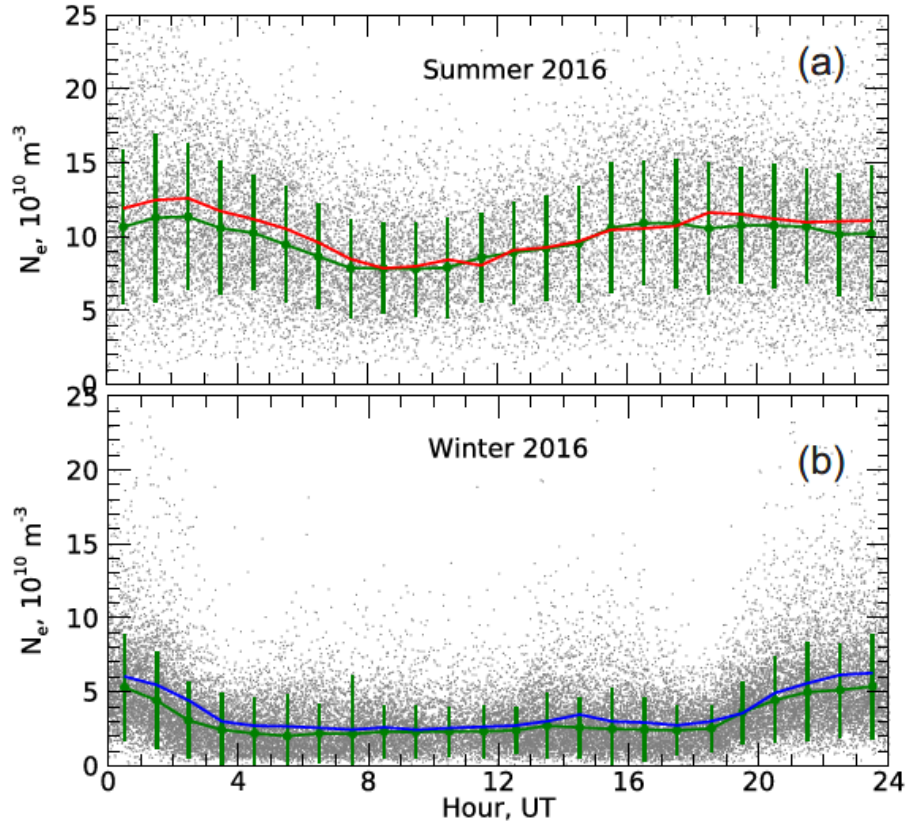


**Figure 3.14:** Line plot of the hourly medians of the electron density at a height of 450 km versus UT time as measured by the PFISR radar in (a) summer (red line) and (b) winter (blue line) for 2016. Grey dots are the electron density  $N_e$  values inferred from the NeQuick model for each individual  $N_e$  profile. Solid green dots connected by the green line are the hourly medians of the  $N_e$  values inferred from NeQuick.

### 3.9.5 Electron density variations in the ionospheric bottomside

The end of the discussion will focus on the electron density in the ionospheric bottomside. The bottomside ionosphere is not a major area of interest for this thesis, but it is a very important region of the ionosphere and the subject of many other publications (e.g., Themens et al., 2019a). Presented in Figure 3.6a and Figure 3.6b are line plots of electron density measured by PFISR at a height of 150 km. One major feature shown in the two figures is that the solar cycle effect is not strong at this height. During the day, shown by the red curves, 2014 (solid) and 2016 (dashed) curves show very similar values. Electron density for both years is maximized during the summer and minimized during the winter. The data for nighttime, shown by the blue curves, have less agreement between the two years of observation. Overall, electron densities are maximized during summer daytime.

## 3.10 Conclusions

The data presented in this chapter illuminated several features in the electron density distribution over Poker Flat, Alaska. These features are consistent with previous findings at other locations, notably at middle latitudes. The results from this chapter provide benchmark values of the electron density over Poker Flat for a variety of ionospheric conditions. The data and plots presented here can be used for testing global scale ionospheric models, and for planning future experiments involving HF radars or HF radio links, for example. The major conclusions of this chapter, and contributions to the knowledge of the electron density in the high latitude ionosphere over Poker Flat are as follows:

1. The daytime electron density increases with F10.7-cm radio flux for values below 200 s.f.u., consistent with a linear increase identified for other locations. This dependence is less pronounced in other time sectors.
2. The dependence of the ionospheric bottomside on F10.7-cm flux is not as strong compared to the F region peak and the topside.
3. Electron density varies with season and the dependence is different on the dayside and nightside. During daytime around local noon, electron density is maximized in the winter and close to the spring equinox. During nighttime, electron density is maximized in the summer.
4. Diurnal variation shows that the maximum electron density is larger during daytime compared to nighttime. The day-night contrast is stronger during winter and at higher solar activity.
5. The height of the F2 layer peak is larger during nighttime by ~50 km compared to daytime.
6. The electron densities in the ionospheric topside show solar cycle, seasonal, and diurnal variations similar to those identified for the peak electron density.
7. The ionospheric F layer is thickest in the summer and does not show an obvious dependence on solar activity.

# Chapter 4

## Validation work for Swarm Langmuir probes

This chapter is devoted to validation of the Swarm Langmuir probe instruments.

### 4.1 Introduction

Although every instrument requires validation, whether it is ground-based or space-based, Swarm LP measurements are of special interest. The importance of these measurements is explained below.

In recent years, significant attention has been paid to the development of the empirical models of the electron density  $N_e$  distribution in the Earth's ionosphere (e.g., Feng et al., 2019; Karpachev et al., 2016; Klimenko et al., 2019; Radicella & Nava, 2020; Wang et al., 2019). There are practical needs behind these models (e.g., Belehaki et al., 2015), but there is also a general interest in understanding physical processes behind the plasma creation and its redistribution following strong solar-activity events and slow changes occurring as the solar cycle progresses (e.g., Kutiev et al., 2013; Laštovička, 2017; Schunk & Nagy, 2009). Efforts to improve the International Reference Ionosphere family of comprehensive global-scale ionospheric models (Bilitza et al., 2017; Bilitza, 2018; Kotova et al., 2018) and to develop models for specific ionospheric regions (e.g., Karpachev et al., 2016) have been recently shown. New comprehensive models have also been proposed, for example the E-CHAIM, Themens et al. (2017, 2019a).

One of the most difficult parts of the ionosphere to study is its topside, above the peak of the electron density. Experimentally, one can study the topside ionosphere with ground-based incoherent scatter radars (e.g., Beynon & Williams, 1978; Hunsucker, 1991). Unfortunately, these radars operate for limited times and cover only the space near their zenith. Measurements from ionosondes on satellites provided global coverage for many years, but this type of measurement is limited, and significant data sets have not been accumulated. Original topside sounding data analyses (e.g., Nava et al., 2001) have transitioned to studies with in situ measurements with

Langmuir probes (e.g., Belehaki et al., 2022; Kakinami et al., 2008; Kotova et al., 2022; Pignalberi et al., 2018). In recent years, radio occultation (RO) measurements of the topside have also become common (e.g., Hocke & Igarashi, 2002; Pignalberi et al., 2020). Measurements of Global Positioning System (GPS) signals from satellites on the ground also provide useful information on the electron density in the ionosphere, albeit indirectly for the topside (e.g., Themens et al., 2021).

Electron density profiles above the F region peak are of special interest for all empirical models. As mentioned, this region is difficult to investigate experimentally. It is not a surprise that several analytical and numerical approaches have been developed, and semi-empirical models were proposed (e.g., Coïsson et al., 2006; Kutiev et al., 2006; Radicella & Nava, 2020). One important step in this area is the development of the NeQuick semi-empirical model (Kotova et al., 2018; Nava et al., 2008; Pignalberi et al., 2018; 2020) that became a part of the IRI model (Bilitza, 2018). One can check the performance of various models of the topside ionosphere with in situ measurements on satellites. One venue in this respect is work with data from the Swarm satellites.

Three Swarm satellites have been in operation since 2013 (Buchert et al., 2015; Friis-Christensen et al., 2008; Knudsen et al., 2017). The Swarm satellites fly at altitudes of 400 to 500 km, and measure the electron density with a temporal resolution of one second or better (Buchert et al., 2015), i.e. with a spatial resolution of less than 10 km. Langmuir probes are one of many instruments on these satellite. The electron density can also be inferred from the Thermal Ion Imager (TII) instrument (Knudsen et al., 2017). Data from the TII have only just started to be explored (Xiong et al., 2022).

The LP method of electron density measurements is well established, but each Swarm unit requires validation. Several recent publications (Larson et al., 2021; Lomidze et al., 2018; Smirnov et al., 2021; Xiong et al., 2022) addressed this aspect of Swarm experimentation with LPs. It was found that overall, the Swarm LPs report electron density ( $N_e^{Swarm}$ ) values compatible with those measured on the ground and in space, although there is a tendency for LPs to underestimate the electron density by up to 30%. Data recalibration approaches have been suggested to deal with this underestimation effect.

The Swarm validation work has been more extensive for the middle and low latitudes, and limited for the high latitudes. Lomidze et al. (2018) and Smirnov et al. (2021) presented data for high latitudes obtained with the RO method. Although their results are in line with those reported

for the middle and low latitudes, there is a general concern about the quality of RO electron density measurements at high latitudes (Shaikh et al., 2018). This is because the method assumes that the ionosphere is spherically layered, which is not always true at high latitudes. Larson et al. (2021) focused on Swarm validation at extreme high latitudes, in the polar cap, by comparing their data with measurements from the RISR radars operating at Resolute Bay, Canada. The authors considered radar-satellite conjunctions with very close spatial coincidence. For this reason, their data set was limited. Performance of the Swarm LPs at the auroral zone latitudes has not been discussed although some data for these latitudes have been presented (e.g., Lomidze et al., 2018; Smirnov et al., 2021).

The aim of the work presented in this chapter is to compare ISR-Swarm electron density measurements at the auroral zone and polar cap latitudes, thus expanding the previous ISR-Swarm comparison by Larson et al. (2021) in the polar cap. In essence, this chapter is a contribution to the validation work for Langmuir probes on the Swarm satellites performed by other researchers (Larson et al., 2021; Lomidze et al., 2018; Smirnov et al., 2021; Xiong et al., 2022). Most of the materials presented here are part of a published paper:

Fast, H., A. Koustov, & R. Gillies, 2023. Validation of Swarm Langmuir probes by incoherent scatter radars at high latitudes. *Remote Sensing*, 15, 1846. <https://doi.org/10.3390/rs15071846>

My contributions to the above publication are as follows:

1. Development of the software for
  - Identification of Swarm satellite passes over Resolute Bay and Poker Flat
  - Reading and averaging ISR data in multiple beams
  - Analysis of the electron density profiles
  - Combing and comparing electron density data from ISRs and Swarm
2. Full statistical analyses of the radar-satellite data under supervision of Dr. Koustov
3. Production of all original diagrams apart from Figure 4.1.
4. Participation in writing of the manuscript and work on the reviewers' comments

## 4.2 Methodology of the analysis

In this chapter, incoherent scatter radars were selected as an independent instrument for testing the Swarm LP performance.

## 4.2.1 Geometry and approach

Locations for the PFISR and RISR-C radars and examples of the Swarm footprints for two passes over the radars' field of views are shown in Figure 4.1.

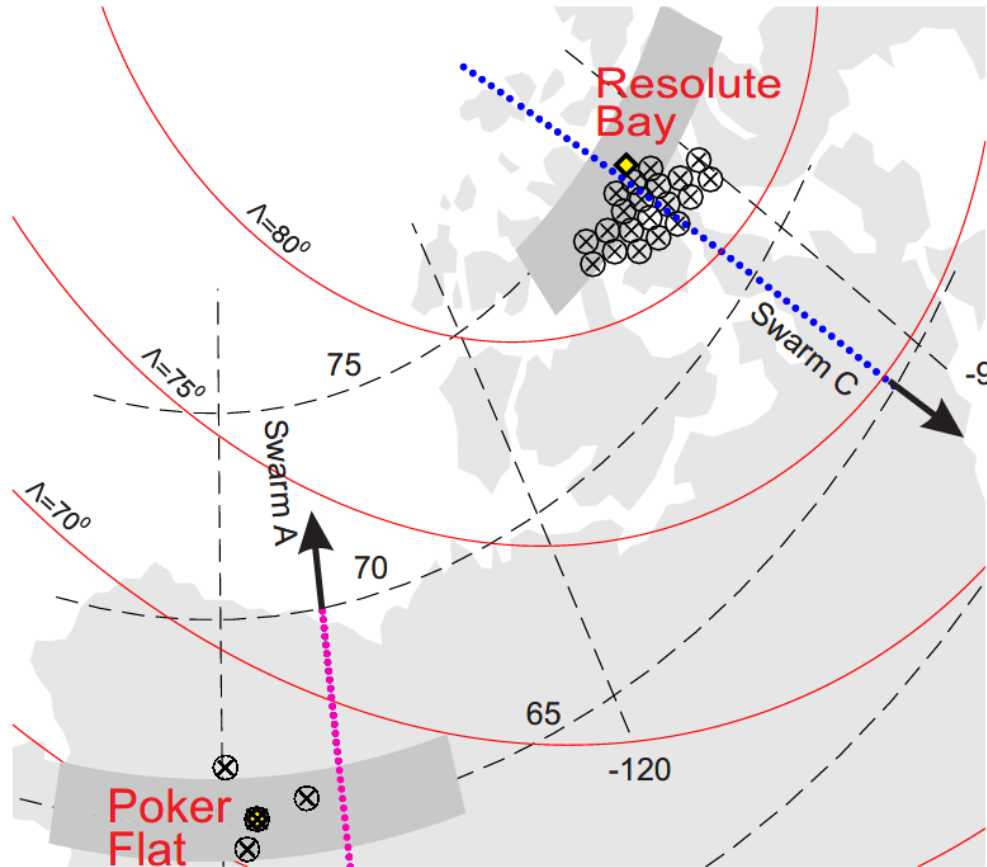


**Figure 4.1:** A map illustrating typical measurement coverage by RISR-C (Resolute Bay) and PFISR (Poker Flat), and the footprints of the Swarm satellites passing the area of ISR measurements in two different events. For the ISRs, an altitude of  $\sim 450$  km was considered. Crosses indicate those locations for which a median electron density was computed and compared to Swarm data. Darker shaded segments around Resolute Bay and Poker Flat outline the areas over which the median Swarm data was computed along a trajectory. Shown by solid dots are Swarm C footprints for 27 July 2016 ( $\sim 16:35$  UT, blue) and Swarm A footprints for 21 February 2015 ( $\sim 07:23$  UT, pink). Arrows indicate directions of satellite travel.

For RISR-C, the radar location is indicated by a yellow diamond. Measurements are made somewhat equatorward of its location. Pierce points at 450 km for 21 beams are shown in Figure 4.1 by circled crosses. For any of the selected beams (out of the total available 51) the elevation angles are above  $55^\circ$ , and all other beams were judged to be too far away from the radar location. Originally, there were plans to conduct a similar work with the RISR-N radar, but because the

results obtained for the RISR-C radar were consistent and compatible with those from the previous comparison by Larson et al. (2021), this work is left for the future. Figure 4.1 shows footprints for two Swarm satellite passes, one over each of the ISR regions of comparison. Conjunctions occurring while the satellites were travelling either equatorward (as shown over Resolute Bay) or poleward (as shown over Poker Flat) were considered. Figure 4.2 gives details of the methodology for handling data from both instruments.

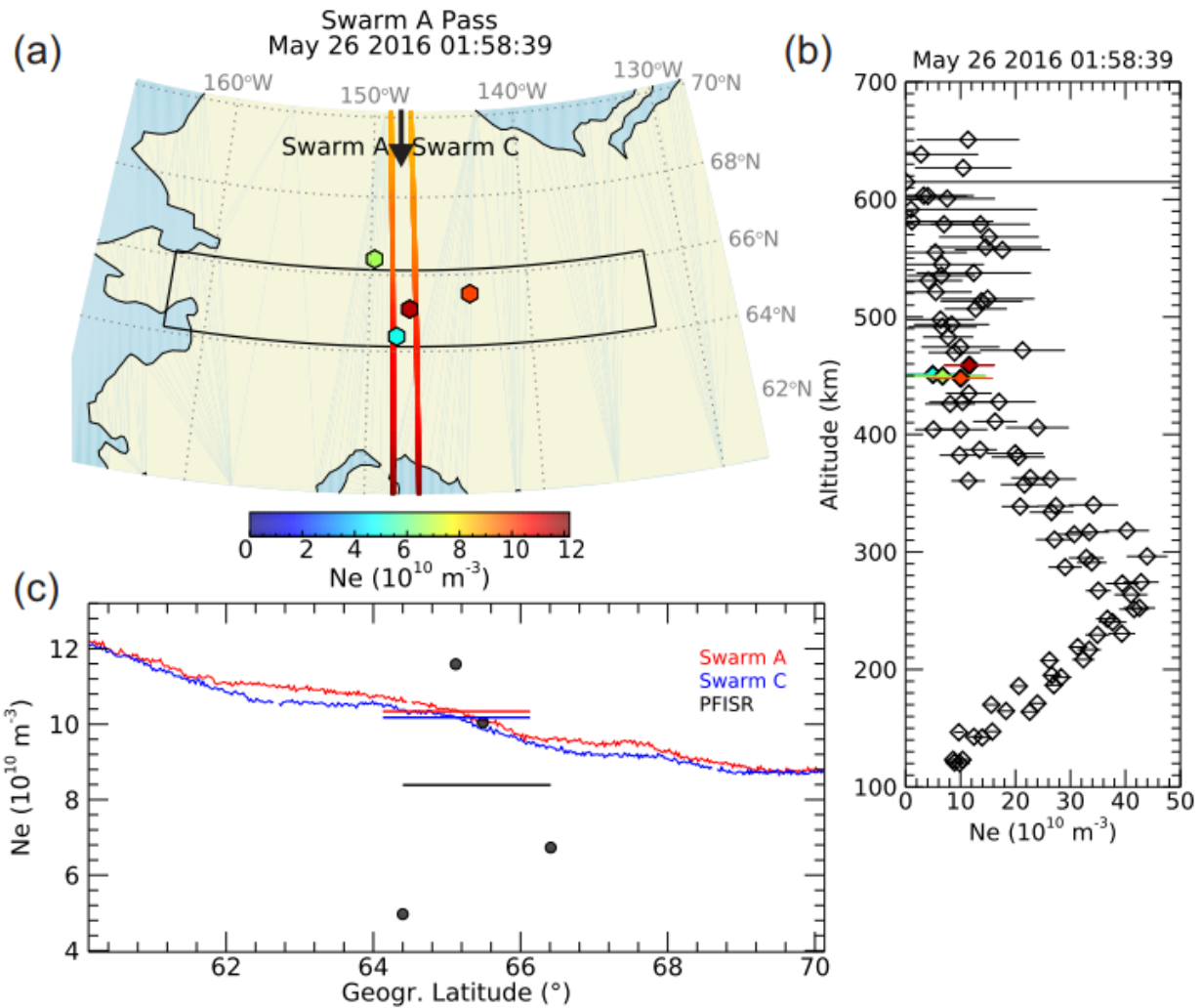


**Figure 4.2:** Details on methodology of ISR-Swarm comparison for the Poker Flat (PFISR) radar. (a) Footprints of the Swarm A and Swarm C satellites passing the area of PFISR observations on 26 May 2014 at ~01:58 UT moving equatorward (arrow). The observed electron density is represented by the color according to the bar at the bottom of the panel. For PFISR, an altitude of 450 km was considered. Colored segments reflect the median electron density according to the color bar at the bottom. (b) Electron density profile according to PFISR measurements. Colored diamonds indicate measurements for the conjunction. (c) Line plot of the electron density measured by the instruments and median values passed to the data base.

The median of the Swarm electron density values along their track were taken from points of measurements within  $\pm 1^\circ$  geographic latitude (GLAT) of the ISR radar location, corresponding to  $\sim 200$  km in latitude. Longitudinally, a Swarm separation from the radar sites of up to  $15^\circ$  was allowed. The spatial regions where Swarm measurements were classified as a conjunction with ISRs are shown by darker shading in Figure 4.1 for both PFISR and RISR-C and by a rectangle in Figure 4.2. Swarm data were considered if a satellite was within the allowable area for comparison (rectangle in Figure 4.2) any time within a 5-min interval of an ISR measurement. 5-min integrated data were considered for both PFISR and RISR-C.

Figure 4.2c shows that Swarm A and Swarm C show comparable electron densities as the red and blue overlap in a significant part of the pass. The median of the electron densities within the conjunction area are presented by horizontal lines to judge the difference between the PFISR measurement and Swarm measurements. The difference is  $\sim 2 \cdot 10^{10} \text{ m}^{-3}$  for this event. Larson (2021, personal communication) made a statistical analysis of differences between the Swarm A and Swarm C LP measurements over Resolute Bay and concluded that they are on the order of  $1 \cdot 10^{10} \text{ m}^{-3}$  to  $5 \cdot 10^{10} \text{ m}^{-3}$ . The temporal separation between the two satellites is on the order of 10 s. Since the differences between measurements from the two satellites were often large, the data from Swarm A and Swarm C were treated as separate points for comparison with the ISRs.

From Figure 4.1, the median of the electron density profiles measured by 21 RISR-C beams was taken to obtain an electron density height profile characterizing a large spatial domain, similar to the PFISR data handling. For PFISR, four pierce points at 450 km are shown by circled crosses and the middle point corresponds to the radar location. The median of the PFISR electron density profiles was taken over all 4 beams. All measurements were considered irrespective of error values, and the uncertainty of measurements at each height was characterized by the standard deviation of electron density in the beams.

This approach of ISR-Swarm data handling for conjunctions is similar to the approach used by others (e.g., Lomidze et al., 2018; Smirnov et al., 2021, Xiong et al., 2022), but it differs from the approach used by Larson et al. (2021) who considered 5-min data in World Day mode and quasi-instantaneous Swarm measurements.

One disadvantage of the approach by Larson et al. (2021) was that the ISR data at the conjunction height were often missing or of a poor quality for some beams but reasonable in other

beams. The approach of the present study alleviates this problem. Another advantage of the present approach is in diminishing the effect of extreme localized electron density enhancements that frequently occur at high latitudes. In the polar cap, near RISR-C, these enhancements are polar cap patches while in the auroral (subauroral) zone, near PFISR, these enhancements can be related to patches or intense particle precipitation (Crowley et al., 2000).

#### 4.2.2 Data coverage

Figure 4.3 provides information on data coverage for three comparisons, PFISR with Swarm A and Swarm C, PFISR with Swarm B, and RISR-C with Swarm A and Swarm C. These three comparisons will be referred to as PFISR-AC, PFISR-B and RISR-AC comparisons, respectively.

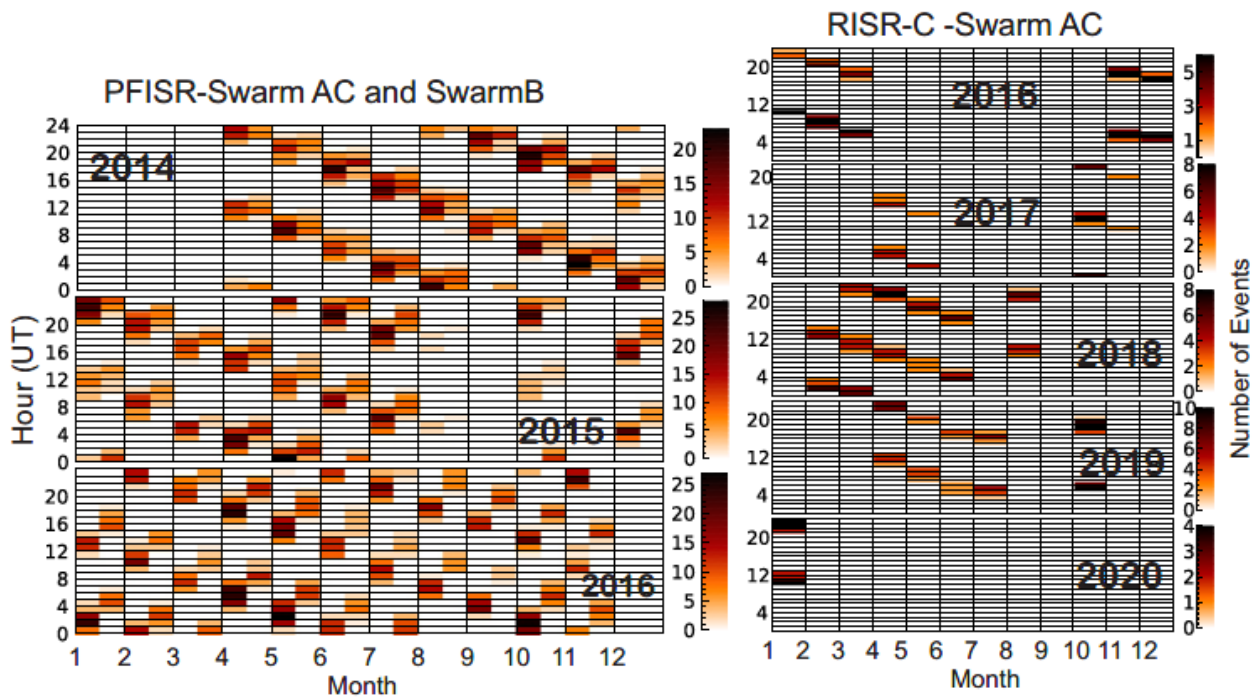


**Figure 4.3:** Number of joint ISR-Swarm measurements on the UT-month plane for observations over Poker Flat, left panels, and Resolute Bay (RISR-C radar), right panels. For the Poker Flat data, each UT-month cell is divided into two halves with the left half for each month corresponding to the radar-Swarm AC conjunctions while the right half of each month corresponding to the radar-Swarm B conjunctions.

A RISR-C comparison with Swarm B was not performed because of difficulties in getting reasonable data coverage as RISR-C electron density profiles at or above 510 km are very noisy.

In addition, the PFISR-B comparison showed results consistent with the pervious study by Larson et al. (2021).

Figure 4.3 shows that for the PFISR-AC comparison all months and UT sectors are covered, cumulatively over 2.5 years, albeit not very uniformly with some very limited gaps in the data. The number of PFISR-B conjunctions is  $\sim 2$  times smaller than the number of PFISR-AC conjunctions because the PRISR-AC comparison data set is a combination of measurements from both satellites. The RISR-AC comparison shows far less conjunctions than both PFISR comparisons, particularly in the winter, despite more years of data being considered. The total number of conjunctions is  $\sim 2600$  for PFISR-AC,  $\sim 1300$  for PFISR-B, and 421 for RISR-AC.

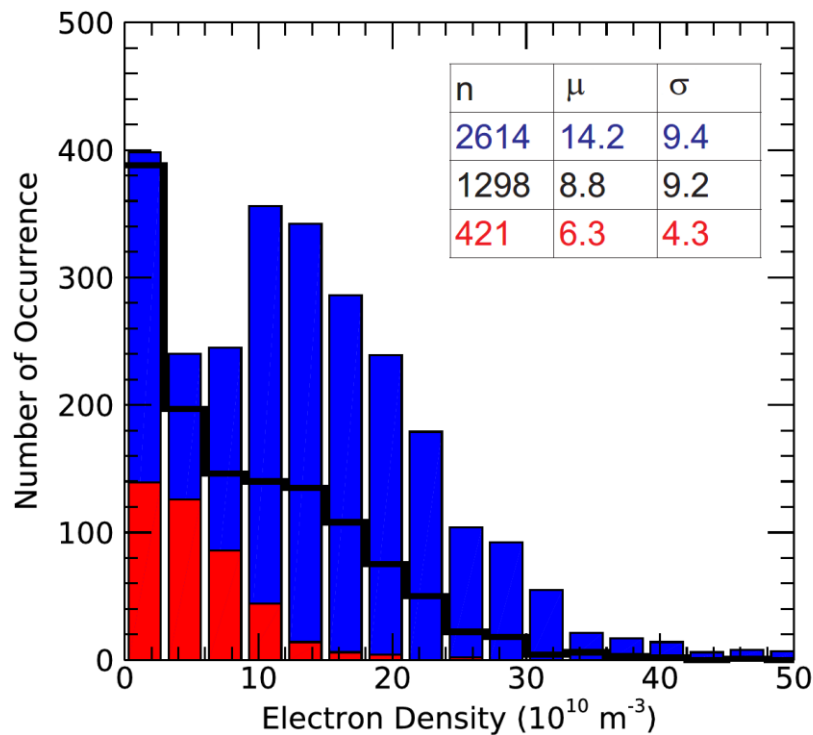


**Figure 4.4:** Histogram distributions for the occurrence of the electron density measured by the incoherent scatter radars PFISR and RISR-C for all conjunctions with Swarm satellites in 2014 to 2020. Blue columns are for the PFISR-Swarm AC conjunctions, red columns are for the RISR-C-Swarm AC conjunctions and black columns are for the PFISR-Swarm B conjunctions. The ISR electron density is plotted in units of  $10^{10} \text{ m}^{-3}$ . Total number of points  $n$ , median value  $\mu$  (in units of  $10^{10} \text{ m}^{-3}$ ) and standard deviation  $\sigma$  (in units of  $10^{10} \text{ m}^{-3}$ ) for each distribution are given in the upper right corner by numbers colored respectively.

Figure 4.4 gives a sense of typical electron densities available for the obtained database in the form of cumulative histograms. The blue columns indicate that the PFISR-AC comparison has far more points of electron density measured by PFISR ( $N_e^{PFISR}$ ) between 0 and  $15 \cdot 10^{10} \text{ m}^{-3}$ , and a

gradual decrease in points at larger electron densities. For the PFISR-B and RISR-AC comparisons, low electron density data are more dominant. The median values of the electron density are  $14.2 \cdot 10^{10} \text{ m}^{-3}$ ,  $8.8 \cdot 10^{10} \text{ m}^{-3}$  and  $6.3 \cdot 10^{10} \text{ m}^{-3}$  for the PFISR-AC, PFISR-B, and RISR-AC comparisons, respectively. These numbers reflect changes in electron density with altitude (PFISR-AC versus PFISR-B) and latitude (PFISR-AC versus RISR-AC).

### 4.2.3 Variability of Swarm and ISR electron densities over conjunction regions

Ideally, for a comparison of ISR and Swarm electron density measurements, one would want to have small differences between values measured by the ISR radars in many beams (4 for PFISR) over several minutes, and small spatial variations of electron density measured by the Swarm satellites along their trajectories over a conjunction area to justify taking the median value of these measurements. In reality, variations usually occur, as shown in Figure 4.2. To assess the variability of the electron density values for conjunctions, the standard deviations of the measurements were computed for each instrument and were then compared with each other, Figure 4.5. In Figure 4.5a, data for both Swarm A and Swarm C were included keeping in mind that typically individual measurements on two satellites were compared with the same electron density value measured by PFISR, because of the 5-min intervals in the data available. Figure 4.5b is the comparison in the standard deviation in measurements for PFISR and Swarm-B.

Figures 4.5a and 4.5b show that the most frequently occurring differences between the standard deviation of the measurements between the instruments is on the order of  $2 \cdot 10^{10} \text{ m}^{-3}$  to  $4 \cdot 10^{10} \text{ m}^{-3}$  for the Swarm AC satellites and  $2 \cdot 10^{10} \text{ m}^{-3}$  to  $3 \cdot 10^{10} \text{ m}^{-3}$  for the Swarm B satellite. Another general conclusion is that the variability in the PFISR values is larger than the variability in the Swarm values.

To explore the uncertainty in the measurements further, the standard deviations of the electron density measured by PFISR and the standard deviation of the electron density measured by Swarm AC are plotted against the absolute values of the electron density measured by PFISR, Figures 4.5c and 4.5d, respectively. As expected, the standard deviation tends to increase with the electron density measured by PFISR. The effect is clearly seen in Figure 4.5c for the PFISR data.

For the Swarm AC data, shown by Figure 4.5d, the standard deviation is  $\sim 2 \cdot 10^{10} \text{ m}^{-3}$  and is fairly constant with increasing electron density, with the exception of very large electron densities.

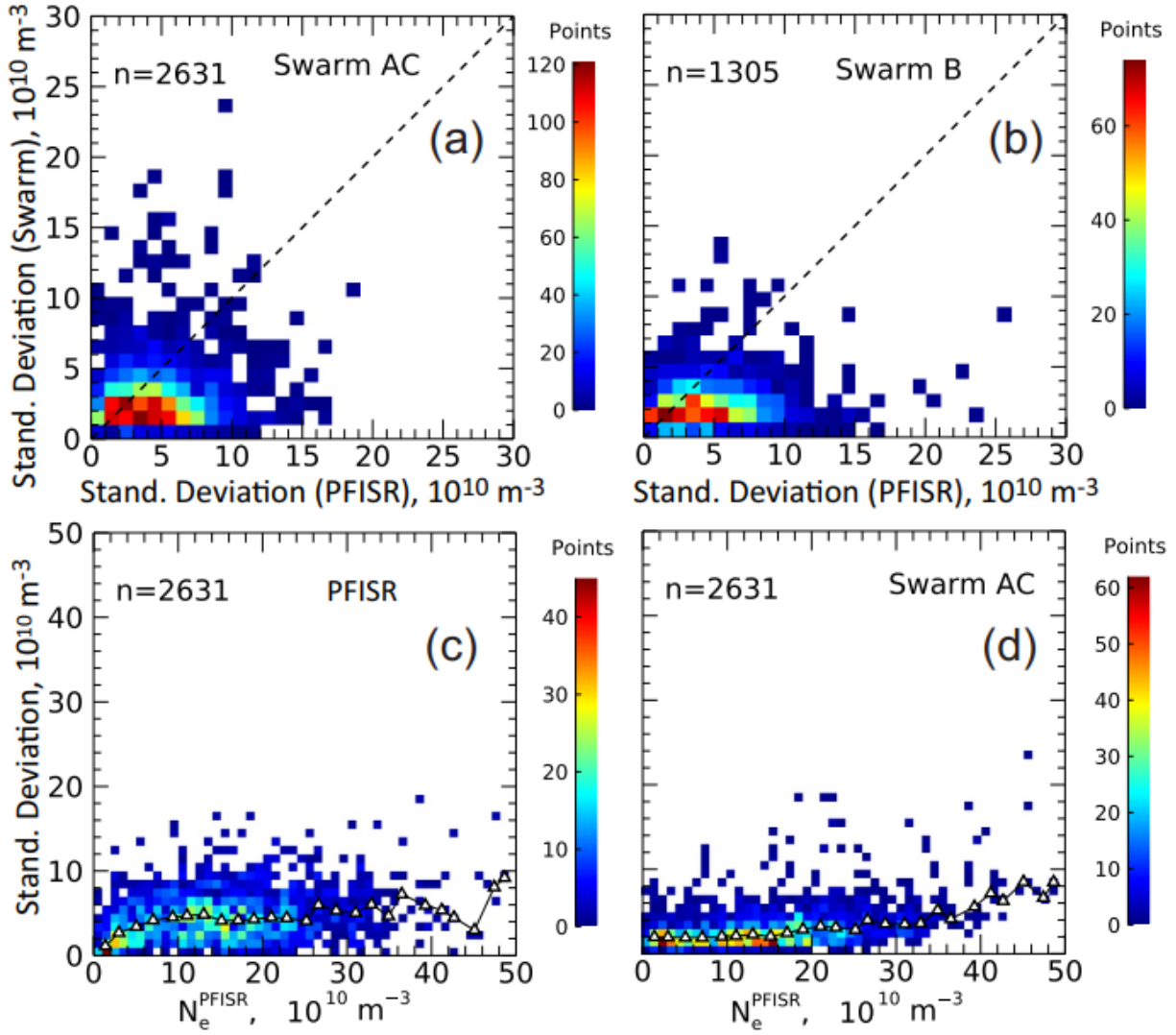


**Figure 4.5:** (a) Standard deviations of electron density for Swarm measurements versus standard deviation of electron density for PFISR measurements over respective areas of conjunctions for the PFISR-AC comparison. (b) The same as (a) but for PFISR-B comparison. (c) Standard deviations of electron density for PFISR measurements versus the absolute value of the electron density measured by PFISR. The triangles are the medians of standard deviations in  $N_e^{\text{PFISR}}$  bins of  $2 \cdot 10^{10} \text{ m}^{-3}$  (d) The same as (c) but for standard deviations of Swarm AC measurements.

The Swarm LP data do not have uncertainty estimates for individual measurements, so the standard deviations reported in Figure 4.5 can be considered as error estimates for these instruments. For PFISR, uncertainty in each measurement is provided by the radar operators. These

reported uncertainty values have a large degree of variability, specifically at the ionospheric topside. This is expected to occur due to the echo power variations affecting the quality of autocorrelation lags in raw data analysis (Chapter 2). However, the reported values are typically below or at the level of what is reported in Figure 4.5c.

## 4.3 RISR and Swarm comparison, results for the polar cap

In this section, joint ISR-Swarm data for observations near Resolute Bay, Canada are considered using measurements from the RISR-C radar and from the Swarm A and Swarm C satellites.

### 4.3.1 Overall scatter plots

The first objective in assessing Swarm data against ISR measurements is to investigate if the new approach of considering median data (in the present work) is comparable with the results obtained by Larson et al. (2021), who compared quasi-instantaneous electron density values at close locations. Figure 4.6 presents data for the RISR-AC conjunctions in the form of a scatter plot. The points are scattered around the bisector of perfect agreement (blue line) with a trend of smaller  $N_e^{Swarm}$  values at larger  $N_e^{RISR}$  values. The tendency is obvious while looking at the red dots, representing the medians of  $N_e^{Swarm}$  in bins of  $N_e^{RISR}$ . The linear fit to the data, depicted by the green line, is somewhat different from the dashed line representing the linear fit line to a similar plot reported by Larson et al. (2021), their Figure 6. The slope of the line in Figure 4.6 indicates that, typically, the ratio is  $\sim 0.57$  which is close to the values of 0.58 to 0.59 reported by Larson et al. (2021). This consistency implies that the comparisons by the two methods are compatible.

The data shown in Figure 4.6 have one common feature with the previous work, namely, the presence of cases of Swarm overestimations (shown by the darker colored points) at small  $N_e^{RISR}$  values. The Swarm overestimations in Figure 4.6 seem to be less significant in our case if one judges by the y-intercept of the fit line. It is close to 0 in Figure 4.6 compared to a value of  $\sim 4 \cdot 10^{10} \text{ m}^{-3}$  reported by Larson et al. (2021). However, the number of cases with Swarm overestimation is larger here,  $\sim 24\%$  of all points compared to  $\sim 12\%$  seen in the data reported by Larson et al. (2021), their Figure 5. We note that the total number of conjunctions in the present work is about half of those in Larson et al. (2021), but the number of separate satellite crosses is  $\sim 4$  times larger.

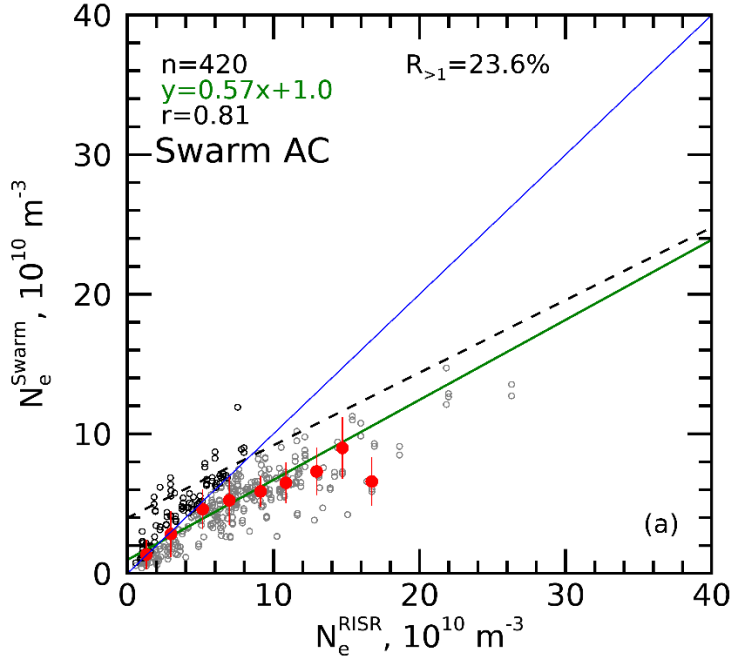


**Figure 4.6:** Scatter plot of the electron density measured by the Swarm A and Swarm C satellites  $N_e^{Swarm}$  versus electron density measured by the Resolute Bay incoherent scatter radar RISR-C  $N_e^{RISR}$ . Darker circles reflect measurements where  $N_e^{Swarm}/N_e^{RISR} > 1$ . Red solid dots are medians of  $N_e^{Swarm}$  in bins of  $N_e^{RISR}$  (size of each bin is  $2 \cdot 10^{10} \text{ m}^{-3}$ ). Vertical red bars are the binned values of  $N_e^{Swarm} \pm$  one standard deviation of  $N_e^{Swarm}$ . The green line is a linear fit line assuming that the RISR-C measurements are precise. The dashed line is a linear fit line according to the data presented by Larson et al. (2021).

### 4.3.2 Diurnal differences between $N_e^{Swarm}$ and $N_e^{RISR}$

A more extensive data set considered in the current work as compared to that in Larson et al. (2021) allows us to assess a change in the degree of Swarm-radar agreement over different periods of the day. The entire RISR-AC data set was split on four time sectors as follows: dawn (10 to 16 UT), day (16 to 22 UT), dusk (22 to 04 UT) and night (04 to 10 UT). Figure 4.7 shows scatter plots of RISR-AC electron density measurements in the four different time sectors. The format of the plots is the same as that in Figure 4.6.

Figure 4.7 indicates that agreement is best at nighttime and worst at daytime. These conclusions can be made from both the slopes of the linear fit line and from simply assessing the locations of the red dots (median values of  $N_e^{Swarm}$ ) with respect to the bisector of perfect agreement (blue line). Figure 4.7 also indicates that  $N_e^{Swarm}$  underestimations and overestimations are both possible for all time sectors. Nighttime shows highest percentage of Swarm overestimations. We

note that the correlation coefficients  $r$  are not very high,  $\sim 0.75$ , indicating significant spread of the points on the plots.

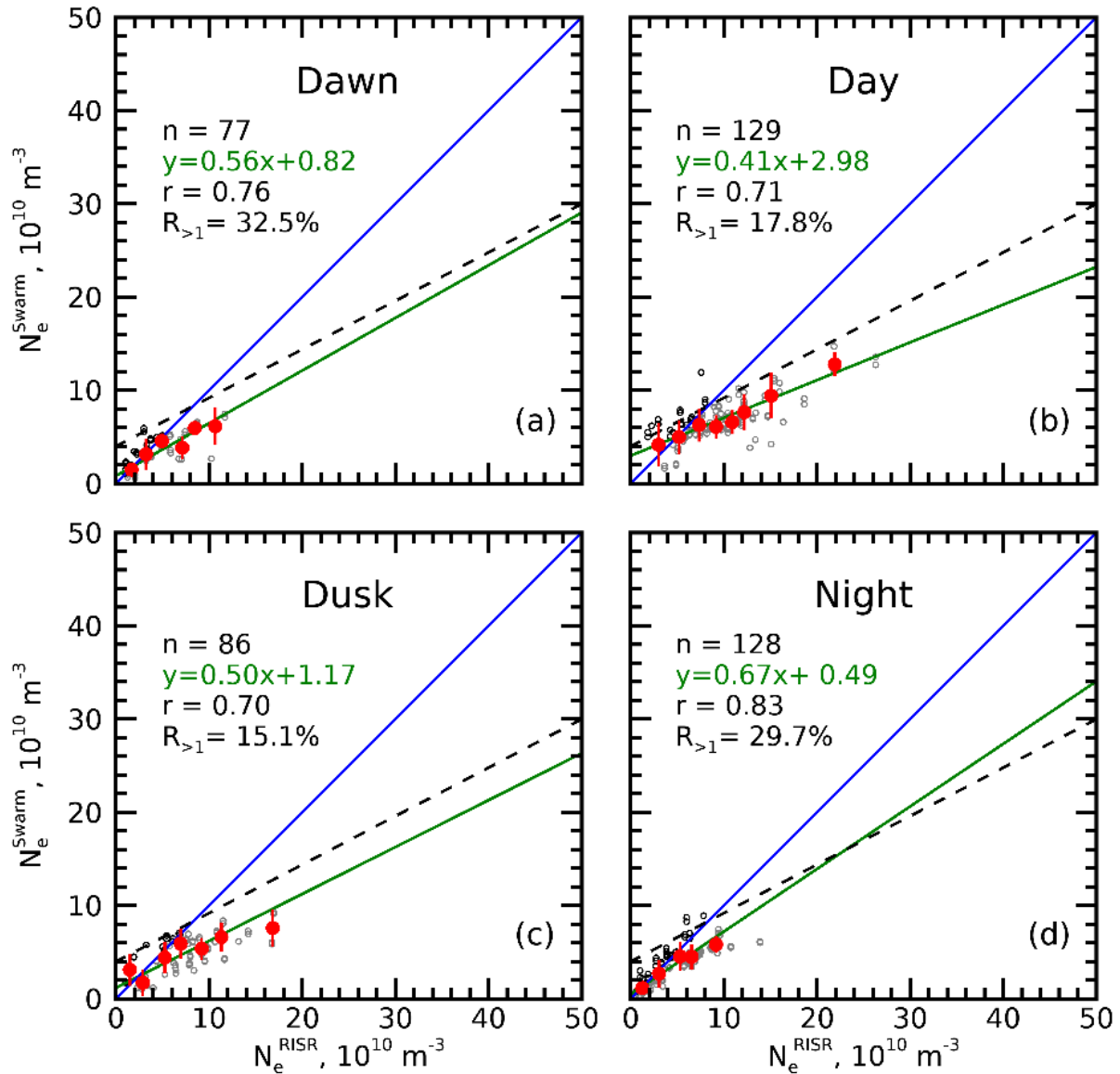


**Figure 4.7:** Scatter plots of electron density measured onboard the Swarm A and Swarm C satellites versus electron density measured by the RISR-C incoherent scatter radar. The format of the plots is the same as in Figure 4.6. Panels (a) through (d) are for the dawn, day, dusk, and night sectors. Definitions of the time sectors are given in the text.

The conclusions on the level of RISR-AC agreement for the four time sectors are different than what was reported by Larson et al. (2021). They indicated that the agreement is the worst in the night sector. Their conclusion was based on a more limited data set containing data for Swarm

A, Swarm C, and Swarm B measurements. The authors judged the differences in agreement by looking at the median ratios  $N_e^{Swarm}/N_e^{RISR}$  and the differences in median ratios for various time sectors were rather minor (see their Table 2). Moreover, as will be shown later in this chapter, the Swarm B-ISR comparison shows somewhat different trends compared to the Swarm AC-ISR comparison. Based on this finding, merging of Swarm data at two different heights (Swarm A and Swarm C at 450 km, and Swarm B at 510 km) to create a larger data set may not be the best approach.

## 4.4 PFISR and Swarm comparison, results for the auroral zone

In this section, joint ISR-Swarm data for observations near Poker Flat, Alaska are considered using measurements from the PFISR radar and from the Swarm A, Swarm C, and Swarm B satellites.

### 4.4.1 Overall scatter plots

Figure 4.8 presents scatter plots of the PFISR-AC and PFISR-B electron density data in the same format as the RISR-AC comparison in Figure 4.6. The number of available points is ~6 times larger for the PFISR-AC comparison and ~3 times larger for the PFISR-B comparison. General tendencies here are the same as in Figure 4.6 and are similar to the plots reported by Larson et al. (2021). The linear fit line for the PFISR-AC comparison agrees well with the fit line reported by Larson et al. (2021). The number of Swarm overestimation cases is significantly larger for the PFISR-B data, 37% versus 24% for the PFISR-AC case.

Figure 4.8 indicates that the majority of the data are located below the bisector of perfect agreement (indicated by the grey points). The effect is obvious at large electron densities. At small electron densities, there is significant number of points located above the bisector (indicated by the black points). These are cases of  $N_e^{Swarm}$  overestimations. The number of such points is comparable to that reported for the polar cap area in Figure 4.6. The slope of the linear fit line is lower in this comparison, 0.52 versus 0.57, which could be due to the greater amount of higher electron density data measured by the PFISR radar.

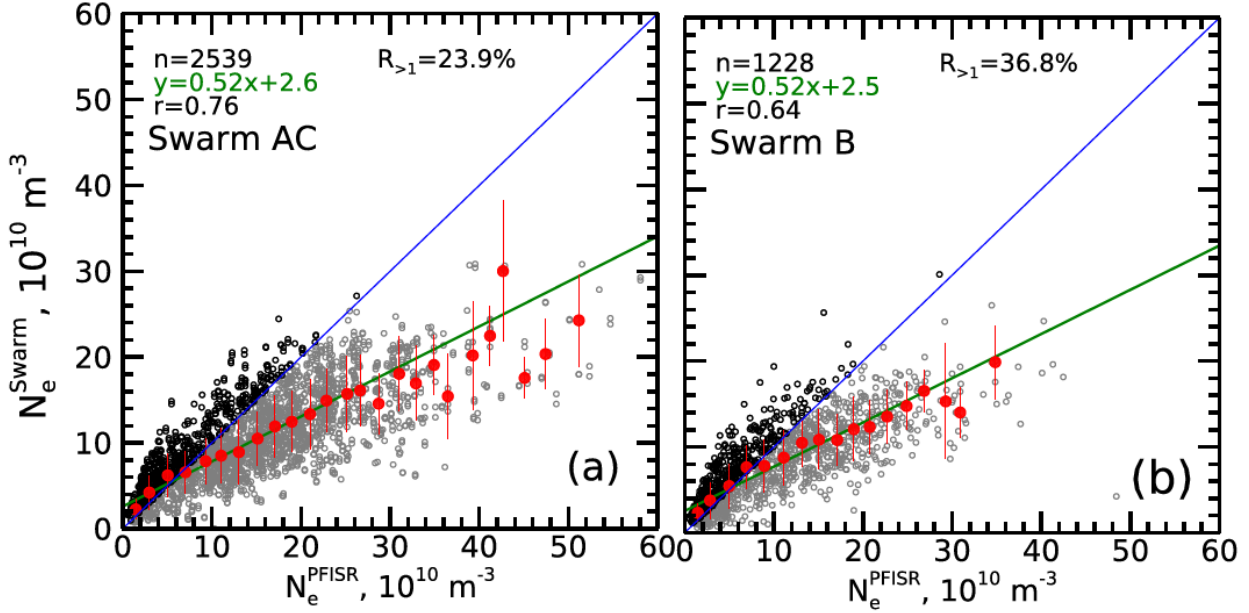


**Figure 4.8:** Scatter plots of the electron density measured onboard the Swarm satellites versus electron density measured by the PFISR incoherent scatter radar. The format of the plots is the same as in Figure 4.6. Panels (a) and (b) are for the PFISR-AC and PFISR-B conjunctions, respectively.

#### 4.4.2 Diurnal differences between $N_e^{Swarm}$ and $N_e^{PFISR}$

An assessment of the differences in PFISR-Swarm agreement was performed considering the same approach as for RISR-AC comparison in Section 4.3. The four different time sectors were selected as follows: dawn (14 to 20 UT), day (20 to 02 UT), dusk (02 to 08 UT) and night (08 to 14 UT).

The PFISR-AC data, shown in figure 4.9, and the PFISR-B data, shown in figure 4.10, are fairly consistent with each other. The slopes of the linear fit lines are in the range of 0.5 to 0.7 and y-offsets in the range of  $1 \cdot 10^{10} \text{ m}^{-3}$  to  $4 \cdot 10^{10} \text{ m}^{-3}$ . The agreement between the PFISR and Swarm measurements is better for the nighttime. The Swarm overestimations are more obvious at small electron densities. Nighttime shows the most frequently occurring overestimates at  $\sim 39.4\%$  of the data for Swarm AC and  $48.2\%$  of the data for Swarm B. Overestimations are less frequent during the daytime for Swarm AC and Swarm B at  $15.6\%$  and  $27.1\%$ , respectively. Overall, Swarm B shows a higher percentage of overestimations for all four time sectors compared to Swarm AC. These results are also consistent with data from the RISR-AC comparison in Figure 4.7.

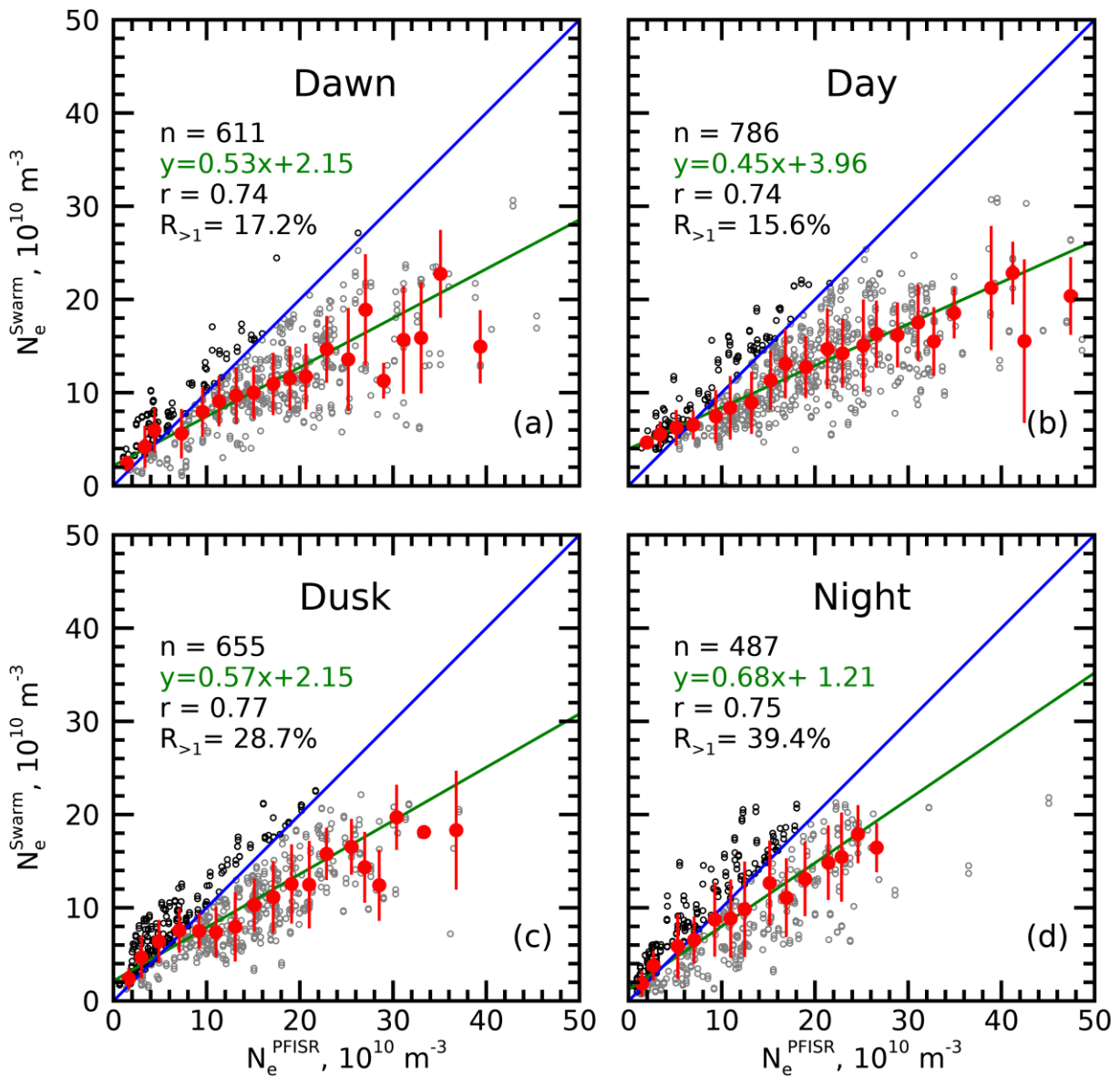


**Figure 4.9:** Scatter plots of electron density measured onboard the Swarm AC satellites versus electron density measured by the PFISR incoherent scatter radar. The format of the plots is the same as for Figure 4.6. Panels (a) through (d) are for the dawn, day, dusk, and night sectors, respectively. Definitions of the time sectors are given in the text.

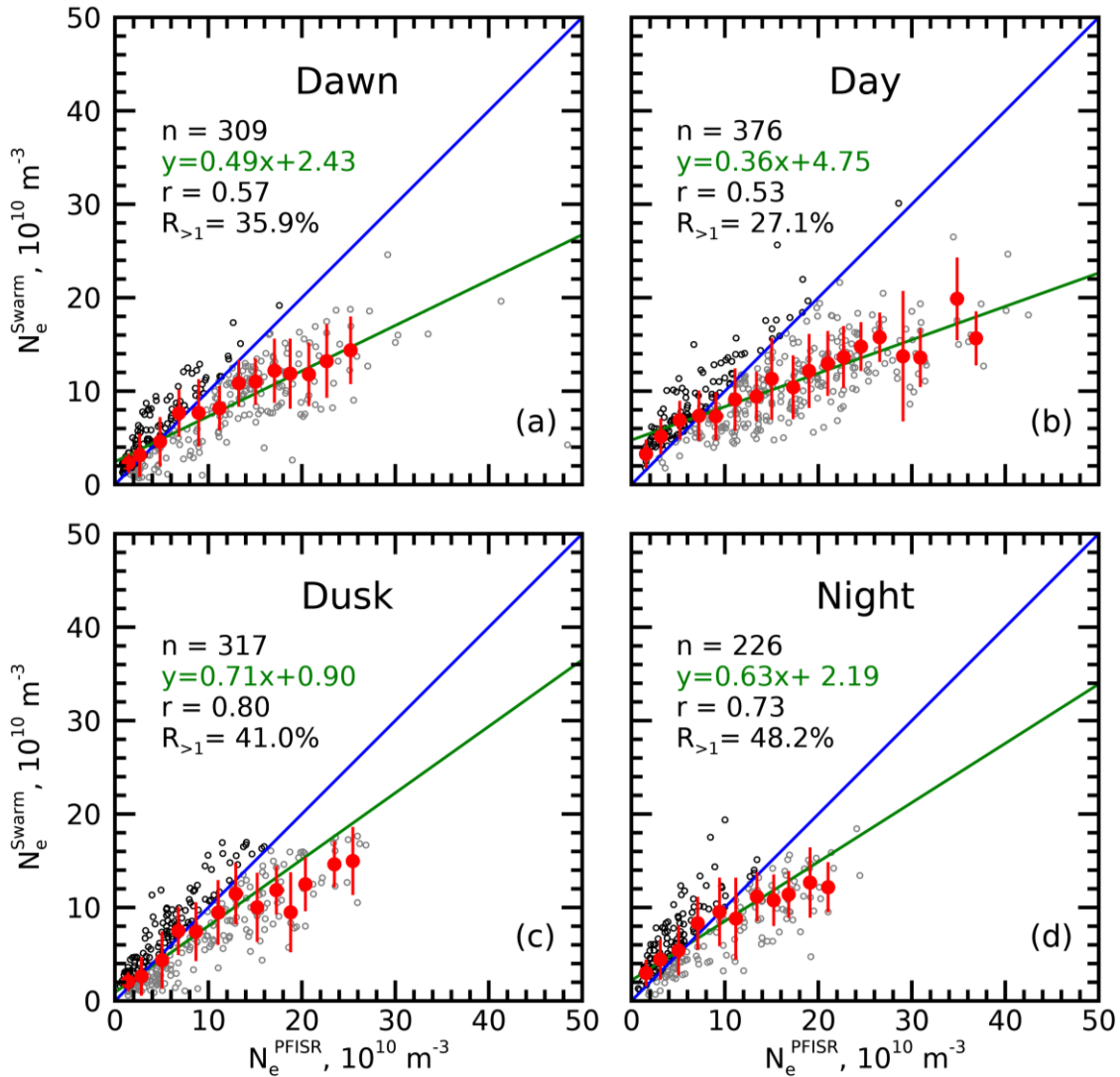


**Figure 4.10:** The same as in Figure 4.9 but for the PFISR-B conjunctions.

#### 4.4.3 Examining the ratio $N_e^{Swarm}/N_e^{PFISR}$ versus absolute electron density

To further investigate the overestimation effect, the ratio  $R = N_e^{Swarm}/N_e^{PFISR}$  is plotted versus  $N_e^{PFISR}$  binned in steps of  $2 \cdot 10^{10} \text{ m}^{-3}$ , Figure 4.11. The ratio  $R$  steadily increases toward smaller  $N_e^{PFISR}$ .  $R$  values are typically greater than 1 for  $N_e^{PFISR} < 5 \cdot 10^{10} \text{ m}^{-3}$  and become greater than 2 at  $N_e^{PFISR} < 3 \cdot 10^{10} \text{ m}^{-3}$ . The tendencies are very similar for the PFISR-AC and PFISR-B comparisons, implying that the effect does not strongly depend on the height of joint measurements. The comparisons performed suggest that the Swarm electron density

overestimation effect is a common feature of the Swarm LP instruments and is significant whenever electron densities in the ionosphere are low.

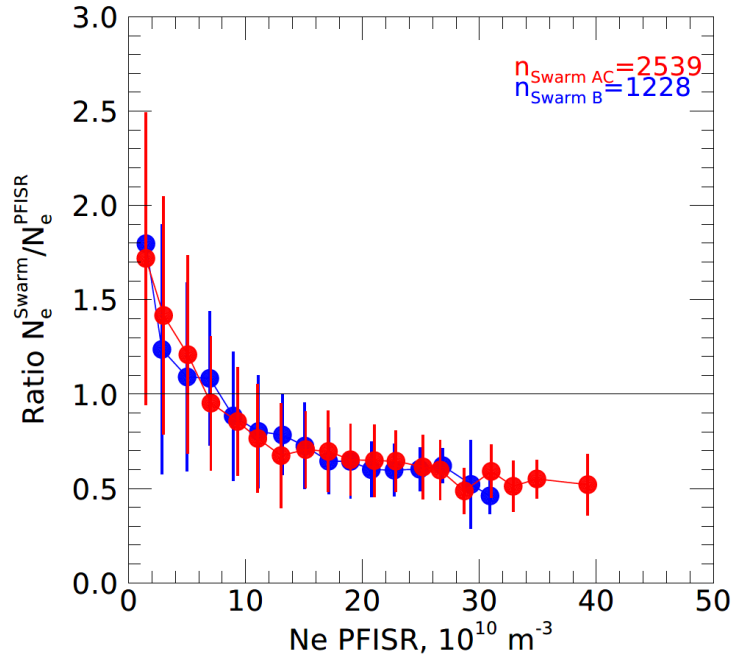


**Figure 4.11:** Medians of the ratio  $N_e^{Swarm}/N_e^{PFISR}$  as a function of the electron density measured by PFISR  $N_e^{PFISR}$ . The bins of  $N_e^{PFISR}$  have a step of  $2 \cdot 10^{10} \text{ m}^{-3}$ . Vertical bars for each bin are the median value of the ratio  $\pm$  one standard deviation of the ratio. Red and blue colors characterize data for PFISR conjunctions with Swarm AC and Swarm B, respectively.

#### 4.4.4 Solar cycle trend for the ratio R

Xiong et al. (2022) presented data indicating that the Swarm overestimation occurrence changes as the solar cycle progresses. The dataset presented here is too limited to explore the effect in great detail, but is sufficient to identify trends at the decaying phase of solar cycle 24.

Figure 4.12 is a contour plot for the number of cases of ratio  $R$  as a function of time between 2014 and 2017 with the red-pink color corresponding to largest counts. Overlaid on the contours is a black line (connecting white circles) representing monthly median values of F10.7-cm radio flux. The scale for the F10.7-cm flux is on the right Y axis.

A reduction of the F10.7-cm flux from  $\sim 120$  s.f.u. in 2014 to  $\sim 80$  s.f.u. by the end of 2016 is evident. The ratio  $R$  does not show an obvious trend with most of the cases being in between 0.3 and 0.8 for both Swarm AC and Swarm B. The distributions for  $R$  appear to become flatter at smaller solar activity, as the red-pink color becomes less present in 2016. This effect is more

obvious in the Swarm B data (Figure 4.12b). The other general observation from Figure 4.12 is that the Swarm B distributions tend to be somewhat shifted towards the horizontal line of  $R = 1$ .

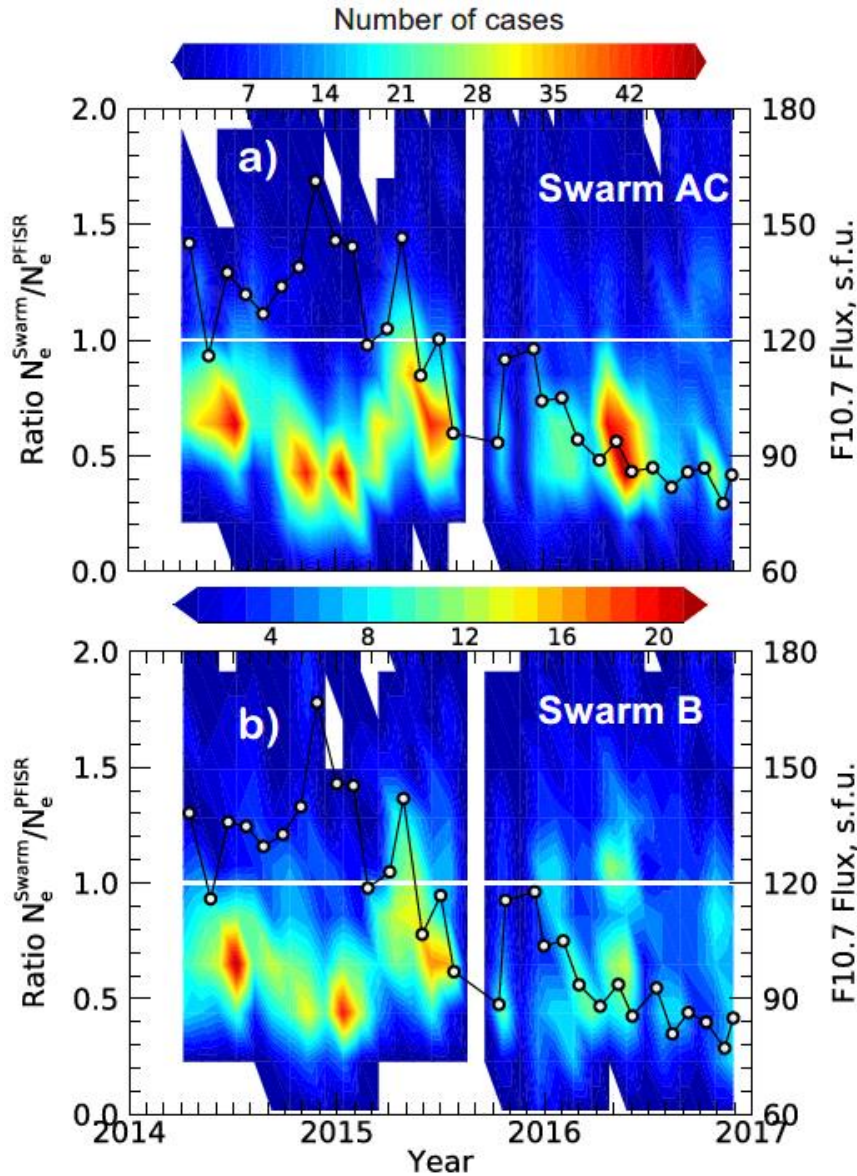


**Figure 4.12:** (a) A contour plot for the occurrence of the ratio  $R = N_e^{Swarm}/N_e^{PFISR}$  for Swarm AC versus year of radar-satellite conjunctions. The ratio is scaled according to the bar at the top of each plot. Black circles are F10.7-cm radio flux (given in s.f.u. units). The scale for the radio flux is given on the right. (b) The same as (a) but for Swarm B satellite.

Upon closer examination of the plots in Figure 4.12 it can be inferred that largest F10.7-cm values, occurring at the end of 2014 to beginning of 2015, correlate with occurrence of smallest  $R$  values. Also, a steady increase in F10.7-cm flux from the middle of 2014 to the beginning of 2015

correlates with a steady decrease of  $R$ , and short-lasting enhancement of F10.7-cm flux in the middle of 2015 is accompanied by a decrease of  $R$ . A short-lived enhancement of F10.7-cm flux at the beginning of 2016 is seen as a transition from a flat distribution of  $R$  values to more asymmetric distribution with domination of  $R$  equal to  $\sim 0.4$ .

To investigate the solar cycle effect more quantitatively, median  $R$  values are plotted versus F10.7-cm flux in bins of 20 s.f.u., shown by the solid dots in Figure 4.13. A decrease of  $R$  with F10.7-cm flux is evident for both PFISR-AC and PFISR-B comparisons. The decrease is not steady over the range of F10.7 values. Investigation showed that largest solar flux values were observed at the end of 2014. During this period, the electron densities were somewhat depressed compared to what one would expect from the measured F10.7-cm flux values.

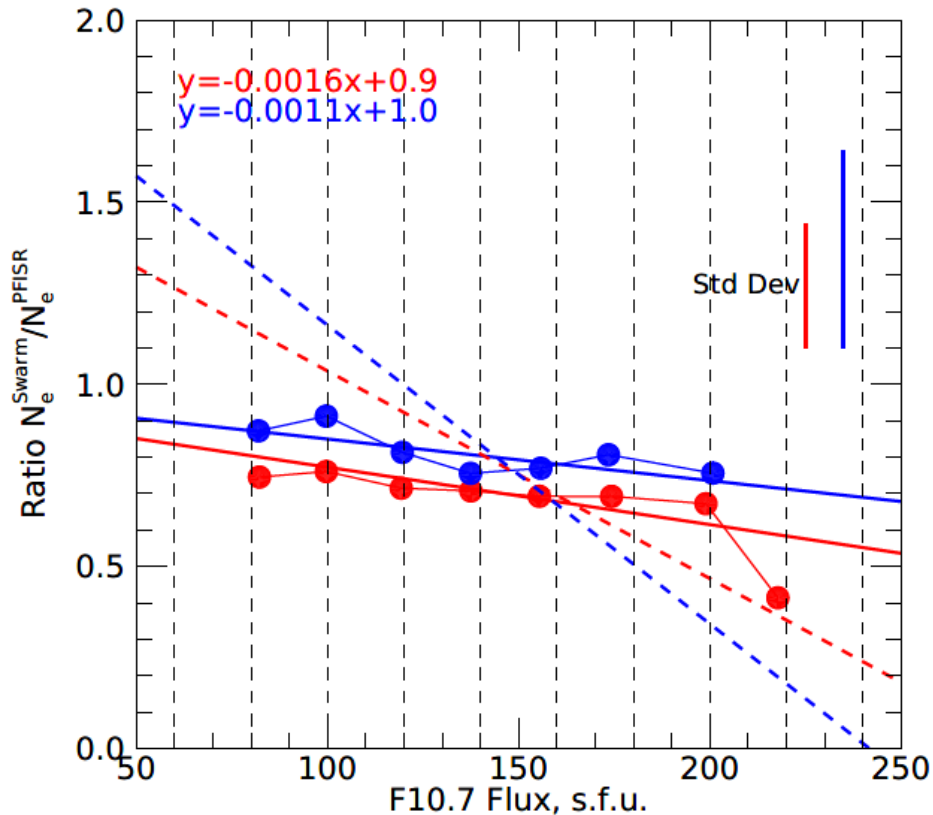


**Figure 4.13:** Medians of the ratio  $R = N_e^{Swarm}/N_e^{PFISR}$  as a function of the F10.7-cm radio flux (given in s.f.u. units) for joint PFISR-Swarm measurements from 2014 to 2016. Red and blue colors characterize PFISR conjunctions with Swarm AC and Swarm B, respectively. Bins of F10.7-cm radio flux have a step of 20 s.f.u. Typical standard deviations for  $R$  over all flux bins are shown by vertical lines, on the right. Sloped solid lines are linear fits and parameters of the fit are given in the top left corner. Sloped dashed lines are the linear fit lines as reported by Xiong et al. (2022).

The dashed lines in Figure 4.13 present the linear fit lines reported by Xiong et al. (2022) for observations at low latitudes. The slopes of these lines are larger than those found in the present study, indicating a stronger dependence for observations at low magnetic latitudes.

#### 4.4.5 UT/MLT variations of the ratio $R$

Xiong et al. (2022) presented data indicating that the Swarm overestimation effect is predominantly seen during night hours of MLT. We address this issue by plotting PFISR-Swarm data as a function of UT, Figure 4.14.

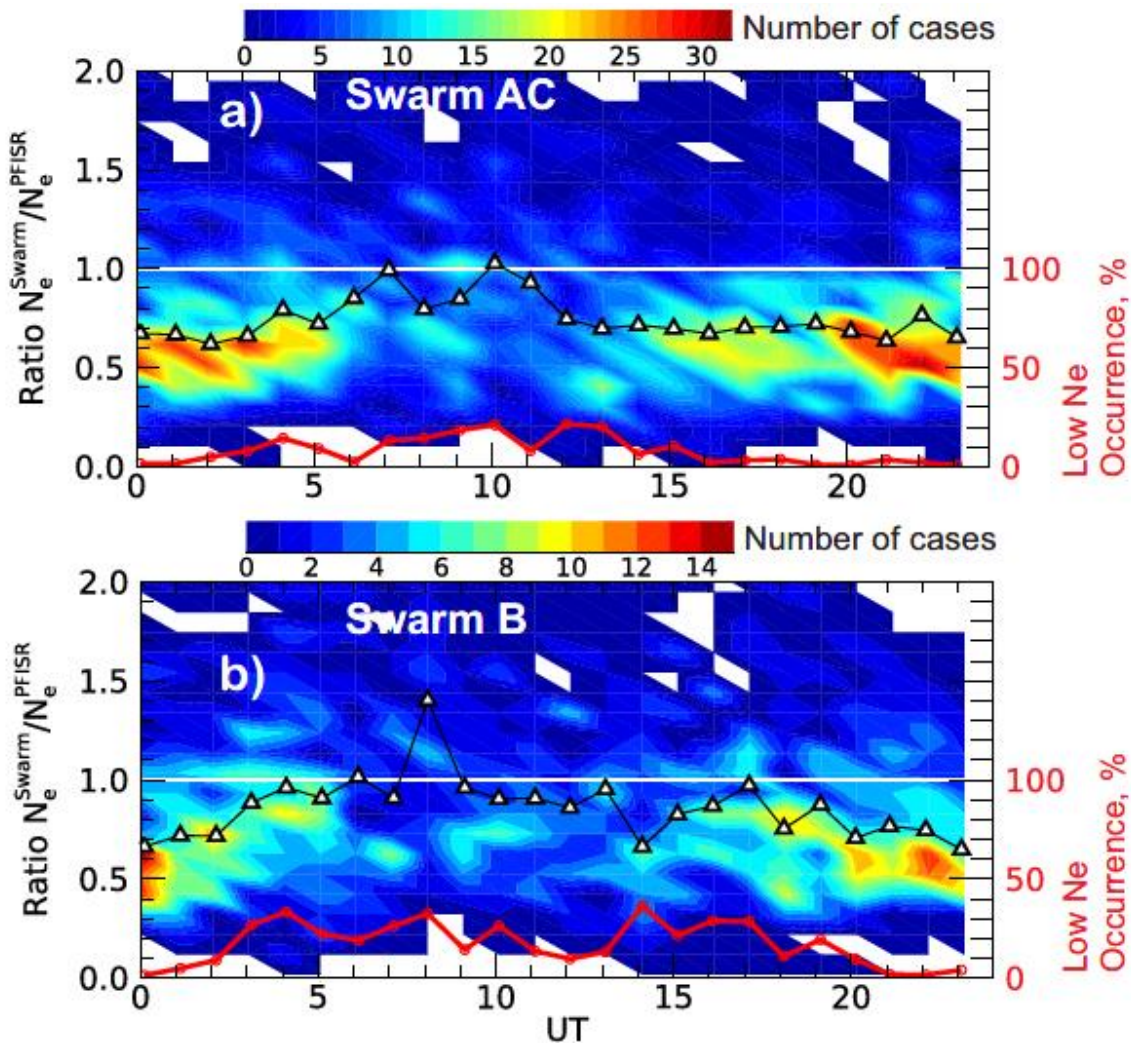


**Figure 4.14:** (a) A scatter plot for the occurrence of ratio  $R = N_e^{Swarm} / N_e^{PFISR}$  for Swarm AC versus UT time of radar-satellite conjunctions. The scale for  $R$  is represented by the bar at the top. The overlaid black-white triangles are the hourly medians of the  $R$  values. The overlaid red line is the occurrence of low electron densities,  $N_e^{PFISR} < 3 \cdot 10^{10} \text{ m}^{-3}$ , given in percent of the total number of measurements for each one-hour bin. The scale for the occurrence is shown on the right (y) axis. (b) The same as (a) but for the PFISR-B conjunctions.

Figures 4.14a and 4.14b are contour plots for the number of cases of  $R$  as a function of UT time, binned over 1-hour intervals with a step in  $R$  of 0.1. All collected data from 2014 to 2016 were considered. Overlaid on the scatter plots are medians of  $R$  values over each 1-hour UT interval (white triangles connected by black lines) and median percentage of cases with  $N_e^{PFISR} < 3 \cdot 10^{10} \text{ m}^{-3}$  (red line with scale is on the right). The magnetic local midnight for Poker Flat is roughly 11:00 UT.

Figure 4.14a for the PFISR-AC comparison indicates that the nighttime distributions are flatter than in other time sectors, where strongly dominating  $R$  values in the range of 0.5 to 0.8 (red color) are seen. The medians of  $R$  are close to 1 during pre-midnight/midnight hours. This increase of  $R$  values correlates with a general increase of the number of cases with small  $N_e^{PFISR}$  measurements, which is consistent with the general trend reported in Figure 4.11.

The data presented in Figure 4.14b for the PFISR-B comparison show similar trends to the data presented in Figure 4.14a for the PFISR-AC comparison. The minor differences in Figure 4.14b are that  $R$  values are close to 1 for a more extended period of  $11 \text{ UT} \pm 6 \text{ h}$  and the Swarm B overestimations during midnight hours are stronger.

## 4.5 Discussion of the results

This section discusses the results of the study. It should be noted that this study uses data only from high-gain units on each Swarm satellite while previous high-latitude work by Larson et al. (2021) used “blended” data sets (Catapano et al., 2021) from both high-gain and low-gain LPs.

### 4.5.1 Swarm underestimation effect

Data reported in this study support the major conclusion of all previous publications that the Swarm LP instruments mostly underestimate the electron density, both at altitudes of  $\sim 450 \text{ km}$  (Swarm AC) and  $\sim 510 \text{ km}$  (Swarm B). Expanding the initial work by Larson et al. (2021), where a “point-by-point comparison” was performed, this study considered the median of the Swarm data over much larger space and involved ISR measurements over comparable regions (latitudinally) of the ionosphere. Our analysis of the new Swarm-RISR data set for the Resolute Bay area showed that the best linear fit lines have slopes anywhere between 0.4 and 0.6, somewhat smaller but compatible with those reported by Larson et al. (2021).

The underestimation effect for Swarm LPs was reported first by Lomidze et al. (2018) and then by Smirnov et al. (2021) and Xiong et al. (2022). While Lomidze et al. (2018) characterized the scatter plots with a linear fit line with no y-offset, Smirnov et al. (2021) and Xiong et al. (2022) allowed for offsets and found them to be nonzero and positive, similar to Larson et al. (2021). Xiong et al. (2022) reported that the magnitude of underestimations changes with the solar cycle, being stronger at high solar activity (their Figures 6b and 6e) and has diurnal variation. Data presented in this study for the Resolute Bay area are too limited to make a definitive conclusion on the solar cycle effect because the RISR-C radar started operation in 2016 when the F10.7-cm flux was already low. The typical  $R$  values were about the same from 2016 to 2020. Our analysis of PFSIR and Swarm data for the Poker Flat area, which is based on a larger data set but spread over a smaller period of time, confirmed the trend reported by Xiong et al. (2022), albeit weaker for this location, shown by Figures 4.12 and 4.13.

Attempting to investigate the effect further, the PFSIR-Swarm data were sorted by time sector of local solar time. The time sectors were introduced as follows: day (20 to 02 UT), dusk (02 to 08 UT), night (08 to 14 UT) and dawn (14 to 20 UT). The time slots were shifted by 1 h to be more aligned with the magnetic local midnight at the PFSIR location. Histograms for the ratio  $R = N_e^{Swarm}/N_e^{PFSIR}$  were created, and the distribution medians and standard deviations were computed, similarly to Larson et al. (2021). Linear fit lines for scatter plots of  $N_e^{Swarm}$  versus  $N_e^{PFSIR}$  were produced for each data set. The ratio medians and standard deviations are given in Table 4.1 while information on the linear fit lines is given in Table 4.2.

**Table 4.1:** The median value  $\mu$  and the standard deviation  $\sigma$  for a histogram distribution of the ratio  $R = N_e^{Swarm}/N_e^{PFSIR}$  and number of points  $n$  for all conjunctions between RISR-AC, PFSIR-AC and PFSIR-B.

	RISR-AC			PFSIR-AC			PFSIR-B		
	$\mu$	$\sigma$	$n$	$\mu$	$\sigma$	$n$	$\mu$	$\sigma$	$n$
Day	0.73	0.44	129	0.67	0.36	786	0.70	0.46	376
Dusk	0.63	0.38	86	0.76	0.49	655	0.87	0.55	317
Night	0.78	0.36	128	0.85	0.53	487	0.98	0.61	226
Dawn	0.79	0.41	77	0.70	0.43	611	0.83	0.55	309
All	0.74	0.40	420	0.72	0.45	2539	0.83	0.55	1228

**Table 4.2:** Coefficients of a linear fit in the form  $N_e^{Swarm} = a \cdot N_e^{ISR} + b$ , total number of points, and correlation coefficient to a scatter plot of electron density measured by Swarm versus electron density measured by ISRs for all conjunctions between RISR-AC, PFISR-AC, and PFISR-B. Values of  $b$  are given in units of  $10^{10} \text{ m}^{-3}$ .

	RISR-AC			PFISR-AC			PFISR-B		
	$a$	$b$	$n/r$	$a$	$b$	$n/r$	$a$	$b$	$n/r$
Day	0.41	2.98	129/0.71	0.45	3.96	786/0.74	0.36	4.75	376/0.53
Dusk	0.50	1.17	86/0.70	0.57	2.15	786/0.74	0.71	0.90	317/0.80
Night	0.67	0.49	128/0.83	0.68	1.21	655/0.77	0.63	2.19	226/0.73
Dawn	0.56	0.82	77/0.76	0.53	2.15	487/0.75	0.49	2.43	309/0.57
All	0.57	1.00	420/0.81	0.52	2.6	2539/0.76	0.52	2.5	1228/0.64

Table 4.1 indicates that the underestimation effect is stronger during daytime and dawn where the ratio  $R$  medians are smallest, however the values for all four time sectors are in agreement within one standard deviation. Table 4.2 indicates that the underestimation effect is also stronger in day and dawn sectors where slopes of the fit line are smaller and y-offsets are larger. The data presented by Xiong et al. (2022), their Figures 6c and 6f, show stronger underestimations at nighttime compared to daytime MLT hours, i.e. a different diurnal trend.

Previous studies identified several possible reasons for the Swarm underestimations. We briefly comment on two of them. Oyama & Hirao (1976) suggested that surface contamination of LP electrodes can result in a decrease in the current through the probe resulting in a lower measured electron density. One would expect the underestimation effect to be more pronounced at larger electron densities. The results of this study support that expectation. However, if this effect is mostly responsible for the Swarm underestimations, it should be stronger at later periods of the mission with a general degradation of the instrument. Our analysis of data for the Resolute Bay location (data are not presented here) does not support this expectation as typical  $R$  values are about the same in 2016 and 2020.

Smirnov et al. (2021) and Xiong et al. (2022) concluded that plasma “contamination” with light ions could greatly affect Swarm LPs measurements. They cite the paper by Resendiz Lira and Marchand (2021), who considered a realistic model of Swarm LP probe and employed three dimensional kinetic simulations to infer the current collected by the probe under typical conditions. They showed that the difference between the electron density inferred under pure  $O^+$  plasma and plasma mixed with lighter ions can be on the order of 20%. Some of their simulations showed a

possibility of overestimations. For this reason, the expected LP underestimation in simulations is correct only in a statistical sense.

The ISR-Swarm comparison for the Poker Flat location showed results similar to those for the Resolute Bay location, Tables 4.1 and 4.2, and these results are compatible with the conclusions drawn from comparisons at middle and low latitudes (Smirnov et al. (2021) and Xiong et al. (2022)) where potential sources/processes of ionization are not the same as at high latitudes. The similarity of the conclusions at various latitudes questions the dominant role of the light ions for Swarm electron density underestimations.

### 4.5.2 Swarm overestimation effect

This study also confirmed a common occurrence of cases with Swarm LP electron density overestimations. Points with Swarm overestimations were evident in scatter plots reported previously (e.g., Lomidze et al., 2018; Smirnov et al., 2021; Xiong et al., 2022) but many of them can be attributed to the differences in the spatial and temporal resolutions of the instruments involved. For example, the uncertainty in the ISR radar calibration can be as large as 10%, as discussed by Larson et al. (2021). To quantitatively evaluate the severity of the overestimation effect for various time sectors in our data sets, we computed a percentage of points of Swarm overestimation with  $R > 1.3$ , Table 4.3.

**Table 4.3:** Percentages of cases with ratio  $R = N_e^{Swarm}/N_e^{PFISR}$  more than 1.3 for various time sectors.

	RISR-AC	PFISR-AC	PFISR-B
Day	9.2	7.7	13.6
Dusk	5.8	13.6	20.5
Night	11.7	19.3	29.2
Dawn	13.0	9.3	18.5

Table 4.3 indicates that Swarm overestimations occur more frequently at night/dawn for both Swarm AC and Swarm B, and they are more frequent for Swarm B for any time of a day. Qualitatively, these tendencies are recognizable in plots of Figure 4.14.

Smirnov et al. (2021) were the first authors who expressed the notion of Swarm overestimations explicitly. They reported the overestimation effect for the nighttime ionosphere at low to middle and equatorial latitudes (their Figure 7). No effect is evident in their plots at high

latitudes, although the data statistics are lower there (their Figure 8). One needs to keep in mind that the radio occultation approach to electron density profiles derivation (data used by Smirnov et al. (2021)) assumes a spherically layered ionosphere, which might not always be correct for the high latitude ionosphere. The overestimation effect shown by Smirnov et al. (2021) is most evident for the electron densities measured by the Constellation Observing System for Meteorology, Ionosphere, and Climate (COSMIC) satellites below  $5 \cdot 10^{10} \text{ m}^{-3}$  (their Figure 7) which is consistent with Figure 4.11 of this study.

Xiong et al. (2022), while comparing Swarm LP and Jicamarca ISR (a near equatorial radar) data, showed that the Swarm overestimation effect varies with the solar cycle and MLT time of observations (their Figure 6). The effect was stronger in 2019 and 2020, the period of lowest solar activity. Our analysis for a high-latitude region based on a much larger data set (although covering a smaller time period) showed an increase of Swarm overestimations with the decay of the solar activity, consistent with their results. Xiong et al. (2022) proposed Swarm density correction equations based on values of the F10.7-cm radio flux. Although their equations work well at near-equatorial latitudes, and presumably for low-gain LPs, their applicability to other latitudes requires further investigation, as our comparisons for high-gain LPs showed much weaker trends (Figure 4.13).

Swarm electron density overestimations are not a random feature of the data. They occur very frequently during low electron densities in the ionosphere, as shown in our Figure 4.11. Indirect supporting evidence is a systematic inference, shown in previous publications, that the linear fit line to Swarm electron density scatter plots versus data from an independent instrument has a non-zero and positive y-offset. Explanations of the effect in terms of the physics or hardware operation features is a challenging task. One possible reason for the Swarm electron density overestimations at low density is that the ISR measurements at low electron density become more unreliable. At low densities, the return signal detected by the ISR is weaker and the relative error in the measurements increases, especially at higher altitudes as seen in Figure 4.2b. For this reason, utilizing larger integration times for ISRs would be beneficial. However, for the purpose of the present work, this can hardly be justified because the satellites pass the radars' observational region in a matter of minutes. The fact that 1-min and 5-min RISR data are not quite consistent, as shown in Section 2.2, is a good indicator that dedicated ISR experiments, utilizing improved capabilities

for the topside ionosphere measurements, would be interesting to conduct in conjunction with Swarm measurements.

## 4.6 Conclusions

The major results of this study are summarized as follows:

1. Overall, electron densities measured by the Swarm satellites with high-gain LP instruments are smaller than those measured by the incoherent scatter radars at Resolute Bay in the polar cap and at Poker Flat in the auroral zone. Extensive satellite-radar comparisons at Poker Flat showed that scatter plots of Swarm versus ISR electron density have a slope of the best fit line of  $\sim 0.52$  for both Swarm AC and Swarm B. The y-offsets of the linear fit lines are  $2 \cdot 10^{10} \text{ m}^{-3}$  and are positive.
2. The comparisons for the Poker Flat location showed that Swarm electron density underestimations occur predominantly during daytime and dawn, and the effect is stronger at high solar activity. The underestimation effect is stronger when there are higher electron densities in the topside ionosphere.
3. The comparisons for the Poker Flat location confirmed existence of Swarm overestimations at high latitudes, earlier reported by Smirnov et al. (2021) and Xiong et al. (2022) at middle and low latitudes.  $N_e^{Swarm}$  overestimations are evident for low electron densities ( $N_e^{PFISR} < 3 \cdot 10^{10} \text{ m}^{-3}$ ). Indirect evidence of Swarm overestimations is observed as positive offsets for the linear fit lines to scatter plots of  $N_e^{Swarm}$  versus  $N_e^{PFISR}$  in the ionosphere. The effect was observed in 10 to 20% of conjunctions, and more frequently for Swarm B compared to Swarm A and C.
4. The Swarm overestimation effect is stronger at lower solar activity, consistent with an overall decrease of the electron density in the topside ionosphere.

# Chapter 5

## Summary of the thesis work and suggestions for future research

This chapter will summarize the work presented in this thesis and suggest possible ways to expand the research. This thesis had two independent research topics. The first was assessing the electron density profiles over Poker Flat, Alaska and the second was validating the Swarm LP in situ electron density measurements in the ionospheric topside over Poker Flat, Alaska and Resolute Bay, Canada. The key instruments for both topics were incoherent scatter radars.

### 5.1 Summary of the thesis work

Below is a summary of the results and conclusions for both research topics.

#### 5.1.1 Seasonal and diurnal variations of the electron density over Poker Flat

To study the electron density profiles over Poker Flat, data for two full years of observations were analyzed. The two years selected were 2014 and 2016, corresponding to relatively high and low solar activity, respectively. Observations in a specially designed mode of operation, “in support of International Polar year (IPY)”, were selected. This mode provided 5-min resolution data in four beams slightly spread around Poker Flat. The data were calibrated and treated consistently over long periods, which is important for the objectives of the work. For inferring trends in changes of the electron density the median value of the four beams was taken and grouped by height with a bin size of 20 km.

First, Objectives 1.1 (page 21) and 1.2 (page 22) were addressed. Assessing the UT/diurnal variations of the electron density for various seasons showed that electron densities are largest during daytime in spring, and smallest during nighttime in winter. Electron density values in 2014 were larger than those in 2016 by a factor of 2 to 5, supporting the notion that high latitude electron

density profiles are highly sensitive to solar radiation flux. Electron density enhancements around midnight at low heights in the upper E region and bottomside F region were identified, indicating input to the ionosphere from particle precipitation related to auroral substorms.

The seasonal variation of the electron density for four time sectors was addresses and it was found that daytime electron densities are stronger during equinoctial periods and at winter time, and there is a semi-annual type of variation. The semi-annual seasonal variation of daytime electron densities at low solar activity is much weaker. During nighttime, the electron density is stronger in the summer and weaker in the winter, showing annual variation. The results from the analysis of the overall electron density profiles are consistent with the results of the diurnal and seasonal variation assessment for the peak electron densities  $N_mF2$ .

The height of the peak density  $h_mF2$  was plotted on a month-UT plane which showed complicated patterns with some differences between 2014 and 2016. In 2014, the largest heights occurred at night during the winter and equinoctial periods, and the lowest heights during the day in summer, with differences on the order of ~50 km. The diurnal variations were smaller in 2014 and the pattern had special signatures near sunrise and sunset. It was stated in Chapter 3 that  $h_mF2$  seasonal variations needed further investigation.

To address Objective 1.3 (page 22), trends for the scale height  $H_o$ , which roughly reflects the thickness of the F2 layer, were investigated. Assessing seasonal trends identified that the layer is thickest in the summer, and thinnest in the winter. At low solar activity in 2016, the layer is generally thinner than at high solar activity in 2014. It was also demonstrated that the NeQuick ionospheric model with adjusted parameters reasonably describes the diurnal variation of the electron density at ~450 km.

### 5.1.2 Validation work for Swarm LP instruments

This topic is an expansion of the validation work performed by Bion Larson in 2020/2021 (Larson, 2022). The objective was to assess the performance of the Swarm LP instruments as the satellites travel over Resolute Bay (Canada) and Poker Flat (Alaska), regions that are deep inside the polar cap and at subauroral-auroral latitudes, respectively. The approach to data handling is quite different from that used by Larson (2021). Instead of considering close conjunctions between a range gate of a specific RISR beam and one of the Swarm satellites, median values of the Swarm LP data over comparable latitudinal regions were taken. The ISR data consisted of 21 beams for

RISR-C and 4 beams for PFISR. Additionally, a larger longitudinal separation between the radar measurement zone and satellite footprints was allowed. This approach is consistent with that adopted in several recent Swarm publications (e.g., Lomidze et al., 2018; Xiong et al., 2022). An advantage of relaxing the requirement on the proximity of the satellite with respect to the radar is that more conjunctions are considered, thus enlarging the data statistics.

Analysis of the RISR-Swarm data obtained by the different approach (Objective 2.1, page 23) showed results that were very similar to those reported by Larson (2021) and Larson et al. (2021). The Swarm LP measurements mostly underestimate electron densities in the polar cap by up to 30-40%, as judged from the linear fit lines. The degree of agreement was investigated separately for four different time sectors, and it was found that agreement is slightly better during the night and worse during the day and dawn.

To address Objective 2.2 (page 23), the performance of the Swarm LPs was then assessed over Poker Flat using the PFISR radar, which had a much larger data set. For this more extensive satellite-radar comparison, the linear fit lines for scatter plots of Swarm versus ISR electron density have a slope of  $\sim 0.52$ , for both Swarm AC and Swarm B, showing  $\sim 48\%$  underestimation which is slightly larger than in the polar cap. The y-offsets of the linear fit lines were  $\sim 2 \cdot 10^{10} \text{ m}^{-3}$  and positive, qualitatively in agreement with measurements over Resolute Bay. It was revealed that the Swarm electron density underestimations occur predominately during daytime, and the effect is stronger at higher solar activity. The stronger underestimation effect correlates with the occurrence of larger electron densities in the topside ionosphere.

Swarm electron density overestimations were then investigated (Objective 2.3, page 23). The scatter plots discussed above confirmed the existence of Swarm overestimations at high latitudes (Poker Flat), which have been reported by others for middle and low latitudes. Swarm overestimations were evident for low electron densities ( $N_e^{PFISR} < 3 \cdot 10^{10} \text{ m}^{-3}$ ). The effect was observed in  $\sim 20\%$  of joint measurements, and more frequently for Swarm B. The overestimation effect is more frequent at lower solar activity, consistent with an overall decrease of the electron density in the topside ionosphere.

To address Objective 2.4 (page 23), the joint satellite-radar data from Swarm AC and Swarm B were compared. The slopes of the linear fit lines for the Swarm AC ( $\sim 450 \text{ km}$ ) comparison are about the same as for the Swarm B ( $\sim 510 \text{ km}$ ) comparison. However, measurements at  $\sim 510 \text{ km}$  showed more cases of overestimation.

## 5.2 Suggestions for future research

This section will discuss potential ways to expand the efforts undertaken in the thesis.

### 5.2.1 Study of long-term trends in the ionosphere over Alaska

The work on assessing diurnal, seasonal and solar cycle variations of the electron density over Poker Flat requires further expansion, specifically in terms of data coverage. PFISR data are available from 2007 to 2022, which begins at solar minimum, covers the maximum years of solar cycle 24, and the next solar cycle minimum (Figure 1.2). The justification of this work comes from the fact that these variations in electron density can be different in the ascending and descending phases of the solar cycle, as demonstrated by Ratovsky et al. (2014) and Zheng et al. (2017) for the Siberian sector. The data presented by Zheng et al. (2017) also showed a noticeable change in the variations from the middle latitude station Irkutsk and the high latitude station Norilsk, and that the solar cycle variations can be different depending on the latitude. Data reported by Sheng et al. (2014) for the European Incoherent Scatter Scientific Association (EISCAT) ISR also indicated different relative amplitudes of variations.

Multi-year data over Poker Flat can address another interesting aspect of ionospheric F layer. As explained in Chapter 1, the F2 layer is formed by contributions from solar radiation and diffusion processes. It is well established that the peak electron density  $N_mF2$  is sensitive to the intensity of solar radiation flux, traditionally represented by F10.7-cm flux (e.g., Lei et al., 2005). The dependence is almost linear for F10.7-cm flux  $< 200$  s.f.u. and saturates at higher values. Plotting  $N_mF2$  values versus F10.7-cm flux over the entire solar cycle leads to a pattern similar to the hysteresis curve in magnetism, and it would be interesting to see if the feature exists over Poker Flat. The nature of the hysteresis dependence is not quite clear, and additional information might help in understanding the physics behind this unique feature.

Another topic regarding the dependence of the electron density on solar radiation is the role of the solar zenith angle. Data for the height of the peak density  $h_mF2$  presented in Figure 3.6 indicated their potential relationship. Ratovsky et al. (2014) presented  $N_mF2$  data for Norilsk (GLAT = 69° N) that illustrates the solar illumination control of  $N_mF2$ . However, for the very high latitude station Longyearbyen, Sheng et al. (2014) found different patterns of variations supporting

the notion that “magnetosphere-ionosphere coupling processes, such as particle precipitation and plasma convection, play a significant role in the high latitude ionosphere.” Poker Flat is located in a transition region from middle latitudes to the auroral latitudes, and work in this area would be important. Overall, it is desirable to sort the data according to the solar zenith angle and investigate  $N_mF2$  and  $h_mF2$ .

Another interesting topic is the thickness of the F layer. The analysis in Chapter 3 showed seasonal dependencies that are quite different from observations at middle latitudes reported by Lei et al. (2005) from the Millstone Hill ISR (GLAT = 42.6° N). Lei et al. (2005) used a Chapman-like profile to fit the data while the data presented in Chapter 3 of this thesis used the NeQuick function. The differences in the trends are expected to be small, but to fully understand the differences in seasonal dependencies at middle and auroral latitudes the same fitting function would need to be applied to both data sets.

Finally, the seasonal variation of the electron density with maxima in winter (Figure 3.3) suggests that one should expect higher ground scatter occurrence rate for the Kodiak SuperDARN radar in winter or equinoxes compared to summer. This prediction needs to be confirmed by statistical analysis of Kodiak data. It would be interesting to determine if the effect also exists during years of low solar activity for which the winter anomaly effect is weaker.

## 5.2.2 Further validation work for the NeQuick ionospheric model

The validation work for the NeQuick ionospheric model in this thesis was limited to checking whether it reasonably reproduces the diurnal variation at the ionospheric topside (due to time constraints). This is a very narrow scope and below are several ways to expand the validation work.

One issue is to investigate if the empirical formula for the parameter  $H_o$  (equation 9 in Themens et al., 2018) is consistent with values obtained by fitting profiles with fixed values of  $r$  and  $g$ . This would require an assessment of the solar zenith angle and magnetic activity for specific electron density profiles.

The current effort of ionospheric physicists working on the improvement of the NeQuick model is focused on identifying optimal values for the parameters  $r$ ,  $g$ , and  $H_o$  (Pignalberi et al., 2020; 2022). Analysis of radio occultation data in those studies has shown that the optimal values vary with latitude, longitude, and solar activity level. It would be beneficial to refit the NeQuick function to the PFISR electron density profiles allowing for  $r$  and  $g$  to be independent variables,

instead of just  $H_0$ . A limited analysis of this method showed that the obtained values are similar to those suggested by Themens et al. (2018), but a statistical assessment of the data might allow more precise parameters for the Poker Flat area to be determined. The optimal values suggested by Themens et al. (2018) were based on data from PFISR and three other ISRs, located at different latitudes and longitudes.

To conclude this chapter, and this thesis, the work undertaken has led to a better understanding of the electron density distribution at high latitudes, and the way the LPs on the Swarm satellites measure electron density in the ionospheric topside. However, more work needs to be done to have better ionosphere specification for space weather monitoring and forecasting.

# References

- Alfonsi, L., Kavanagh, A. J., Amata, E., Cilliers, P., Correiam E., Freeman, M., Kauristie, K., Liu, R., Luntama, J., Mitchell, C. N., & Zherebtsov, G. A. (2008). Probing the high latitude ionosphere from ground-based observations: The state of current knowledge and capabilities during IPY (2007-2009). *J. Atmos. Solar-Terr. Phys.*, *70*, 2293-2308. <https://doi.org/10.1016/j.jastp.2008.06.013>
- Bahcivan, H., Tsunoda, R., Nicolls, M., & Heinselman, C. (2010). Initial ionospheric observations made by the new resolute incoherent scatter radar and comparison to solar wind IMF. *Geophys. Res. Lett.*, *37*, L15103. <https://doi.org/10.1029/2010GL043632>
- Belehaki, A., Tsagouri, I., Kutiev, I., Marinov, P., Zolesi, B., Pietrella, M., Themelis, K., Elias, P., & Tziotziou, K. (2015). The European Ionosonde Service: Nowcasting and forecasting ionospheric conditions over Europe for the ESA space situational awareness services. *J. Space Weather Space Clim.*, *5*, A25. <https://doi.org/10.1051/swsc/2015026>
- Belehaki, A., Tsagouri, I., & Paouris, E. (2022). Characteristics of the effective scale height in the topside ionosphere extracted from Swarm A and Digisonde observations: Preliminary results. *J. Geophys. Res.: Space Phys.*, *127*, e2021JA030075. <https://doi.org/10.1029/2021JA030075>
- Beynon, W. J. G., & Williams, P. J. S. (1978). Incoherent scatter of radio waves from the ionosphere. *Reports on Progress in Physics*, *41*, 909. <https://doi.org/10.1088/0034-4885/41/6/003>
- Bhattacharai, S., & Mishra, L. N. (2017). Theoretical study of spherical Langmuir probe in Maxwellian plasma. *International Journal of Physics*, *5*, 73–81. <https://doi.org/10.12691/ijp-5-3-2>
- Bilitza, D., Altadill, D., Truhlik, V., Shubin, V., Galkin, I., Reinisch, B., & Huang, X. (2017). International reference ionosphere 2016: From ionospheric climate to real-time weather predictions. *Space Weather*, *15*, 418-429. <https://doi.org/10.1002/2016SW001593>
- Bilitza, D. (2018). IRI the international standard for the ionosphere. *Adv. Radio Sci.*, *16*, 1-11. <https://doi.org/10.5194/ars-16-1-2018>
- Bilitza, D., Pezzopane, M., Truhlik, V., Atadill, D., Reinisch, B., & Pignalberi, A. (2022). The international reference ionosphere model: A review and description of an ionospheric benchmark. *Reviews of Geophysics*, *60*, e2022RG000792. <https://doi.org/10.1029/2022RG000792>
- Bowles, K. L. (1958). Observation of vertical-incidence scatter from the ionosphere at 41 Mc/sec. *Phys. Rev. Lett.*, *1*, 454-455. <https://doi.org/10.1103/PhysRevLett.1.454>
- Brekke, A. (2013). *Physics of the upper polar atmosphere* (2nd ed.). Springer.

- Buchert, S. (2021). Langmuir Probe Level 1b Algorithm, ESA report Doc. no: SW-TN-IRF-EF-003, Rev: 3D, 2021-06-07, Downloaded from <https://earth.esa.int/eogateway/documents/20142/37627/swarm-level-1b-plasma-processor-algorithm.pdf> on 31 May 2023.
- Buchert, S., Zangerl, F., Sust, M., André, M., Eriksson, A., Wahlund, J. -E., & Opgenoorth, H. (2015). Swarm observations of equatorial electron densities and topside GPS track losses. *Geophys. Res. Lett.*, *42*, 2088–2092. <https://doi.org/10.1002/2015GL063121>
- Buzulukova, N., & Tsurutani, B. (2022). Space weather: from solar origins to risks and hazards evolving in time. *Frontiers in Astronomy and Space Physics*, *9*. <https://doi.org/10.3389/fspas.2022.1017103>
- Cai, H. T., Ma, S. Y., Fan, Y., Liu, Y. C., & Schlegel, K. (2007). Climatological features of electron density in the polar ionosphere from long-term observations of EISCAT/ESR radar. *Ann. Geophys.*, *25*, 2561–2569. <https://doi.org/10.5194/angeo-25-2561-2007>
- Catapano, F., Buchert, S., Qamili, E., Nilsson, T., Bouffard, J., Siemes, C., Coco, I., D’Amicis, R., Tøffner-Clausen, L., Trenchi, L., Olsen, P. E. H., & Stromme, A. (2021). Swarm Langmuir Probes' data quality and future improvements. *Geoscientific Instrumentation, Methods and Data Systems*, *11(1)*, 149-162. <https://doi.org/10.5194/gi-2021-17>
- Chen, F. F. (2003). Lecture notes on Langmuir probe diagnostics. Electrical Engineering Department University of California, Los Angeles. Mini-Course on Plasma Diagnostics, IEEE-ICOPS meeting, Jeju, Korea, June 5, 2003. <https://www.seas.ucla.edu/~ffchen/Pubs/Chen210R.pdf>. Downloaded on 29 May 2023.
- Coisson, P., Radicella, C. M., Leitinger, R., & Nava, B. (2006). Topside electron density in IRI and NeQuick: Features and limitations. *Adv. Space Res.*, *37*, 937-942. <https://doi.org/10.1016/j.asr.2005.09.015>
- Cravens, T. E. (1997). *Physics of solar system plasmas*, Cambridge University Press.
- Crowley, G., Ridley, A. J., Deist, D., Wing, S., Knipp, D. J., Emery, B. A., Foster, J., Heelis, R., Hairston, M., & Reinisch, B. W. (2000). Transformation of high-latitude ionospheric F region patches into blobs during the March 21, 1990 storm. *J. Geophys. Res.: Space Phys.*, *105(A3)*, 5215-5230. <https://doi.org/10.1029/1999JA900357>
- Damba, J. (2020). Characterization of plasma streams and ion populations from plasma thrusters for space propulsion. PhD. Thesis, Universidad Politécnica de Madrid, 2020. [https://oa.upm.es/64130/1/JULIUS\\_DAMBA.pdf](https://oa.upm.es/64130/1/JULIUS_DAMBA.pdf)
- Diaz, M. A., Semeter, J. L., Oppenheim, M., & Zettergren, M. (2008). Particle-in-cell simulation of the incoherent scatter radar spectrum. *Radio Sci.*, *43*, RS1007. [doi:10.1029/2007RS003722](https://doi.org/10.1029/2007RS003722)
- Dote, T., Amemiya, H., & Ichimiya, T. (1965). Effect of the geomagnetic field on an ionospheric sounding probe. *J. Geophys. Res.: Space Phys.*, *70*, 2258-2261. <https://doi.org/10.1029/JZ070i009p02258>

- Fast, H., A. Koustov, & R. Gillies, 2023. Validation of Swarm Langmuir probes by incoherent scatter radars at high latitudes. *Remote Sensing*, 15, 1846. <https://doi.org/10.3390/rs15071846>
- Feldstein, Y. I. (2016). The discovery and the first studies of the auroral oval: A review. *Geomagnetism and Aeronomy*, 56, 129–142. <https://doi.org/10.1134/S0016793216020043>
- Feng, J., Han, B., Zhao, Z., & Wang, Z. (2019). A new global Total Electron Content empirical model. *Remote Sensing*, 11, 706. <https://doi.org/10.3390/rs11060706>
- Friis-Christensen, E., Lühr, H., Knudsen, D., & Haugmans, R. (2008). Swarm – an Earth observation mission investigating geospace. *Adv. Space Res.*, 41, 210–216. <https://doi.org/10.1016/j.asr.2006.10.008>
- Ghezelbash, M. (2013). Occurrence and causes of F-region echoes for the Canadian PolarDARN/SuperDARN radars. M.Sc. Thesis, University of Saskatchewan, 2013. <http://hdl.handle.net/10388/ETD-2013-03-949>
- Gillies, R. G., van Eyken, A., Spanwich, E., Nicolls, M., Kelly, J., Greffen, M., Knudsen, D., Connors, M., Schutzer, M., Valentice, T., Malone, M., Buonocore, J., St.-Maurice, J., -P., & Donovan, E. (2016). First observations from the RISR-C incoherent scatter radar, *Radio Sci.*, 51, 1645 – 1659. <https://doi.org/10.1002/2016RS006062>.
- Gillies, R. G., & Varney, R. (2016). Introduction to the Resolute Bay incoherent scatter radars (RISR). Retrieved June 8, 2023 from [https://data.phys.ucalgary.ca/sort\\_by\\_project/RISR-C/documentation/RISR\\_information.pdf](https://data.phys.ucalgary.ca/sort_by_project/RISR-C/documentation/RISR_information.pdf).
- Hägström, I. (2017). Incoherent and coherent scatter radars. In *The ESPAS e-infrastructure: Access to data from near-Earth space* (pp. 117-126). Les Ulis: EDP Sciences. <https://doi.org/10.1051/978-2-7598-1949-2.c012>
- Hargreaves, J. K. (1992). *The solar-terrestrial environment*. Cambridge University Press. <https://doi.org/10.1017/CBO9780511628924>
- Hervás, M., Bergadà, P., & Alsina-Pagès, R. M. (2020). Ionospheric narrowband and wideband HF soundings for communications purposes: A Review. *Sensors*, 20(9), 2486. <https://doi.org/10.3390/s20092486>
- Hocke, K., & Igarashi, K. (2002). Electron density in the F region derived from GPS/MET radio occultation data and comparison with IRI. *Earth, Planets and Space*, 54, 947–954. <https://doi.org/10.1186/BF03352442>
- Huba, J. D., Schunk, R.W., & Khazanov, G. V. (Eds.) (2014). *Modeling the ionosphere-thermosphere (geophysical monograph series)*, Volume 201. American Geophysical Union.
- Hunsucker, R. D. (1991). *Radio techniques for probing the terrestrial ionosphere*. Springer-Verlag.

- Kakinami, Y., Watanabe, S., & Oyama, K. -I. (2008). An empirical model of electron density in low latitude at 600 km obtained by Hinotori satellite. *Adv. Space Res.*, *41*, 1495–1499. <https://doi.org/10.1016/j.asr.2007.09.031>
- Kane, R. P. (2002). Periodicities in the time series of solar coronal radio emissions and chromospheric UV emission lines. *Solar Phys.*, *205*, 351-359. <https://doi.org/10.1023/A:1014253824687>
- Karpachev, A. T., Klimenko, M. V., Kilmenko, V. V., & Pustovalova, L. V. (2016). Empirical model of the main ionospheric trough for the nighttime winter conditions. *J. Atmos. Solar-Terr. Phys.*, *146*, 149-159. <https://doi.org/10.1016/j.jastp.2016.05.008>
- Kelley, M. C. (2009). *The Earth's ionosphere* (2nd ed.). Academic Press.
- Kim, E., Jee, G. Ji, E-Y, Kim, Y. H., Lee, C., Kwak, Y-S, & Shim, S.-S. (2020). Climatology of polar ionospheric density profile in comparison with mid-latitude ionosphere from long-term observations of incoherent scatter radars: A review. *J. Atmos. Solar Terr. Phys.*, *211*, 105449. <https://doi.org/10.1016/j.jastp.2020.105449>
- Kivelson, M. G., & Russell, C. T. (Eds.). (1995). *Introduction to space physics*. Cambridge University Press. <https://doi.org/10.1017/9781139878296>
- Klimenko, M. V., Zakharenkova, I. E., Klimenko, V. V., Lukianova, R. Y., & Cherniak, I. V. (2019). Simulation and observations of the polar tongue of ionization at different heights during the 2015 St. Patrick's Day storm. *Space Weather*, *17*, 1073–1089. <https://doi.org/10.1029/2018SW002143>
- Knudsen, D. J., Burchill, J. K., Buchert, S. C., Eriksson, A. I., Gill, R., Wahlund, J. -E., Åhlen, L., Smith, M., & Moffat, B. (2017). Thermal ion imagers and Langmuir probes in the Swarm electric field instruments. *J. Geophys. Res.: Space Phys.*, *122*, 2655-2673. <https://doi.org/10.1002/2016JA022571>
- Kontor, N. N. (1993). Long term variability of solar activity. *Adv. Space Res.*, *13*, 417-427. [https://doi.org/10.1016/0273-1177\(93\)90514-C](https://doi.org/10.1016/0273-1177(93)90514-C)
- Kotova, D. S., Ovodenko, V. B., Yasyukevich, Yu. V., Klimenko, M. V., Mylnikova, A. A., Kozlovsky, A. E., & Gusakov, A. A. (2018). Correction of IRI-Plus and NeQuick empirical ionospheric models at high latitudes using data from the remote receivers of Global Navigation Satellite system signals. *Russian Journal of Physical Chemistry B*, *12*, 776-781. <https://doi.org/10.1134/S1990793118040127>
- Kotova, D., Jin, Y., & Miloch, W. (2022). Interhemispheric variability of the electron density and derived parameters by the Swarm satellites during different solar activity. *J. Space Weather Space Clim.*, *12*, 12. <https://doi.org/10.1051/swsc/2022007>
- Kutiev, I., Tsagouri, I., Perrone, L., Pancheva, D., Mukhtarov, P., Mikhailov, A., Lastovicka, J., Jakowski, N., Buresova, D., Blanch, E., Andonov, B., Altadill, D., Magdaleno, S., Parisi, M., & Torta, J.M. (2013). Solar activity impact on the Earth's upper atmosphere. *J. Space Weather Space Clim.*, *3*, A06. <https://doi.org/10.1051/swsc/2013028>

- Larson, B. (2021). Comparative study of polar cap electron density measurements and E-Chaim modeling. M.Sc. Thesis, University of Saskatchewan, 2021. <https://harvest.usask.ca/handle/10388/13751>
- Larson, B., Koustov, A. V., Kouznetsov, A. F., Lomidze, L., Gillies, R. G., & Reimer, A. S. (2021). A comparison of the topside electron density measured by the Swarm satellites and incoherent scatter radars over Resolute Bay, Canada. *Radio Sci.*, *56*, e2021RS007326. <https://doi.org/10.1029/2021RS007326>
- Larson, B., Koustov, A. V., Themens, D. R., & Gillies, R. G. (2023). Ionospheric electron density over Resolute Bay according to E-CHAIM model and RISR radar measurements. *Adv. Space Res.*, *71*, 2759-2769. <https://doi.org/10.1016/j.asr.2023.01.017>
- Laštovička, J. (2017). A review of recent progress in trends in the upper atmosphere *J. Atmos. Solar-Terr. Phys.*, *163*, 2–13. <https://doi.org/10.1016/j.jastp.2017.03.009>
- Lei, J., Liu, L., Wan, W., & Zhang, S.-R. (2005). Variations of electron density based on long-term incoherent scatter radar and ionosonde measurements over Millstone Hill, *Radio Sci.*, *40*, RS2008, <https://doi.org/10.1029/2004RS003106>.
- Lomidze, L., Knudsen, D. J., Burchill, J., Kouznetsov, A., & Buchert, S. C. (2018). Calibration and validation of Swarm plasma densities and electron temperatures using ground-based radars and satellite radio occultation measurements. *Radio Sci.*, *53*, 15-36. <https://doi.org/10.1002/2017RS006415>
- Ma, R., Xu, J., Wang, W., & Yuan, W. (2009). Seasonal and latitudinal differences of the saturation effect between ionospheric NmF2 and solar activity indices. *J. Geophys. Res.*, *114*, A10. <https://doi.org/10.1029/2009JA014353>
- Mathews, J. D., Briczinski, S. J., Meisel, D. D., & Heinselman, C. J. (2007). Radio and meteor science outcomes from comparisons of meteor radar observations at AMISR Poker Flat, Sondrestrom, and Arecibo. *Earth Moon and Planet.*, *102*, 365-378. <https://doi.org/10.1007/s11038-007-9168-0>
- McWilliams, K., André, D., Greenwald, R., Schiffler, A., Sofko, G., & Yeoman, T. (2003). SuperDARN pulse sequences - optimization and testing. Retrieved June 15, 2023 from <https://chapman.usask.ca/assets/FITACF-Tutorial.pdf>.
- Merlino, R. L. (2007). Understanding Langmuir probe current-voltage characteristics. *American Journal of Physics*, *75*, 1078–1085. <https://doi.org/10.1119/1.2772282>
- Michell, R. G., Grydeland, T., & Samara, M. (2014). Characteristics of Poker Flat incoherent scatter radar (PFISR) naturally enhanced ion-acoustic lines (NEIALs) in relations to auroral forms. *Ann. Geophys.*, *32*, 1333-1347. <https://doi.org/10.5194/angeo-32-1333-2014>
- Mishin E. V., & Streltsov, A. V. (2021). *Nonlinear wave and plasma structures in the auroral and subauroral geospace*. Elsevier

- Mott-Smith, H. M., & Langmuir, I. (1926). The theory of collectors in gaseous discharges. *Phys. Rev.*, *28*, 727–763. <https://doi.org/10.1103/PhysRev.28.727>
- Nava, B., Radicella, S. M., Pulinetz, S., & Depuev, V. Kh. (2001). Modelling bottom and topside electron density and TEC with profile data from topside ionograms. *Adv. Space Res.*, *27*, 31-34. [https://doi.org/10.1016/S0273-1177\(00\)00137-X](https://doi.org/10.1016/S0273-1177(00)00137-X)
- Nava, B., Coisson, P., & Radicella, S. M. (2008). A new version of the NeQuick ionosphere electron density model. *J. Atmos. Solar-Terr. Phys.*, *70*, 1856-1862. <https://doi.org/10.1016/j.jastp.2008.01.015>
- Nishitani, N., Ruohoniemi, J. M., Lester, M., Baker, J. B. H., Koustov, A. V., Shepherd, S. G., Chisham, G., Hori, T., Thomas, E. G., Makarevich, R. A., Marchaudon, A., Ponomarenko, P., Wild, J. A., Milan, S. E., Bristow, W. A., Devlin, J., Miller, E., Greenwald, R. A., Ogawa, T., & Kikuchi, T. (2019). Review of the accomplishments of mid-latitude Super Auroral Radar Network (SuperDARN) HF radars. *Progress in Earth and Planetary Science*, *6*, A27. <https://doi.org/10.1186/s40645-019-0270-5>
- Oyama, K.-I., & Hiraio, K. (1976). Inaccuracies in electron density estimates due to surface contamination of Langmuir probes. *Planetary and Space Science*, *24*, 87–89. [https://doi.org/10.1016/0032-0633\(76\)90065-9](https://doi.org/10.1016/0032-0633(76)90065-9)
- Özgüç, A., Ataç, T., & Pektaş, R. (2008). Examination of the solar cycle variation of foF2 for cycles 22 and 23. *J. Atmos. Solar-Terr. Phys.*, *70*, 268-276. <https://doi.org/10.1016/j.jastp.2007.08.016>
- Parker, E. N. (1959). Extension of the solar corona into interplanetary space, *J. Geophys. Res.: Space Phys.*, *64*, 1675-1681.
- Pignalberi, A., Pezzopane, M., & Rizzi, R. (2018). Modeling the lower part of the topside ionospheric vertical electron density profile over the European region by means of Swarm satellites data and IRI UP method. *Space Weather*, *16*, 304–320. <https://doi.org/10.1002/2017SW001790>
- Pignalberi, A., Pezzopane, M., Themens, D. R., Haralambous, H., Nava, B., & Coisson, P. (2020). On the analytical description of the topside ionosphere by NeQuick: Modeling the scale height through COSMIC/FORMOSAT-3 selected data. *IEEE Journal of Selected Topics in Applied Earth Observations and Remote Sensing*, *13*, 1867–1878. <https://doi.org/10.1109/JSTARS.2020.2986683>
- Pignalberi, A., Pezzopane, M., & Nava, B. (2022). Optimizing the NeQuick topside scale height parameters through COSMIC/FORMOSAT-3 radio occultation data. *IEEE Geoscience and Remote Sensing Letters*, *19*, 1-5. <https://doi.org/10.1109/LGRS.2021.3096657>
- Pignalberi, A., Pezzopane, M., & Rizzi, R. (2018). Modeling the lower part of the topside ionospheric vertical electron density profile over the European region by means of Swarm satellites data and IRI UP method. *Space Weather*, *16*, 304–320. <https://doi.org/10.1002/2017SW001790>

- Pradipta, R. (2006). Incoherent Scatter Radar Detection of Enhanced Plasma Line in Ionospheric E-Region over Arecibo. B.Sc. Thesis. Massachusetts Institute of Technology, 2006. <http://hdl.handle.net/1721.1/36122>. Downloaded on 21 June 2023
- Quinn, C. (2019). Examining surface effects on the Swarm satellite Langmuir Probes, M.Sc. Thesis, University of Calgary, 2019. <https://prism.ucalgary.ca/items/e7089a58-f1d8-44c0-baea-138f04c22468>
- Radicella, S. M., & Nava, B. (2020). Empirical ionospheric models. In: *The dynamical ionosphere. A systems approach to ionospheric irregularity*, 39-53. <https://doi.org/10.1016/B978-0-12-814782-5.00006-6>
- Ratovsky, K. J., Shi, J. K., Oinats, A. V., & Romanova, E. B. (2014). Comparison of diurnal, seasonal and solar cycle variations of high-latitude, mid-latitude and low-latitude ionosphere. *Chin. J. Space Sci.*, *34*(2), 143-153. <https://doi.org/10.11728/cjss2014.02.143>
- Resendiz Lira, P. A., & Marchand, R. (2021). Simulation inference of plasma parameters from Langmuir probe measurements. *Earth and Space Science*, *8*, e2020EA001344. <https://doi.org/10.1029/2020EA001344>
- Richards, P. G. (2001). Seasonal and solar cycle variations of the ionospheric peak electron density: Comparison of measurement and models. *J. Geophys. Res.: Space Phys.*, *106*, A7. <https://doi.org/10.1029/2000JA000365>
- Riley, P. (2012). On the probability of occurrence of extreme space weather events, *Space Weather*, *10*, S02012, <https://doi.org/10.1029/2011SW000734>.
- Rishbeth, H., & Garriott, O. (1969). *Introduction to ionospheric physics*. Springer
- Samaniego, J. I., Yeo, L. H., & Wang, X. (2020). A double hemispherical probe for characterizing and minimizing the self-wake effects on probe measurements. *J. Geophys. Res.: Space Phys.*, *125*, e2020JA028508. <https://doi.org/10.1029/2020JA028508>
- Schunk, R. W., & Nagy, A. (2009). *Ionospheres: Physics, plasma physics, and chemistry* (2nd ed.). New York: Cambridge University Press.
- Sedgemore-Schulthess, F., & St. Maurice, J. -P. (2001). Naturally enhanced ion-acoustic spectra and their interpretation. *Surveys in Geophysics*, *22*, 55-92. <https://doi.org/10.1023/A:1010691026863>
- Shaikh, M. M., Nava, B., & Haralambous, H. (2018). On the use of topside RO-derived electron density for model validation. *J. Geophys. Res.: Space Phys.*, *123*, 3943-3954. <https://doi.org/https://doi.org/10.1029/2017JA025132>
- Sheng, X., Beichen L., Ruiyuan, L., Lixin, G., & Yewen, W. (2014). Climatological features of the maximum electron density of the ionospheric F2 layer (NmF2) in polar regions. *2014 XXXIth URSI General Assembly and Scientific Symposium (URSI GASS)*, Beijing, China, 2014, 1-4. doi: 10.1109/URSIGASS.2014.6929844.

- Smirnov, A., Shprits, Y., Zhelavskaya, I., Lühr, H., Xiong, C., Goss, A., Prol, F. S., Schmidt, M., Hoque, M., Pedatella, N., & Szabó-Roberts, M. (2021). Intercalibration of the plasma density measurements in Earth's topside ionosphere. *J. Geophys. Res.: Space Phys.*, *126*(10), e2021JA029334. <https://doi.org/10.1029/2021JA029334>
- Sojka, J. J., Nicolls, M. J., Heinselman, C. J., & Kelly, J. D. (2009). The PFISR IPY observations of ionospheric climate and weather. *J. Atmos. Solar-Terr. Phys.*, *71*, 771-785. <https://doi.org/10.1016/j.jastp.2009.01.001>
- Stromme, A., Enkeledjda, Q., Catapano, F., Siemes, C., Sieg, D., Velimsky, J., Finlay, C., Laundal, K., Trenchi, L., Stolle, C., Hulot, G., Zhima, Z., Olsen, N., & Vogel, P. (2019). The 9-th Swarm data quality workshop. *Summary and recommendations Report*. ESA, <https://earth.esa.int/eogateway/documents/20142/1479677/Swarm-DQW9-Summary-Recommendations-Report.pdf>. Downloaded 1 June 2023.
- Themens, D. R., Jayachandran, P. T., Galkin, I., & Hall, C. (2017). The Empirical Canadian High Arctic Ionospheric Model (E-CHAIM): NmF2 and hmF2. *J. Geophys. Res.: Space Phys.*, *122*, 9015–9031. <https://doi.org/10.1002/2017JA024398>
- Themens, D. R., Jayachandran, P. T., Bilitza, D., Erickson, P. J., Häggström, I., Lyashenko, M. V., Reid, B., Varney, R. H., & Pustovalova, L. (2018). Topside electron density representations for middle and high latitudes: A topside parameterization for E-CHAIM based on the NeQuick. *J. Geophys. Res.: Space Phys.*, *123*, 1603–1617. <https://doi.org/10.1002/2017JA024817>
- Themens, D. R., Jayachandran, P.T., McCaffrey, A.M., Reid, B., & Varney, R. H. (2019a). A bottomside parameterization for the Empirical Canadian High Arctic Ionospheric Model. *Radio Sci.*, *54*, 397–414. <https://doi.org/10.1029/2018RS006748>
- Themens, D. R., Jayachandran, P. T., & McCaffrey, A. M. (2019b). Validating the performance of the Empirical Canadian High Arctic Ionospheric Model (E-CHAIM) with in situ observations from DMSP and CHAMP. *J. Space Weather Space Clim.*, *9*, A21. <https://doi.org/10.1051/swsc/2019021>
- Themens, D. R., Jayachandran, P. T., & McCaffrey, A. M. (2020). The limits of empirical electron density modeling: Examining the capacity of E-CHAIM and the IRI modeling intermediate (1- to 30-day) timescales at high latitudes. *Radio Sci.*, *55*, e2018RS006763. <https://doi.org/10.1029/2018RS006763>
- Themens, D. R., Reid, B., Jayachandran, P. T., Larson, B., Koustov, A. V., Elvidge, S., McCaffrey, A. M., & Watson, C. (2021). E-CHAIM as a model of total electron content: Performance and diagnostics. *Space Weather*, *19*, e2021SW002872. <https://doi.org/10.1029/2021SW002872>
- Usoskin, I. G. (2017). A history of solar activity over millennia. *Living Reviews in Solar Physics*, *14*, 3. <https://doi.org/10.1007/s41116-017-0006-9>

- Valentic, T., Buonocore, J., Cousins, M., Heinselman, C., Jorgensen, J., Kelly, J., Malone, M., Nicolls, M., & Van Eyken, A. (2013). *AMISR the advanced modular incoherent scatter radar*, IEEE International Symposium on Phased Array Systems and Technology, Waltham, MA, USA, 2013, pp. 659-663. doi: 10.1109/ARRAY.2013.6731908
- Wang, J., Ma, J.-G., Huang, X.-d., Bai, H.-M., Chen, Q., & Cheng, H.-Y. (2019). Modeling of the ionospheric critical frequency of the F2 layer over Asia based on modified temporal-spatial reconstruction. *Radio Sci.*, *54*, 680–691. <https://doi.org/10.1029/2019RS006856>
- Whittier, R.L. (2014). Poker Flat incoherent scatter radar investigations of the nighttime E-region. M.Sc. Thesis, University of Alaska, 2014. [https://amisr.com/publications/media/pub-pdfs/Whittier\\_MS\\_Thesis\\_UAF\\_final.pdf](https://amisr.com/publications/media/pub-pdfs/Whittier_MS_Thesis_UAF_final.pdf)
- Xiong, C., Jiang, H., Yan, R., Lühr, H., Stolle, C., Yin, F., Smirnov, A., Piersanti, M., Liu, Y., Wan, X., Diego, P., Zhima, Z., Shen, X., Förster, M., Buchert, S., & Bilitza, D. (2022). Solar flux influence on the in-situ plasma density at topside ionosphere measured by Swarm satellites. *J. Geophys. Res.: Space Phys.*, *127*, e2022JA030275. <https://doi.org/10.1029/2022JA030275>
- Yasyukevich, Y., Yasyukevich, A., Ratovsky, K., Klimenko, M., Klimenko, V. V., & Chirik, N. (2018). Winter anomaly in and TEC: when and where it can occur. *Journal of Space Weather & Space Climate*, *8*, A45. <https://doi.org/10.1051/swsc/2018036>
- Zheng, W., Jiankui, S., Guojun, W., Xiao, W., Zherebtsov, G. A., Romanova, E. B., Ratovsky, K. G., & Polekh, N. M. (2017). Diurnal, seasonal, annual, and semi-annual variations of ionospheric parameters at different latitudes in East Asian sector during ascending phase of solar activity. *Solar-Terr. Phys.*, *3*(2), 43–50, <https://doi.org/10.12737/stp-3220177>. Original Russian version published in *Solnechno-Zemnaya Fizika*, 2017, *3*(2), 45–53. <https://doi.org/10.12737/22594>